Scientific Research Associates, inc.

P.O. Box 1058, Glastonbury, Connecticut 06033, Tel: (203) 659-0333

Numerical Simulation of the Function of Scientific Intrumentation for Measuring the Speed of Electron Devices

Final Report: R92-910028F; Contract: F49620-88-C-0113

Prepared by

H. L. Grubin, J. P. Kreskovsky, W. R. Briley , G. A. Andrews,
M. A. Osman and B. J. Morrison

For

Air Force Office of Scientific Research
Bolling Air Force Base
Washington, DC 20332

February 1992

REPORT DOCUMENTATION PAGE

Form Approved
OMB No. 0704-0188

1. AGENCY USE ONLY (Leave blank)	2. REPORT DATE	3. REPORT TYPE AND DATES COVERED
	13 Feb 92	Final 1 Sep 88 - 28Feb 91

4. TITLE AND SUBTITLE
Numerical Simulation of the Function of Scientific Instrumentation for Measuring the Speed of Electron Devices

5. FUNDING NUMBERS
C - F49620-88-C-0113

6. AUTHOR(S)
H. L. Grubin, J. P. Kreskovsky, W. R. Briley, G. A. Andrews, M. A. Osman and B. J. Morrison

7. PERFORMING ORGANIZATION NAME(S) AND ADDRESS(ES)
Scientific Research Associates, Inc.
50 Nye Rd.
P.O. Box 1058
Glastonbury, CT 06033

8. PERFORMING ORGANIZATION REPORT NUMBER
R92-910028F

9. SPONSORING/MONITORING AGENCY NAME(S) AND ADDRESS(ES)
Air Force Office of Scientific Research
Bolling Air Force Base
Washington, DC 20332-5260

10.11

10. SPONSORING/MONITORING AGENCY REPORT NUMBER
3005/171

11. SUPPLEMENTARY NOTES

12a. DISTRIBUTION/AVAILABILITY STATEMENT
Reproduction in Whole, or in Part, is Permitted for any Purpose of the United States Government

12b. DISTRIBUTION CODE

13. ABSTRACT (Maximum 200 words)
Implementation of three algorithms, (i) moment equation, (ii) Monte Carlo, and (iii) quantum Liouville equation algorithms, were used in a program to determine the high speed and high frequency operation of submicron electron devices. For a psuedo-morphic high electron mobility transistor, high frequency, small signal, subpicosecond charge density waves were observed to form within the two dimensional electron gas. Large signal operation of the PHEMT indicated that the switching time of the device was governed by the longest relaxation effect, the energy relaxation time, estimated to be longer than two picoseconds. A simple two terminal device configuration was examined. It was determined that measurements of its transient behavior, would expose differences in the key relaxation times governing III-V device behavior, and provide the first direct measurement of nonequilibrium effects in semoconductor devices.

14. SUBJECT TERMS
Transient Instrumentation, Simulation, Speed, Two-Dimensional Pseudomorphic HEMT, Picosecond

15. NUMBER OF PAGES

16. PRICE CODE

17. SECURITY CLASSIFICATION OF REPORT	18. SECURITY CLASSIFICATION OF THIS PAGE	19. SECURITY CLASSIFICATION OF ABSTRACT	20. LIMITATION OF ABSTRACT
Unclassified	Unclassified	Unclassified	SAR

Numerical Simulation of the Function of Scientific Instrumentation for Measuring the Speed of Electron Devices

Abstract

Implementation of three algorithms, (i) moment equation, (ii) Monte Carlo, and (iii) quantum Liouville equation algorithms, were used in a program to determine the high speed and high frequency operation of submicron electron devices. For a pseudomorphic high electron mobility transistor, high frequency, small signal, subpicosecond charge density waves were observed to form within the two dimensional electron gas. Large signal operation of the PHEMT indicated that the switching time of the device was governed by the longest relaxation effect, the energy relaxation time, estimated to be longer than two picoseconds. A simple two terminal device configuration was examined. It was determined that measurements of its transient behavior, would expose differences in the key relaxation times governing III-V device behavior, and provide the first direct measurement of nonequilibrium effects in semiconductor devices.

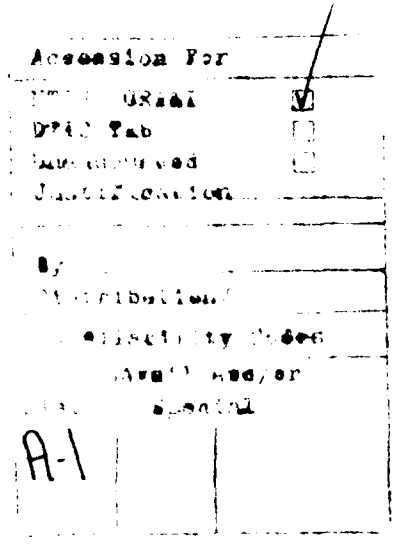

Numerical Simulation of the Function of Scientific Instrumentation for Measuring the Speed of Electron Devices

Table of Contents

SBIR Phase II Final Report

Numerical Simulation of the Function of Scientific Instrumentation for Measuring the Speed of Electron Devices

1. Introduction

The development of techniques to generate laser pulses with picosecond and sub-picosecond duration has finally provided the means to probe ultrafast relaxation process in semiconductors to determine the response time of new high speed devices. This process has introduced a series of significant dilemmas. It was thought that as device size decreases the response time decreases and the speed of the device increases. Effects such as velocity overshoot entered prominently. But we are instead finding several new issues. It is possible to reduce the response time of devices; but we are finding that when very small size devices enter the picture, capacitive and tunnelling times conspire to make tiny feature size devices slow; that is response times are often greater than one picosecond, although higher frequency components do exist.

Thus the question that remains for all devices is: *how fast can we transport charge from one end of the structure to the next, and how much charge can be transported?* In an earlier study (Phase I SBIR) it was suggested that the shortest response time of a device was the time it takes a device to approach 5-10 % of its steady state value. This is the response time for large signal behavior, but it is not necessarily the response time for small signal behavior. Indeed carriers may be expected to follow almost any signal; but whether there will be any gain or any useful operation is to be determined.

To determine the *speed signature* of a device we must understand those features of device operation that affect its transient behavior. This was the broad motivation for the Phase II SBIR study that this report summarizes. In particular through three distinctly different algorithms: (a) moment algorithms, (b) Monte Carlo algorithms, and (c) quantum transport algorithms, we examined the transient device behavior of the pseudomorphic HEMT, and were able to suggest a direct experimental means of identifying nonequilibrium transient effects in semiconductors. It is worthwhile dwelling on this last point.

For many years the device and scientific community has been seeking a measure of velocity overshoot. The conundrum is that most think that velocity overshoot exists, and that the classical steady state description of device behavior underestimates velocity and

hence current. But there was no way to compare the two because only one velocity was correct. *Thus if velocity overshoot always exists how do we detect it*? Clearly, the speed of the device is not a measure of velocity overshoot, since in general current is measured, not velocity. To address this we have taken a different tack and suggest, as a result of this study, that rather than attempt to measure velocity overshoot, measurements should concentrate on determining the differences between energy and momentum relaxation times, since these differences, when significant, are responsible for nonequilibrium device behavior.

But in addition to providing a means by which nonequilibrium effects occur, significant code development pointed to the existence of high frequency *charge density* waves in the channel of the pseudomorphic HEMT. These waves corresponded to local density changes within the two dimensional electron gas, and suggest high frequency terahertz response. The behavior of these oscillation also suggest strong high frequency capacitive contributions, but the details indicate otherwise.

In the course of the study both Monte Carlo and moment equation algorithms were examined. Steady state curves of the two were obtained for simple (non heterostructure FETs) and it was found that virtually identical results could be obtained. Because transient nonequilibrium codes were robust, the transient operation was examined using the moment codes. The primary three terminal structure studied during the Phase II program involved a two dimensional electron gas, and another issue was *how do quantum contributions affect the distribution of charge*?. Originally, this problem was to be addressed through incorporating quantum effects into the scattering integrals. While this was done, most of the effort was devoted to solving the multiparticle quantum Liouville equation, which is a generalization of the Schrodinger's equation, for the heterostructure configuration associated with the pseudo-morphic HEMT.

One of the key issues addressed during the study was whether nonequilibrium transients could be measured. *As a result of the simulations it was determined that it is possible to expose the different relaxation times in a common device configuration in a manner that would lead to the first experimental demonstration of nonequilibrium contributions to velocity overshoot.*

The basic conclusion of the Phase I study is reaffirmed for the Phase II study; namely a measure of a devices speed is the time it takes a device to approach 5-10 % of its steady state value.

2. The Governing Equations

The Moment Equations

Introduction

As indicated in our introductory remarks the thrust of this study was in both the steady state and transient behavior of devices. The equations governing this transport must be relevant. In choosing the equations care was taken with respect to the device physics, and computational resources. The three terminal structure that we are dealing with is a pseudomorphic HEMT whose operation requires quantum transport for it's description. In earlier studies, moments of the Wigner function were introduced and the effects of quantum transport were introduced through the quantum potential (Grubin and Kreskovsky, 1989). The use of the quantum potential has not progressed far enough and was not implemented during the study, although quantum transport calculations were performed through the incorporation of the density matrix. These quantum transport studies were introduced primarily to ascertain the significance of some of the space charge profiles obtained through the more traditional means of transport, and regarded as supplementary to the core simulations.

The primary transport calculations as performed today are classical calculations in which quantum transport is incorporated into the scattering integrals, and into the treatment of carriers in different subbands as interacting though scattering process. In such situations a carrier traversing a region of a device in which it makes a transition from a wide band gap region to a narrow band gap region is thought to have all of its bandgap energy converted into kinetic energy. Detailed quantum transport calculations that incorporate the quantum potential indicate that this is not occurring. Instead there are quantum mechanical forces that exist on either side of the wide band gap region that tend to mitigate the transition in energy across the interface. These effects are not included in the Monte Carlo calculations nor are they included in those moment equations that do not include quantum corrections. But for the most part they are all that we have to deal with at the present time. And so the quantum calculations are introduced to determine how well the classical transport calculations represent some of the quantum streaming contributions

During the course of this study the Monte Carlo algorithm was implemented and applied to a simple FET, as discussed in the introduction. This same FET was examined using the moments of the Boltzmann transport equation. The results of the simulation indicated that both results would yield substantially similar results quantitatively; the results were certainly qualitatively similar. Insofar as much of the one dimensional calculations indicate better numerical control in representing boundary conditions, it was decided to

devote most of the simulation effort to enhance the moment algorithms, in particular with regard to analyzing short time phenomena on a scale not represented in the current literature. It was also felt that this exercise would bear further advantages in that the moment algorithms are currently capable of modification to include quantum corrections, whereas the Monte Carlo algorithms are not. Thus further development of the moment algorithms would position us to address more realistic problems on a shorter time scale.

The moment algorithm used during the study was the three dimensional moment algorithm developed at SRA, but modified to deal with the transients in three terminal devices in a more accurate manner. During the course of the study this algorithm was generalized to deal with two dimensional transport as well as three dimensional transport. The two dimensional transport algorithm was not implemented during the course of the study, but it is anticipated that it will be used heavily in conjunction with quantum corrective transport. The development of the two dimensional transport as well as the three dimensional equations are discussed in this section. Furthermore, while we have developed the equations for nonparabolic, nonspherical systems, the discussion below is confined to parabolic systems. The new work discussed below is for two dimensional transport. Here there are two elements to consider; *first*, the streaming terms, and *second*, the scattering integrals. The streaming terms have been discussed many times by many authors, and are included here for completeness. The scattering integrals are new. By new we mean the following. There has been a considerable effort undertaken to include scattering in the two dimensional electron gas for incorporation into Monte Carlo algorithms, and some of that work was undertaken during this study. This is a straightforward prescription and simply serves to enhance a numerical capability. Indeed in many hydrodynamic transport models in semiconductors Monte Carlo algorithms have been used to obtain the scattering integrals relevant to transport. At SRA a different approach has always been taken. From the very beginning of the SRA studies with the moments of the Boltzmann transport equation, scattering integrals were computed assuming a displaced Maxwellian. In every case when a comparison was made to the Monte Carlo calculations, minor adjustments in the input parameters such as the intervalley coupling coefficient was all that was needed to achieve similar results from the two sets of calculations. It was with this confidence that a set of scattering integrals was developed. The analysis discussed is for one type of scattering event, the polar phonon.

The discussion below is geared to two dimensional transport; but for assurances that the procedures were correct, parallel three dimensional transport arguments were used as check points. In the discussion both two and three dimensional transport terms are discussed. Note all three dimensional contributions are part of the current SRA moment equation algorithm.

The Boltzmann Transport Equation and it's Moments

All information is obtained from the Boltzmann tranport equation:

$$(2.1) \qquad \{\partial/\partial t + [\hbar k/m^*]\cdot \mathrm{div}_x + [qF/\hbar]\cdot \mathrm{div}_k\} f(x,k,t) = \partial[f(x,k,t)]/\partial t|_{coll}$$

The moments of the BTE are obtained by multiplying equation (2.1) by successive powers of k, and integrating over k-space.

$$(2.2) \qquad \partial\{n_i<\phi^{(\ell)}>_i\}/\partial t + \nabla_r\{n_i<(\nabla_k E)\phi^{(\ell)}/\hbar>_i\}$$

$$= qF/\hbar \cdot n_i<\nabla_k\phi^{(\ell)}>_i + <\partial n_i\partial<\phi>_i^{(\ell)}/\partial t>_{coll}$$

For three dimensional transport:

$$(2.3) \qquad n_i<\phi^{(\ell)}>_i = [2/(2\pi)^3]\int\phi^{(\ell)}(k)f_i(k)d^3k_i$$

and for two dimensional systems:

$$(2.4) \qquad n_i<\phi^{(\ell)}>_i = [2/(2\pi)^2]\int\phi^{(\ell)}(k)f_i(k)d^2k_i$$

For parabolic bands:

$$(3D) \qquad d^3k = \sin\theta\, d\theta\, d\psi\, k^2\, dk$$

$$(2D) \qquad d^2k = d\theta\, k dk$$

In three dimensions the density is per cubic centimeter; in two dimension the density is per square centimeter. As an example consider an evaluation of the *Fermi momentum at absolute zero* for two and three dimensional systems (here we deal with $\phi^{(o)} = 1$). For both two and three dimensional systems the distribution is equal to unity up to energies equal to the Fermi energy, and zero beyond. For parabolic bands the integration is a volume integration with a value equal to $[4/3\pi]k_f^3$, whereas for the circular symmetry in the case of the two dimensional systems the integral is equal to πk_f^2. Thus for three dimensional systems:

$$(2.5) \qquad k_f = [3\pi^2 n_i^{(3)}]^{1/3}$$

and for two dimensional systems:

$$(2.6) \qquad k_f = [2\pi n_i^{(2)}]^{1/2}$$

The scattering integrals for three dimensional systems are

(2.7) $$<\partial n_i<\phi>_i^{(\ell)}/\partial t>_{coll} =$$

$$[1/4\pi^3]\int\phi^{(\ell)}d^3k_i[V/8\pi^3]\int d^3k_j\{W(\mathbf{k_i},\mathbf{k_j})f(\mathbf{k_j})[1-f(\mathbf{k_i})] - W(\mathbf{k_j},\mathbf{k_i})f(\mathbf{k_i})[1-f(\mathbf{k_j})]\}$$

and for two dimensional systems:

(2.8) $$<\partial n_i<\phi>_i^{(\ell)}/\partial t>_{coll} =$$

$$[1/2\pi^2]\int\phi^{(\ell)}d^2k_i[A/4\pi^2]\int d^2k_j\{W(\mathbf{k_i},\mathbf{k_j})f(\mathbf{k_j})[1-f(\mathbf{k_i})] - W(\mathbf{k_j},\mathbf{k_i})f(\mathbf{k_i})[1-f(\mathbf{k_j})]\}$$

In the above the indices i and j account for intervalley scattering. For i=j, there is intravalley scattering.

For the purpose of vector direction, we will assume that a two dimensional electron gas has formed. That the coordinate 'z' represents transport normal to the gate, that 'x' represents transport in the source to the drain contact, and that 'y' represents transport in the unmodelled direction. The Fermi energy for the two dimensional system defines the number of states per square centimeter .

In the absence of collisions, an exact solution to the BTE can be obtained by solving an infinite set of coupled moment equations. This procedure is now standard and has been discussed in a variety of text (see, e.g. Chapman and Cowling, 1964). This method is not, however, satisfactory and a variety of sophisticated techniques are being developed, particularly Monte Carlo procedures (see, e.g., Jacoboni and Reggiani, 1985), are being invoked. The procedure used here is based on a philosophy discussed in earlier papers by the author (see, e.g. Grubin et. al. (1982) and (1985)) and involved first estimating the distribution function and then taking moments. The specific form of the moment equations are sensitive to the approximations used for estimating the distribution function, as will be apparent below. The distribution function most often used in examining transient nonlinear high field transport is the displaced Maxwellian. This is the approach taken below.

The Displaced Maxwellian and the Moment Equations

In calculating the transient properties of submicron devices we assumed that the nonequilibrium distribum function is of the form of a displaced Maxwellian:

(2.9) $$f_o[E(\mathbf{k}-\mathbf{k_d})] = (\exp-[\mathbf{k_d}\cdot \mathrm{grad}_k])f_o(E)$$

where

(2.10) $$f_o(E) = A\exp\text{-}(E/k_BT_e)$$

where A is a constant to be determined and is different for both two and three dimensional systems. T_e is an electron temperature. For parabolic spherical energy bands in three dimensions:

(2.11a) $$E(k) = [\hbar^2/2m](k_x^2 + k_y^2 + k_z^2)$$

In two dimensions:

(2.11b) $$E(k) = [\hbar^2/2m](k_x^2 + k_z^2)$$

The first integral of interest involves the determination of the contant A. Its evaluation, which is equivalent to determining the form of the first moment (see Eq. (4)) is dependent on the requirement that

(2.12) $$\sum_k f_o(\mathbf{k}-\mathbf{k}_d) = N$$

where N is the total number of particles under study. Note, we have suppressed the energy notation in the distribution function.

For parabolic surfaces

(2.13) $$N = \sum_k f_o(\mathbf{k}-\mathbf{k}_d) = [2VA^{(3)}/(2\pi)^3]\int \exp\text{-}[E(\mathbf{k}-\mathbf{k}_d)/k_BT_e]d^3k$$

(2.14) $$N = \sum_k f_o(\mathbf{k}-\mathbf{k}_d) = [2AA^{(2)}/(2\pi)^2]\int \exp\text{-}[E(\mathbf{k}-\mathbf{k}_d)/k_BT_e]d^2k$$

where the factor "2" arises because each quantum state "k" can hold two electrons of different spin. We now defined three and two dimensional densities:

(2.15a) $$n^{(3)} = N/V = [A^{(3)}/4\pi^3]\int d^3k \exp\text{-}[E(\mathbf{k}-\mathbf{k}_d)/k_BT_e]$$

where $n = N/V$ is the density of carriers, and for two dimensional systems:

(2.16b) $$n^{(2)} = N/A = [A^{(2)}/2\pi^2]\int d^2k \exp\text{-}[E(\mathbf{k}-\mathbf{k}_d)/k_BT_e]$$

where for a three dimensional system:

(2.17) $$d^3k = \sin\theta\, d\theta\, d\Psi\, [2m/\hbar^2]^{3/2} \sqrt{E}\, dE/2$$

For a two dimensional system

(2.18) $$d^2k = d\theta\, [m/\hbar^2]\, dE$$

Thus with the introduction of the thermal deBroglie wavelength:

(2.19) $$\lambda^2 = \hbar^2/(2m_d k_B T_e)$$

(2.20) $$A^{(3)} = [4\pi^{3/2}][\lambda^3]n^{(3)}$$

and

(2.21) $$A^{(2)} = [2\pi][\lambda^2]n^{(2)}$$

Having established the value of the coefficients for the two and three dimensional systems it is direct to demonstrate that for parabolic systems the mean current is given by $ne\hbar k_d/m$, and that the pressure gradient for two and three dimensional systems is the same. Thus the first two moment equations are identical in form with the exception of the collision integrals.

Thus the first moment equation, for carrier balance, is:

(2.22) $$\partial n_i/\partial t - \mathrm{div}\, \mathbf{j}_i/e = [\partial n_i/\partial t]_{coll}$$

The second moment equation, for momentum balance, is:

(2.23) $$[\partial/\partial t + (\mathrm{div} \bullet \mathbf{v}_i)]n_i\hbar\mathbf{k}_{di} = qn_i\mathbf{F} - \mathrm{div}\, n_i k_B T_i + [\partial n_i \hbar \mathbf{k}_i/\partial t]_{coll}$$

For energy balance, and for a displaced Maxwellian, the three dimensional energy is:

(2.24) $$W_i = [3/2]n_i k_B T_e + n_i \hbar^2 k_d^2/2m$$

For two dimensional transport:

(2.25) $$W_i = n_i k_B T_e + n_i \hbar^2 k_d^2/2m$$

A result that is expected based upon equipartition. Thus the energy balance equations are:

(2.26) $$[\partial/\partial t + (\mathrm{div}\bullet \mathbf{v}_i)]W_i = qn_i\mathbf{v}_i\bullet\mathbf{F} - \mathbf{v}_i\bullet \mathrm{div} n_i k_B T_i + [\partial W_i/\partial t]_{coll}$$

with the appropriate quantity identifying energy.

The key issue in evaluating the moment equations are the scattering integrals, and this represents a new effort not discussed in the literature, as most discussion are confined to using Monte Carlo evaluations of the scattering integrals in the moment equations. We have taken the Butcher (1967) approach and have evaluated the three dimensional integrals and have begun to evaluate the two dimensional integrals. The evalulation is tedious and only a brief disucssion is given here.

The Scattering Integrals

Here we will concentrate only on the momentum balance scattering integral. We define the momentum scattering rate implicitly as :

(2.27) $$\mathbf{k}'\sum \hbar(\mathbf{k}'-\mathbf{k})W(\mathbf{k}',\mathbf{k}) = -\hbar\mathbf{k}\Gamma(E)$$

where $\Gamma(E)$ denotes a scattering rate and is energy dependent. The specific form of the energy dependence is dependent upon the scattering mechanism. The quantity $\Gamma(E)$ *is not generally the inverse of the mean free time between collisions.* It is the rate at which the net momentum is destroyed as a result of scattering. The scattering rate is used in evaluating the field dependent mobility.

With the scattering rate defined as in Eq. (2.27), the mean time rate of change of momentum due to collisions is given by

(2.28) $$[\partial n_i\hbar\mathbf{k}_i/\partial t]_{coll} = -[1/(4\pi^3)]\int d^3k\hbar\mathbf{k}\Gamma(E)f(\mathbf{k})$$

For two dimensional transport:

(2.29) $$[\partial n_i\hbar\mathbf{k}_i/\partial t]_{coll} = -[1/(2\pi^2)]\int d^2k\hbar\mathbf{k}\Gamma(E)f(\mathbf{k})$$

Note for $\Gamma(E)$ equal to a constant $1/\tau$, independent of energy:

(2.30) $$[\partial n_i\hbar\mathbf{k}_i/\partial t]_{coll} = -n_i\hbar\mathbf{k}_d/\tau$$

For three dimensions, defining:

(2.31) $$U(E) = 3(\zeta\cosh\zeta - \sinh\zeta)/\zeta^3$$

where

(2.32) $$\zeta = \hbar k_d[(2m_iE)^{1/2}]/[m_ik_BT_e]$$

and with $x \equiv E/k_BT_e$:

(2.33) $$\zeta = 2\lambda k_d(\sqrt{x})$$

the scattering takes the form

(2.34a)

$$[\partial n_i\hbar k_i/\partial t]_{coll} = -n_i\hbar k_d[1/\Gamma(5/2)][\exp-[\lambda^2 k_d^2]_o\int^\infty dx\Gamma(x)x^{3/2}U(x)\exp-x$$

This is the generic form of the scattering integral used in the SRA algorithms for the past decade. In the limiting situation as $k_d \Rightarrow 0$, $U \Rightarrow 1$ and equation (2.34a) simplifies to

(2.34b) $$[\partial n_i\hbar k_i/\partial t]_{coll} = -n_i\hbar k_d[1/\Gamma(5/2)]_o\int^\infty dx\Gamma(x)x^{3/2}\exp-x$$

For two dimensions with the following definition:

(2.35) $$I_1(\zeta) = [1/2\pi]_o\int^{2\pi} dz[\exp+(\zeta\cos z)]\cos z$$

where $I_1(\zeta)$ is a modified Bessel function of order '1' (Abramowitz and Stegun, 1964) we rewrite the scattering term as:

(2.36)

$$[\partial n_i\hbar k_i/\partial t]_{coll} = -[2n\lambda^2]\exp-[\lambda^2 k_d^2]i_o\int kdk(\hbar k\Gamma(E))I_1(\zeta)\exp-[E/k_BT_e]$$

Equation (2.36) is a new expression for scattering. We rewrite equation (2.36 in a different form, recognizing that in the limit as $\zeta \Rightarrow 0$, $I_1(\zeta) \Rightarrow \zeta/2$. We define $X(\zeta) = 2I_1(\zeta)/\zeta$. Then:

(2.37a) $$[\partial n_i\hbar k_i/\partial t]_{coll} = -i_o n\hbar k_d\exp-[\lambda^2 k_d^2]_o\int^\infty dx x\Gamma(x)X(x)\exp-x$$

To find an expression for the low field mobility we are interesting in evaluating the above in the limit as $k_d \Rightarrow 0$, or $\zeta \Rightarrow 0$, $X(\zeta) \Rightarrow 1$. Then:

(2.37b) $$[\partial n_i\hbar k_i/\partial t]_{coll} = -i_o n\hbar k_{do}\int^\infty dx x\Gamma(x)\exp-x$$

Thus to evaluate the above integrals for use in the moment equations we need an

expression for $\Gamma(E)$. For the case of three dimensional transport and polar phonons $\Gamma(E)$ is in textbooks (see, e.g., Ridley, 1982) and we simply write down the result:

$$\Gamma^{(1)}(E) = F_0/[2mE]^{1/2}[N_q\{\chi^+ - (\hbar\omega_0/E)\sinh^{-1}(E/\hbar\omega_0)^{1/2}\} + (N_q+1)\{\chi^- + (\hbar\omega_0/E)\sinh^{-1}(E/\hbar\omega_0 - 1)^{1/2}\}] \tag{2.38}$$

where:

$$\chi^{\pm} = (1 \pm \hbar\omega_0/E)^{1/2} \tag{2.39}$$

and the Frohlich force is defined as:

$$F_0 = [\hbar\omega_0/a_0](\kappa_\infty^{-1} - \kappa_0^{-1}) \tag{2.40}$$

The scattering of two dimensional electrons is considered next.

Scattering of two dimensional electrons by three dimensional phonons

As in the case of scattering of three dimensional electrons by three dimensional phonons, the situation of scattering of two dimensional electrons by three dimensional phonons proceeds along the same path. As discussed by Yokoyama and Hess (1986), and by Das Sarma et al (1988), the matrix element for scattering two dimensional electrons by three dimensional electrons involves a sum over all phonon components recognizing that the selection rules are only for those components of the phonon wave vector that are in the plane of the two dimensional electrons. *How do we treat this and effectively define a transition probability that represents two dimensional transport?* We recognize that while we are interested in in-plane transport, if we perform a sum over all phonon wave vectors then the phonon sum is a three dimensional sum. Thus we are interested in evaluating:

$$\sum_{\mathbf{k}'} \hbar(\mathbf{k}'-\mathbf{k})W(\mathbf{k}',\mathbf{k}) = [V/8\pi^3]\int \hbar(\mathbf{k}-\mathbf{k}')W(\mathbf{k},\mathbf{k}')dq_y d^2Q \tag{2.41}$$

where Q denotes the in-plane phonon wave vector with components:

$$Q = (q_x, q_z)$$

Suitable selection rules will be discussed below for the in-plane k vectors and the in-plane phonon vectors. We then rewrite equation (2.41) as

$$\sum_{\mathbf{k}'} \hbar(\mathbf{k}'-\mathbf{k})W(\mathbf{k}',\mathbf{k}) = [A/4\pi^2]\int \hbar(\mathbf{k}'-\mathbf{k})w(\mathbf{k},\mathbf{k}')d^2Q \tag{2.42}$$

where

(2.43) $$w(\mathbf{k},\mathbf{k}') = [1/2\pi][V/A]\int dq_y W(\mathbf{k},\mathbf{k}')$$

If we include a suitable overlap integral $|I_{mn}(q_z)|^2$, the matrix element for scattering the two dimensional electrons is effectively:

(2.44) $$w(\mathbf{k},\mathbf{k}') = [1/2\pi][V/A]\int dq_z |I_{mn}(q_y)|^2 W(\mathbf{k},\mathbf{k}')$$

In the discussion by Das Sarma, et al (1988), the overlap integral is ignored.

To compute equation (2.44) we write the three dimensional expression for W(k,k') in terms of the in-plane and perpendicular components q_z, we also recognize that only the in-plane phonon vectors take place in the selection rule. We find:

(2.45) $$W(\mathbf{k},\mathbf{k}')$$

$$= [4\pi^2\hbar F_o/(mV[q_y^2 + Q^2)]\{N_q\delta[E(\mathbf{k}+\mathbf{Q})-E(\mathbf{k})-\hbar\omega_o] + (N_q+1)\delta[E(\mathbf{k}-\mathbf{Q})-E(\mathbf{k})+\hbar\omega_o]\}$$

where the upper case Q denotes the in-plane phonons:

Ignoring any overlap integral contributions the integration over all q_z is direct (assume contributions from negative as well as positive values) and equal to

(2.46) $$w(\mathbf{k},\mathbf{k}')$$

$$= [2\pi^2\hbar F_o/(mAQ)]\{N_q\delta[E(\mathbf{k}+\mathbf{Q})-E(\mathbf{k})-\hbar\omega_o] + (N_q+1)\delta[E(\mathbf{k}-\mathbf{Q})-E(\mathbf{k})+\hbar\omega_o]\}$$

where w(k,k') retains the dimension of 1/time!

At this point we are interested in evaluating

(2.47) $$\mathbf{k}'\sum\hbar(\mathbf{k}'-\mathbf{k})W(\mathbf{k}',\mathbf{k}) = \mathbf{k}_\perp'\sum\hbar(\mathbf{k}'-\mathbf{k})w(\mathbf{k}',\mathbf{k})$$

where the sum on the right hand side is over the two dimensional quantum states. Thus we are interested in evaulating:

(2.48) $$\mathbf{k}_\perp'\sum\hbar(\mathbf{k}'-\mathbf{k})w(\mathbf{k}',\mathbf{k}) = [A/(4\pi^2)]\int d^2k\hbar(\mathbf{k}'-\mathbf{k})w(\mathbf{k}',\mathbf{k})$$

As in the case of the three dimensional phonon distribution and three dimensional 'k' space, here we are going to assume that **k** represents the polar axis and that the phonon

vector in the x-y plane submits to the following decomposition:

(2.49) $$\mathbf{Q} = Q(\kappa_x \cos\theta + \kappa_z \sin\theta)$$

where (κ_x, κ_z) are unit vectors. Then, for *phonon absorption*:

(2.50) $$\delta[E(\mathbf{k}+\mathbf{Q}) - E(\mathbf{k}) - \hbar\omega_0] = [2m/\hbar^2]\delta[Q^2 + 2kQ\cos\theta - 2m\omega_0/\hbar]$$

or with 'g' representing the argument of the delta function in equation (2.50)

(2.51) $$\delta[E(\mathbf{k}+\mathbf{Q}) - E(\mathbf{k}) - \hbar\omega_0] = [2m/\hbar^2]\delta[g]$$

The zeroes of g(x) are

(2.52) $$Q_{1,2} = -k[\cos\theta \pm (\cos^2\theta + \hbar\omega_0/E)^{1/2}]$$

where $E = E(k) = \hbar^2 k^2/2m$. In view of the constraint that $Q > 0$, the only possible root of g(x) is

(2.53) $$Q_2 = -k[\cos\theta - (\cos^2\theta + \hbar\omega_0/E)^{1/2}], \quad 0 \le \theta \le 2\pi$$

where we notice that the range of integration is now over 2π, as is required by the two dimensional nature of the transport. Thus for phonon absorption the conservation condition is:

(2.54) $$\delta[E(\mathbf{k}+\mathbf{Q}) - E(\mathbf{k}) - \hbar\omega_0] = [m/\hbar^2]\delta[Q - Q_2]/[k(\cos^2\theta + \hbar\omega_0/E)^{1/2}],$$

$$0 \le \theta \le 2\pi$$

Performing the integration of equation (2.48) for absorption:

(2.55) $$\mathbf{k}_\perp' \sum \hbar(\mathbf{k}'-\mathbf{k})w(\mathbf{k}',\mathbf{k}) = -[\kappa_x 2F_0 N_q]_0 \int^{\pi/2} d\theta\, [\cos^2\theta/(\cos^2\theta + \hbar\omega_0/E)^{1/2}]$$

We defer a discussion of the above until after a description of scattering due to phonon emission. The first thing we need are selection rules for phonon emission. From the selection rules for three dimensional transport, we find:

(2.56) $$\delta[E(\mathbf{k}-\mathbf{Q}) - E(\mathbf{k}) + \hbar\omega_0] = [2m/\hbar^2]\delta[Q^2 - 2kQ\cos\theta + 2m\omega_0/\hbar]$$

again defining a quantity 'g' as the argument of the delta function for phonon emission:

(2.57) $$\delta[E(\mathbf{k}-\mathbf{Q})-E(\mathbf{k})+\hbar\omega_0] = [2m/\hbar^2]\delta[g]$$

The zeros of g

$$Q_{s,4} = k[\cos\theta \pm (\cos^2\theta - \hbar\omega_0/E)^{1/2}]$$

for phonon emission:

(2.58)

$$\delta[E(\mathbf{k}-\mathbf{Q})-E(\mathbf{k})+\hbar\omega_0] = [m/\hbar^2]\{\delta[Q-Q_s]+\delta[Q-Q_4]\}/[k(\cos^2\theta-\hbar\omega_0/E)^{1/2}]$$

For $E < \hbar\omega_0$, there is no solution for $Q_{s,4}$. For $E > \hbar\omega_0$, and defining

(2.59) $$\theta_E = \cos^{-1}(\hbar\omega_0/E)^{1/2}$$

solutions exist for θ in the first and fourth quadrants, subject to the constraint

(2.60) $$\cos^2\theta > \hbar\omega_0/E$$

Thus performing the integration of equation (2.48) for phonon emission:

(2.61)

$$\mathbf{k}_\perp \sum \hbar(\mathbf{k}'-\mathbf{k})w(\mathbf{k}',\mathbf{k}) = -[2\kappa_x F_0(N_q+1)][_0\int^{\theta E-\varepsilon} d\theta\,[\cos^2\theta/(\cos^2\theta-\hbar\omega_0/E)^{1/2}]$$

Combining equations (2.55) and (2.61) the net scattering rate for two dimensional electrons scattered by three dimensional phonons is:

(2.62) $$\Gamma = [2F_0/(2mE)^{1/2}]\{N_q][_0\int^{\pi/2} d\theta\,[\cos^2\theta/(\cos^2\theta+\hbar\omega_0/E)^{1/2}]$$

$$(N_q+1)][_0\int^{\theta E-\varepsilon} d\theta\,[\cos^2\theta/(\cos^2\theta-\hbar\omega_0/E)^{1/2}]\}$$

In order to place the above results in perspective with respect to the scattering of three dimensional electrons by three dimensional phonons we rewrite equation (2.38) for the rate of scattering three dimensional electrons by three dimensional phonons:

(2.38) $$\Gamma(E) = F_0/[2mE]^{1/2}[N_q\{\chi^+ - (\hbar\omega_0/E)\sinh^{-1}(E/\hbar\omega_0)^{1/2}\}$$

$$+(N_q+1)\{\chi^- + (\hbar\omega_0/E)\sinh^{-1}(E/\hbar\omega_0-1)^{1/2}\}]$$

The similarity is apparent.

For incorporation of the above results into expressions for evalulating the mobility of the carriers equation (2.38) for three dimensional electrons is inserted into equation (2.34), whereas equation (2.62) is inserted into equation (2.37). We have carried the analysis to the point of integration for the case of two dimensional electrons, but not further. For comparison we also offer the expressions for the three dimensional electrons. Consider first three dimensional electrons and define $x_e = \hbar\omega_o/k_BT_e$. Then:

(2.63)
$$\Gamma(x) = F_o/[2mk_BT_ex]^{1/2}[N_q\{x + -(x_o/x)\sinh^{-1}(x/x_o)^{1/2}\}$$
$$+(N_q+1)\{x^- + (x_o/x)\sinh^{-1}(x/x_o-1)^{1/2}\}]$$
$$= F_o/[2mk_BT_ex]^{1/2}Q(x)$$

Thus the rate of momentum loss as obtained from the above description for three dimensional electrons, when combined with equation (2.34a) yields:

(2.64)

$$[\partial n_i\hbar k_i/\partial t]_{coll} = -n_i\hbar k_d[4F_o/3(2\pi mk_BT_e)^{1/2}]\exp-[\lambda^2 k_d^2]_o\int^\infty dx x Q(x)U(x)\exp-x$$

which is the expression used for computing the scattering integral for polar phonons in the SRA code.

The comparable expression for the scattering of two dimensional electrons by three dimensional phonons is obtained with the scattering rate rewritten as:

(2.65)
$$\Gamma = [2F_o/(2mk_BT_ex)^{1/2}]\{N_q]_o\int^{\pi/2} d\theta[\cos^2\theta/(\cos^2\theta + x_e/x)^{1/2}]$$
$$(N_q+1)][_o\int^{\theta E-\varepsilon} d\theta[\cos^2\theta/(\cos^2\theta - x_e/x)^{1/2}]\}$$
$$= [2F_o/(2mk_BT_ex)^{1/2}]R(x)$$

Then from equation (2.37) we find:

(2.66)

$$[\partial n_i\hbar k_i/\partial t]_{coll} = -i_o n\hbar k_d[2F_o/(2mk_BT_e)^{1/2}]\exp-[\lambda^2 k_d^2]_o\int^\infty dx x^{1/2} R(x)X(x)\exp-x$$

Equation (2.66) is presently being placed into a form suitable for the MBTE algorithm.

The Density Matrix

The space charge profiles for the pseudomorphic HEMT were computed from the moment equations. But as a check on their significance as well as a means of addressing contact problems, as discussed in later sections, the Liouville equation was solved. *The Liouville equation is a quantum mechanical operator equation.* In commutator form, the equation is:

$$i\hbar\,\partial\rho_{op}/\partial t = [H,\rho_{op}] \tag{2.67}$$

where ρ_{op} is the density operator and H is the system Hamiltonian. The Liouville equation is expressed with respect to a specific representation, the most popular being the *mixed representation* discussed by Wigner (1932). In the mixed representation the distribution function is the Wigner function and quantum transport is described by a differential equation that is *ostensibly* similar to Boltzmann equation and may be obtained from the latter by replacing the force term in the Boltzmann equation with (in one space and one momentum direction):

$$+(1/i\hbar)(1/2\pi\hbar)\int_{-\infty}^{+\infty}dp'\int_{-\infty}^{+\infty}dx'f(p',x')[V(x+x'/2,t)-V(x-x'/2,t)]\exp[i(p-p')x'/\hbar]$$

An alternative representation is that implemented at SRA. The alternative representation is generally referred to as the *coordinate representation*; and the quantity computed is called the density matrix, which is related to the mixed representation (Wigner function) through (in one space and one momentun direction):

$$\rho(x,x',t) = [1/(2\pi h)]\int_{\infty}^{\infty}dpf(x,p,t)\exp[i(x-x')p/\hbar] \tag{2.68}$$

In the AFOSR sponsored SBIR study the density matrix equation of motion in the coordinate representation was solved for electrons.

The Liouville equation in the coordinate representation for electrons (ignoring any spatially dependent effective mass and dissipation) is the following differential equation for electrons $\rho_e(x,x',t)$:

$$i\hbar\,\partial\rho_e/\partial t = -(\hbar^2/2m)(\nabla^2-\nabla'^2)\rho_e + [E_c(x,t)-E_c(x',t)]\rho_e \tag{2.69}$$

The equation of motion of the density matrix is a *Schrodinger-like equation.* In its simplest form the density matrix for electrons can be obtained from a solution to Schrodingers equation through the relation:

(2.70) $$\rho(x,x',t)=\Sigma\rho_{m,m}\psi_m(x,t)\psi^*_m(x',t)$$

In equation (2.69) $E_c(x,t)$ is the conduction band energy that would appear in the single particle Schrodinger equation. $E_c(x,t)$ is obtained from the vacuum potential energy $V(x,t)$ from the Anderson rule:

(2.71) $$E_c(x,t) = V(x,t)-X(x)$$

where $X(x,t)$ is the electron affinity of the material. $\rho_e(x,x',t)$ is the density matrix for electrons in the coordinate representation.

All observables such as *density, current, energy,* are obtained from the *diagonal components* of the density matrix and suitable derivatives thereof Grubin, et al (1992). Thus the electron density is $\rho_e(x,x)$:

(2.72) $$\rho_e(x)=\rho_e(x,x)$$

The potential energy of the vacuum is governed by Poisson's equation:

(2.73) $$\nabla_x[\epsilon(x)\nabla V_x] = -e^2[(\rho_e(x)-\rho_h(x))-(N_d^+(x)-P_a^-(x))]$$

The background density in the above equation is assumed as a *jellium* doping distribution with N_d^+ representing the ionized donors and P_a^- representing the ionized acceptors.

Reduction of Liouville Equation for One Dimensional Spatial Transport

In the calculations described in this study we assumed Boltzmann statistics, spatial variations only along the x-direction, and free particle behavior along the y-and z-directions. The equation of motion of the density matrix was transformed to center of mass 'r' and nonlocal 'ζ' coordinates:

(2.74) $$r = (x + x')/2,$$

$$\zeta = (x - x')/2,$$

In these terms the density matrix is re-expressed as:

$$\rho \Rightarrow \rho(r+\zeta, r-\zeta),$$

and equation (2.69) for electrons becomes:

(2.75) $$i\hbar\,\partial\rho_e/\partial t = -(\hbar^2/2m)\partial^2\rho_e/\partial r\partial\zeta + [E_c(r+\zeta,t)-E_c(r-\zeta,t)]\rho_e$$

In these variables Poissons equation reads:

(2.76) $$\partial/\partial r[\epsilon(r)\partial V/\partial r] = -e^2[(\rho_e(r)-\rho_h(r))-(N_d^+(r)-P_a^-(r))]$$

The diagonal components of solutions to equation (2.75) (along the diagonal $r=x$ and $\zeta=0$) provide the density for the electrons with a similar description for the holes.

Note, time independent steady state conditions, implies: $\partial\rho_e/\partial t = 0$

3. Steady State Simulations of a Pseudomorphic HEMT

Effects of Metalization

The use of AlGaAs/GaAs HEMTS results in higher electron velocities and mobilities at low lattice temperatures. High aluminum mole fractions, however, also have the deleterious property of increased bulk-related trapping centers. To reduce these traps the device designer has several options; one is to reduce the Al concentration, which has the consequent effect of reducing band offset, and lowering the 2DEG at the interface. An alternative was demonstrated by Ketterson et al (1987); where, for sufficiently thin InGaAs layers, the compressive elastic strain is accommodated by tetragonal distortion of the InGaAs lattice rather than the generation of misfit dislocations. The result is a HEMT with satisfactory off-set voltage and reduced bulk-related trap centers. HEMTs constructed from such a quantum well are generally called pseudomorphic HEMTs.

The fabrication of a HEMT generally involves the placement of contacts on a narrow band-gap material such as gallium arsenide (or indium gallium arsenide), which in turn is deposited on the wide band gap material. Simulating such a structure is always difficult as it requires dealing with transport through a barrier, necessitating *the implementation of quantum transport algorithms.* With regard to the issue of transport through the barrier it is recognized that there is a body of opinion suggesting that metalization destroys the integrity of the barrier. *Rather than ignore the barrier issue we asked, What if?, the barrier is present.*

This issue was examined generically, through implementation of quantum algorithms developed in part with support from AFOSR. If we assume, for example an FET structure whose topmost portion can be represented by figure 3.1, then it is possible to implement the SRA quantum transport algorithm and ask *what if?* questions concerning the transport of carriers to the quantum well for the case when *the integrity of the heterostructure layers*

Narrow Band Gap Material

Wide Band Gap Material

Narrow Band Gap Quantum Well

Fig 3.1a Generic top layers of a HEMT structure.

is not compromised by the contact metalization process.

The SRA quantum transport simulations involve implementing an algorithm for solving the Liouville equation in the coordination representation. Figure 3.1b displays the self-consistent potential and charge distributions (solutions to Poisson's equation are included), under equilibrium conditions, for a *uniformly doped*, 350Å wide band (barrier height of 300 mev), region surrounded by two narrow band gap regions. Such regions may be expected to mimic *under equilibrium* the source and drain regions of a pseudomorphic HEMT with uniform doping through the quantum well.

Several features are highlighted: (i) a two dimensional electron gas forms on both sides of the wide band gap region; (ii) the barrier as seen by carriers entering the structure is reduced by nearly 10 mev, and *is replaced by two small tunneling regions at the ends of the barrier.* The result clearly suggests that a significant component of current from the source contact to the quantum well can be accomplished by carriers tunneling through the thin barriers, as well as by thermionic emission over the barrier. Note, the considerably reduced free carrier concentration in the barrier region. On the basis of this calculation there is likely to be an insignificant amount of parasitic source to drain current flowing in the wide bandgap material parellel to the 2DEG.

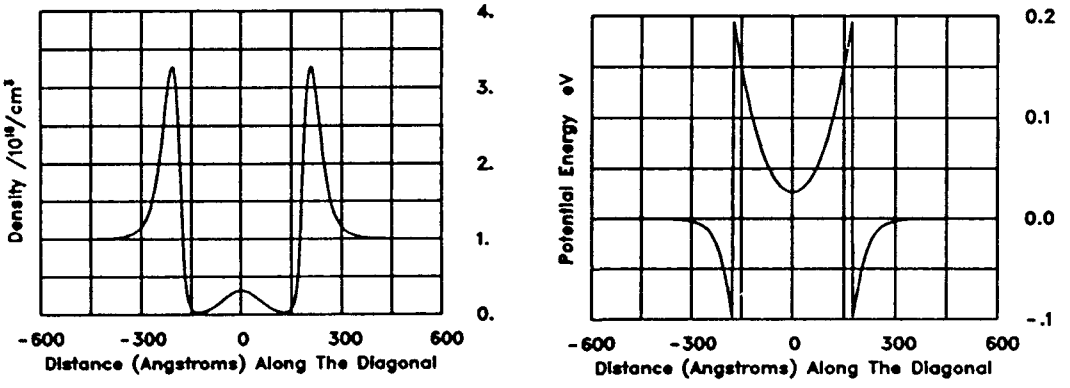

Figure 3.1b. Self consistent distribution of potential energy and charge for a uniformly doped narrow band gap-wide band gap- narrow band gap structure.

The situation when the doping in the structure ends within the wide gap material is qualitatively similar on the contact side of the structure. However, at the interface between the wide bandgap region and the quantum well the density of the 2DEG is reduced, as shown in figure 3.1c

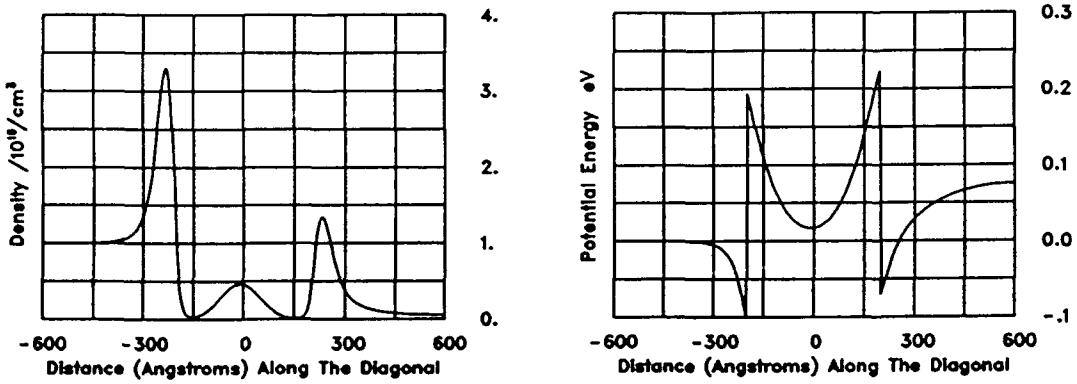

Figure 3.1c. As in figure 3.1b, but where the doping ends at the quantum well.

The Phase II calculations that were performed for the PHEMT were based upon semiclassical physics, and tunneling contributions were not included. A different study on HEMTs which included semiclassical physics permitted thermionic emission over the barrier and indicated that the barrier provided an unrealistically high source resistance. This necessitated performing calculations in which boundary conditions were imposed directly on the wide band gap material, a feature common to most HEMT studies. Because of the availability of the quantum transport algorithm at SRA, the potential and mobile charge density distribution were computed for a situation in which boundary conditions were imposed directly on the wide band gap material, as was done in the full PHEMT simulations. These calculations provided some measure of the nature of the semiclassical approximations we made.

Figure 3.2a displays a sequence of calculations for a 1200 Å structure. The left 600 Å is comprised of a wide band gap material (300 mev barrier); the right side is a narrow bandgap material. The sequence of calculations is for a doping distribution of $10^{18}/10^{18}$, $10^{18}/10^{17}$, $10^{18}/10^{16}$, $10^{18}/10^{15}$, respectively. There are several points to note: (i) approximately 150 Å of the wide band gap material is depleted of carriers; (ii) the 2DEG forms within the first 100 Å of the narrow bandgap material; (iii) the density of the 2DEG is insensitive to quantum well doping levels below $10^{16}/cm^3$. The potential distribution is also shown, and incorporates the conduction band offset. Note that approximately 2/3 of the offset voltage falls across the wideband gap material. How do these calculations compare to the semiclassical calculations?

Semiclassical calculations performed under the Phase I study, in which metallization is assumed computationally to occur at the wide band gap material show the distribution displayed in figure 3.2b. In comparing figures 3.2a and 3.2b, the first point to note is that the density is higher in the classical calculation (in the quantum mechanical calculation

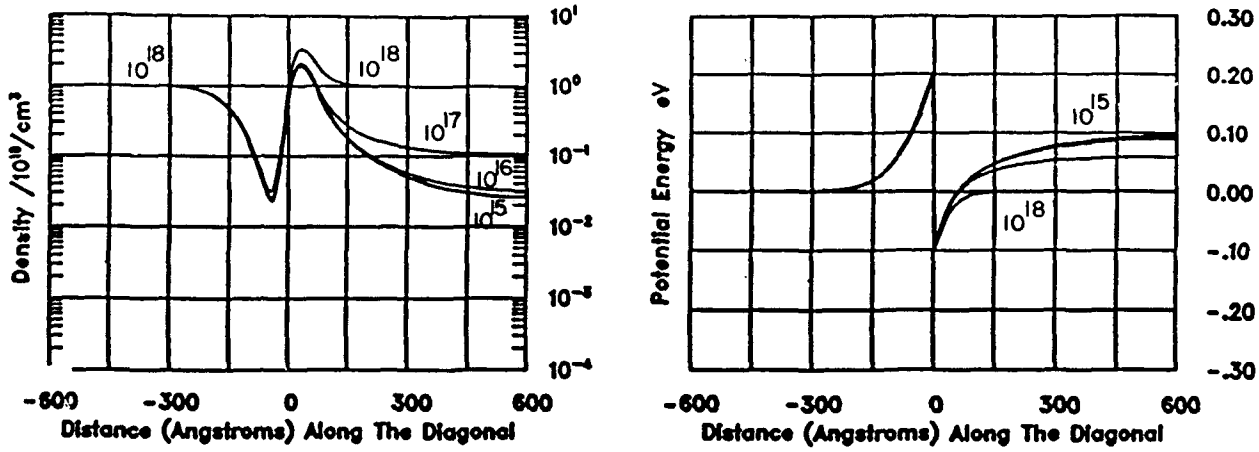

Figure 3.2a Quantum mechanical calculations of the distribution of charge and potential for a wide band gap/ narrow band gap structure with varying doping concentrations.

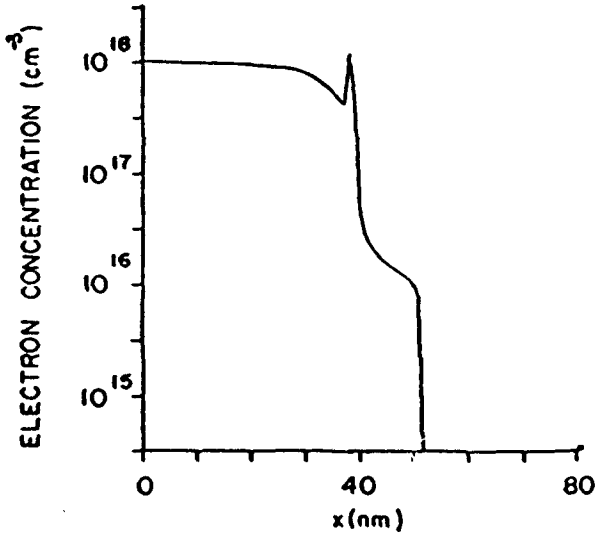

Figure 3.2b. Distribution in charge under the source region for a 400 A wide band gap region adjacent to a narrow band gap region. From Phase I Final Report, figure 21 a.

variations in the effective mass were not taken into account). The second point to note is that the density drops precipitously at the end of the quantum well, a feature not accounted for in the quantum calculations displayed here, although a rapid decrease in charge at the end of quantum well has been observed by the investigators in other calculations. The broad conclusion that can be drawn from a comparison of figures 3.2a and 3.2b is that the parasitic current flow parallel to the 2DEG but in the wide band gap

material is likely to be overestimated in the semiclassical calculations.

The Structure Simulated

The structure that was simulated under the Phase II study is shown in figure 3.3. *Note that boundary conditions were imposed on the wide band gap material.* The simulations were carried out for a range of bias conditions using the moments of the Boltzmann transport equation algorithm. The device consists of 0.5 μm source and drain contacts with a source drain spacing of 1.0 μm. An 0.25 μm gate is placed symmetrically between the source and drain. The device structure consists of a 350Å layer of AlGaAs doped to 1 x $10^{18}/cm^3$, followed by a 30Å undoped layer of AlGaAs. Below this is a 150Å deep channel of undoped InGaAs, which sits on a GaAs substrate.

The Current Voltage Characteristics

The Phase I current voltage characteristics for this structure with a device width of fifty microns obtained through solution to drift and diffusion equations are shown in figure 3.4, while those obtained using the moments of the Boltzmann transport equation are shown in figure 3.5. For the MBTE calculation, gate bias levels of 0.4, 0.0, and -1.0 volts were considered over a drain bias level between 0.0 and 3.0 volts. The current voltage characteristics of the device, as predicted by the MBTE simulation code show current levels that are of the order of three times larger than that obtained with the dirft and diffusion results, a feature that is consistent with effects of velocity overshoot. There is, however, structure in these curves that is not present in the drift and diffusion calculations.

Internal Dynamics

The current voltage characteristics represent a coarse summary of the internal dynamics of the PHEMT. It is the internal dynamics that is discussed next through line and contour plots of the internal distribution of carriers, temperature and potential. Transient effects associated with switching between bias points is also discussed in terms of these plots.

Interpretation of these results is aided by examining Figure 3.6, which shows a portion of the computational mesh used in the simulation. The location of the material and doping interfaces are indicated in the figure. The domain shown includes only approximately the first 425Å of the substrate. As will become evident in the subsequent figures, the remainder of the substrate plays no significant role in the device dynamics. The points labeled 1 through 3 represent selected points where the transient history of a variety of quantities will be examined.

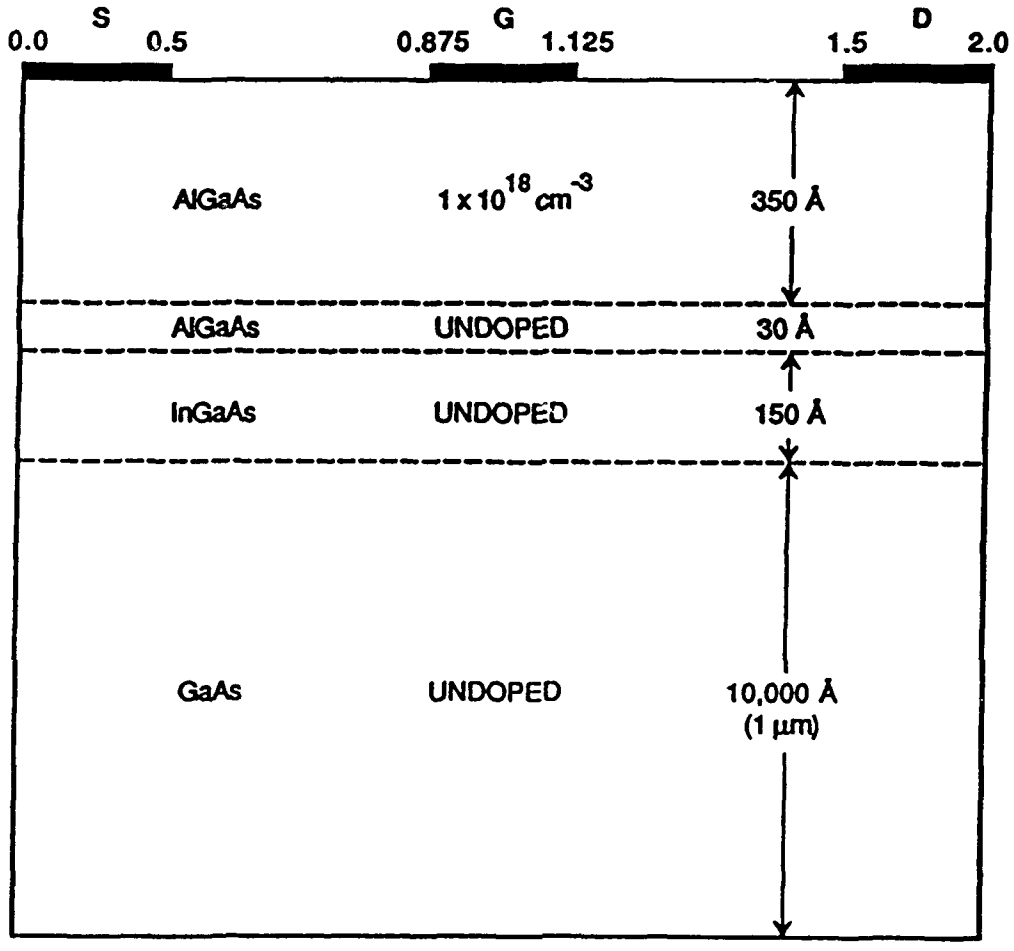

Figure 3.3. Schematic of the Pseudomorphic HEMT (Device Width = 50 microns).

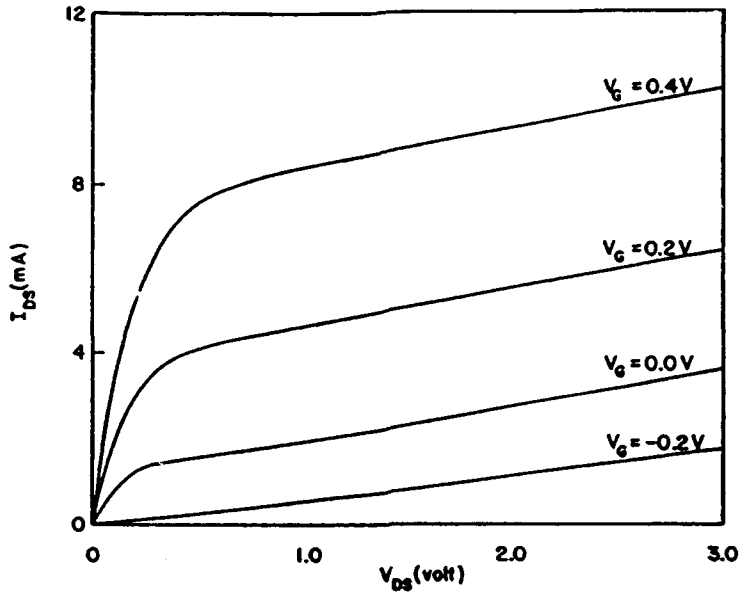

Figure 3.4. Current voltage characteristics for a 50 micron wide PHEMT as obtained from the drift and diffusion equations. From Phase I Final Report.

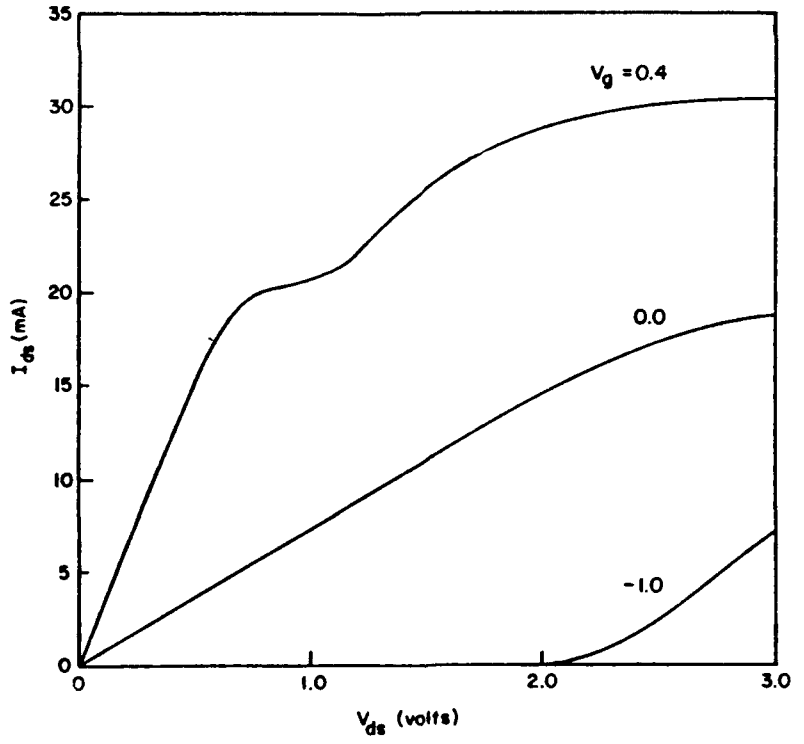

Figure 3.5 Current voltage characteristics for a 50 micron wide PHEMT as obtained from the moments of the Boltzmann transport equation.

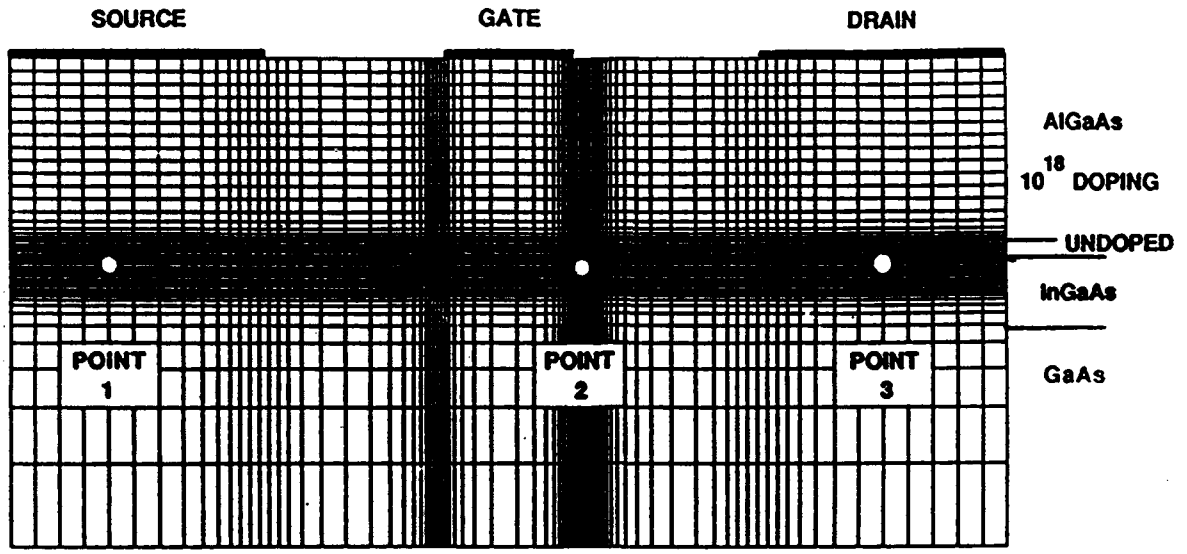

Figure 3.6 Computational grid for the PHEMT.

Equilibrium Calculation

Figure 3.7 shows the potential distribution (a) and electron density (b) when V_{ds} and V_{gs} are zero. Under such conditions the carriers are in static equilibrium with the lattice at 300° K. The contours show the anticipated symmetric distribution of these quantities. The high field region under the gate (evidenced by the closely-spaced potential contours) and the depletion of carriers from the heavily-doped AlGaAs under the gate are clearly evident. Also evident is the accumulation (darkened regions) of carriers, a two-dimensional gas, at the interface between the AlGaAs and InGaAs materials under the source and drain regions and their confinement to the InGaAs channel. The density in this region reaches levels in excess of 3 x $10^{18}/cm^3$. The depletion of electrons from the channel under the gate is also evident.

Figure 3.8 displays line plots of the potential and electron density. The plots are along a line normal to the center of the gate. The potential plot represents only the self consistent potential as obtained from Poisson's equation. (The self consistent potential plus the heterostruture potential are incorporated into the calculations discussed in figures 3.2.)

Here, N_1 represents the lower valley carriers and $N_1 + N_2$ the total carrier density, the difference being upper L-valley electrons. For this calculation most of the carriers are in the Γ-valley. This figure clearly shows the depletion of carriers directly under the gate and in the channel. However, the carrier density in the channel, due to accumulation at the material interface, remains at a value of nearly $1.5 \times 10^{17}/cm^3$ and then decreases rapidly in the substrate. Recall that under the source and drain the density in the channel exceeds $3 \times 10^{18}/cm^3$.

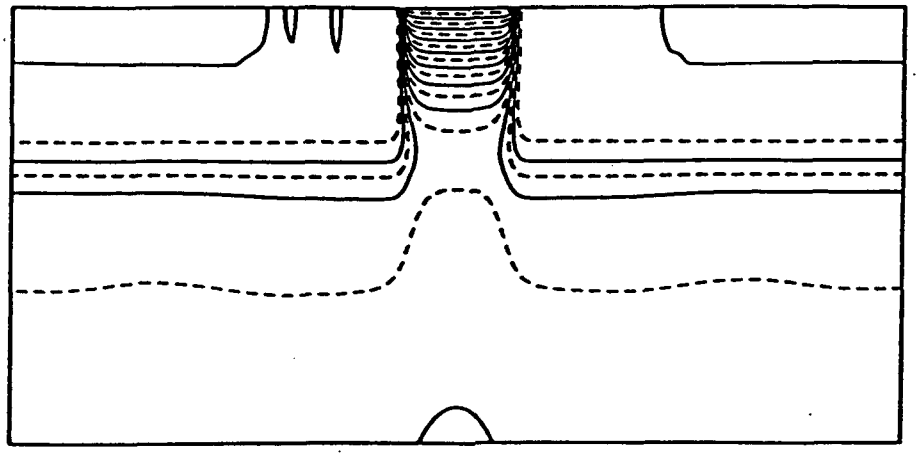

a) Potential.

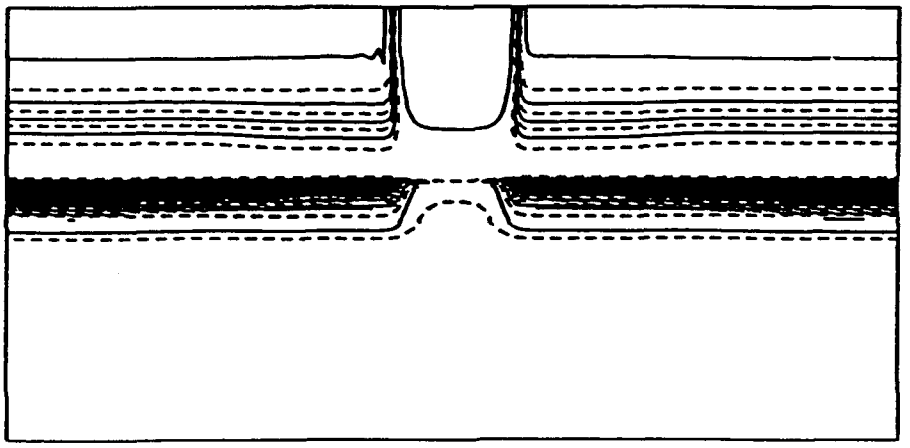

b) Electron Density.

Figure 3.7 Computed Contours for $V_{ds} = 0.0$ and $V_{gs} = 0.0$

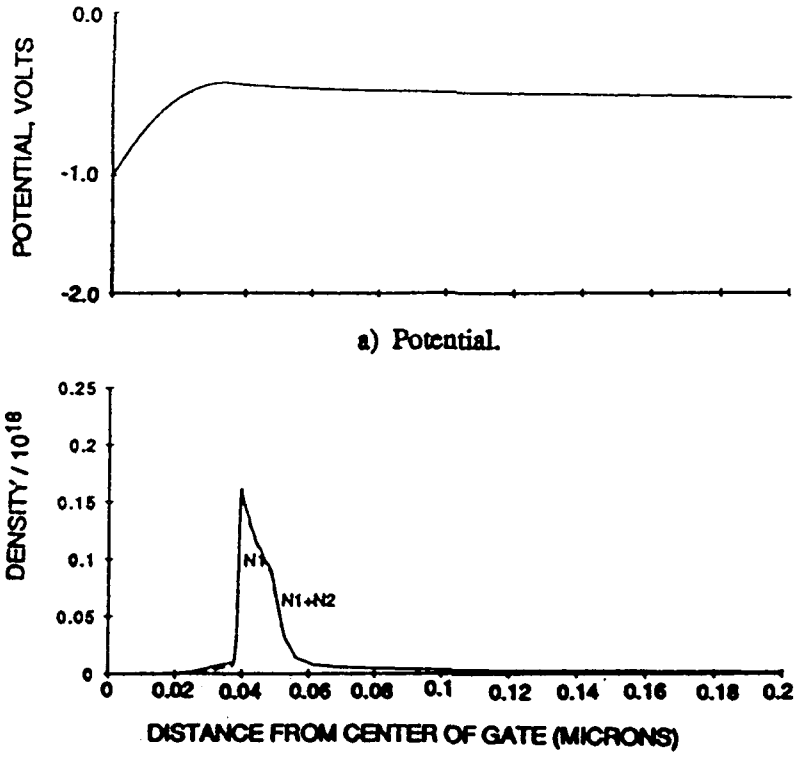

Figure 3.8 Computed Distributions Normal to Center of Gate for $V_{ds}=0.0$ and $V_{gs}=0.0$

Nonequilibrium Calculations

Steady State, $V_{ds}=1.0$ v, $V_{gs}=0.0$ v

The next set of figures, Figures 3.9 through 3.12, show the results for $V_{ds}=1.0$, $V_{gs}=0.0$. In Figure 3.9a the potential distribution shows the effect of the applied bias. The potential contours under the gate are distorted with a larger potential drop under the *drain side* of the gate contact, than on the *source side* of the gate contact. There is also the formation of a longitudinal field from the source to the drain contact, as represented by vertical contours. *The high field at the drain end of the gate extends across the channel and into the substrate*, where it has the effect of distorting the charge distribution, without any significant influence on the transport of carriers to the contacts.

The density contours, Figure 3.9b, when compared to Figure 3.7, show an extension of the depletion region outward into the channel and a reduction of the carrier density in the channel under the gate. This occurs because electrons are drawn from this region by the applied bias. *Thus, even though a current flows, the carrier density is lower in the channel*

than when $V_{ds}=0.0$.

The current path from source to drain is shown by the *current streamlines* in Fig. 3.9c. Here we observe that the current path flows directly from the source to the 2 DEG. The majority of the current then flows within the 2 DEG to the drain side of the device, where it is collected at the drain. The streamlines which intersect the bottom of the figure indicate current paths deeper in the substrate. These represent a small fraction of the current flow from the source to the drain contact.

Figures 3-10 through 3-12 show profile plots along lines normal to the center of the source, gate and drain, respectively for the case $V_{ds}=1.0$ and $V_{gs}=0.0$. For the source and drain region, the self consistent *potential* variation shows the expected shape (potential decreases toward the quantum well) resulting from diffusion of carriers into the undoped region and the accumulation of carriers at the AlGaAs/InGaAs interface under the source and drain. The shape of the potential under the gate corresponds to depletion under the gate.

The *density* profiles under the source and drain, Figures 3-10b and 3-12b, show the diffusion of carriers into the undoped AlGaAs region from the heavily-doped AlGaAs layer and the sharp peak in concentration in the 2 DEG. Several points are noteworthy: (1) The distribution of charge under the source, which may be expected to represent equilibrium conditions, differs from the result obtained quantum mechanically (as discussed earlier). (2) Under the influence of the drain bias the peak density in the 2 DEG under the drain approaches $4x10^{18}/cm^3$. This is a result of two factors. First, due to the drain bias electrons are pulled towards the drain end of the channel. Second, electrons easily enter the 2 DEG at the source, but the interface between the AlGaAs and InGaAs acts as a barrier at the drain. Electrons pile up at this barrier in an attempt to reach the drain. Under the gate, in Figure 3-11b, the electron density in the channel is much lower, at a level near $5x10^{16}/cm^3$, than the equilibrium value of near $1.5x10^{17}/cm^3$.

The *central valley electron temperature* shown in these three figures indicates that electrons enter and leave the device nearly at equilibrium with the lattice. The lattice temperature is at the ambient at the source and drain contact. A small increase in temperature to 1.4 times the lattice temperature, or 420° K occurs under the gate, due to the high source-drain field in this region. This increase is fairly uniform across the entire device, consistent with the potential variation shown in Figure 3.9a. Within the context of the electron temperature model used in the moment formulation, increased electron temperature implies electron transfer from the Γ valley to the L valley. The temperature rise for this bias level was not great enough to cause significant electron transfer.

The *central valley velocity component parallel to the heterostructure interface* is shown in Figure 3-11d. Again the distribution is fairly uniform across the device, reaching a value of approximately 6×10^7 cm/sec. Since the only place any significant numbers of carriers are present is at the 2DEG, only a small current density emerges.

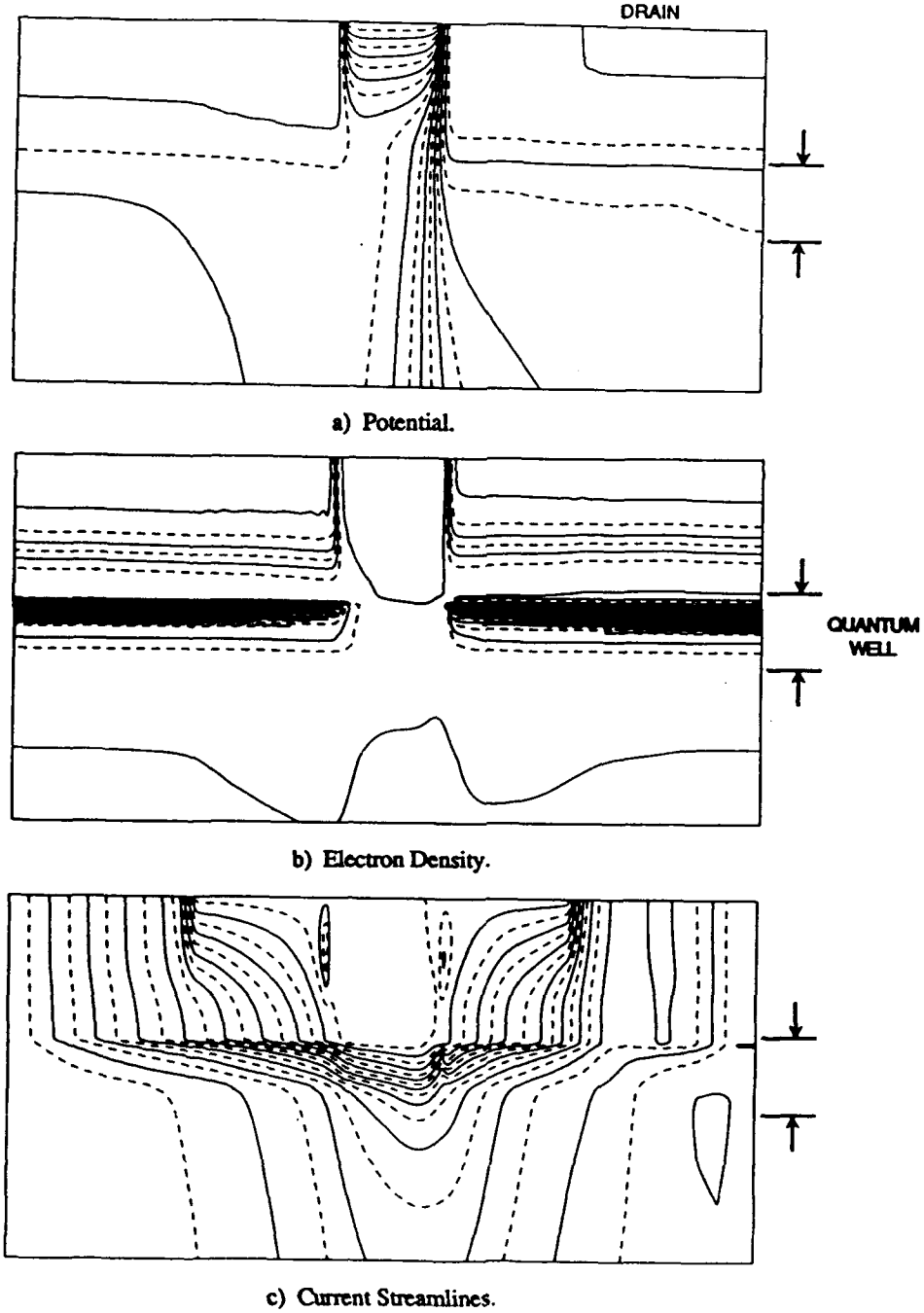

a) Potential.

b) Electron Density.

c) Current Streamlines.

Figure 3.9 Computed Contours for $V_{ds} = 1.0$ and $V_{gs} = 0.0$

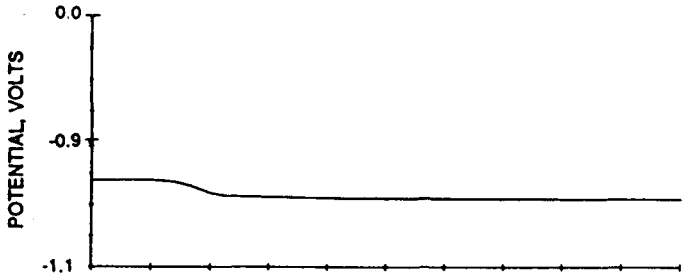

a) Potential.

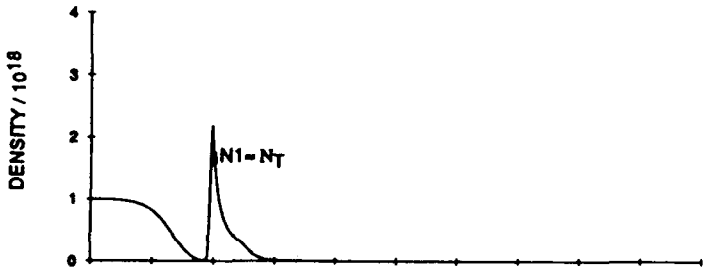

b) Electron Density.

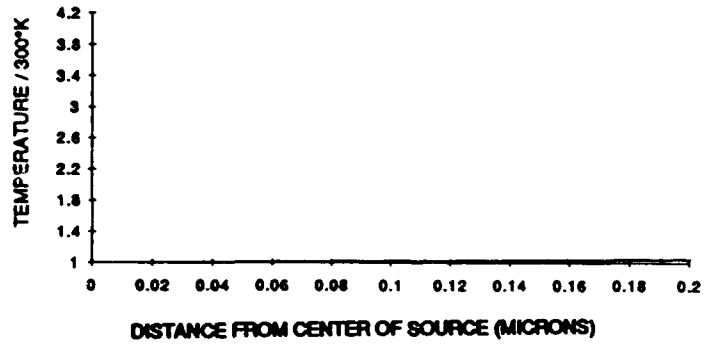

c) Gamma Valley Temperature.

Figure 3.10 Computed Distributions Normal to Center of Source for $V_{ds} = 1.0$ and $V_{gs} = 0.0$

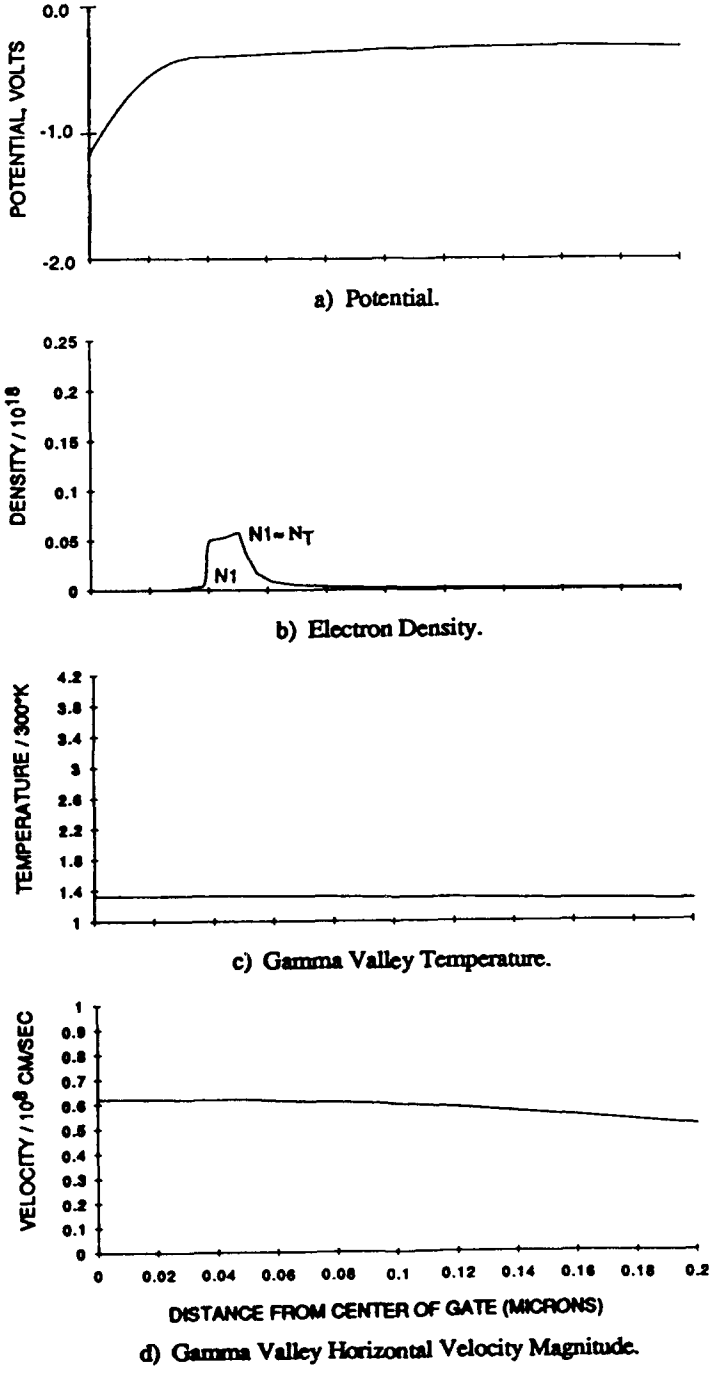

Figure 3.11 Computed Distributions Normal to Center of Gate for $V_{ds} = 1.0$ and $V_{gs} = 0.0$

a) Potential.

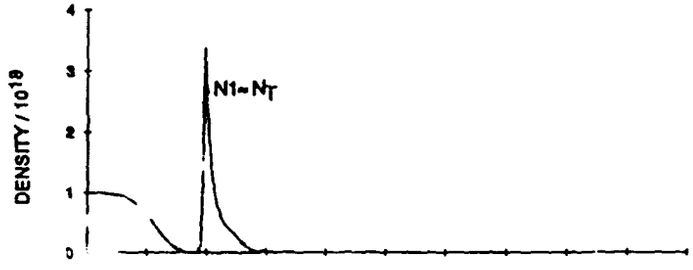

b) Electron Density.

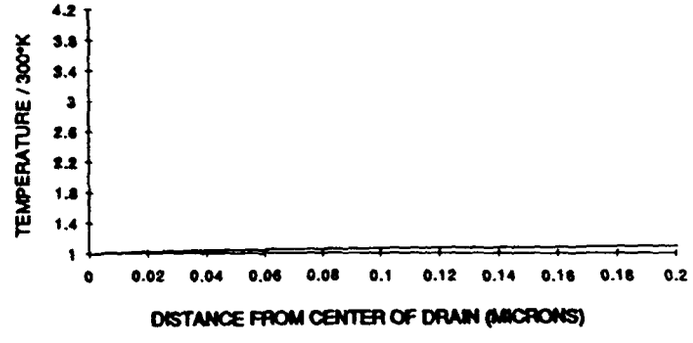

c) Gamma Valley Temperature.

Figure 3.12 Computed Distributions Normal to Center of Drain for $V_{ds} = 1.0$ and $V_{gs} = 0.0$

Steady State, $V_{ds} = 2.0$ v, $V_{gs} = 0.0$ v

When the drain bias is increased to $V_{ds} = 2.0$ volts while holding the gate bias at 0.0, the distribution of potential, density and current streamlines is as shown in Figure 3.13. An increase in the distortion of the potential distribution under the gate, relative to the $V_{ds} = 0.0$ and 1.0 volt cases, is observed, as is the higher field region over a wider area on the drain side of the gate. Due to this higher field, the velocities in the channel are greater and the carrier density continues to decrease under the gate, as shown in Figure 3.13b. The injection of carriers into the substrate is also increased, as is indicated by the density contours, Figure 3.13b, and the current streamlines, Figure 3.13c. Note that a more substantial fraction of the current now flows through the substrate.

The distributions under the source, gate and drain are shown for this bias level in Figures 3.14-3.16. The potential variation, Figures 3.14a - 3.16a, show that under the source only a small field is present in the region of the AlGaAs/InGaAs interface, as was the case for $V_{ds} = 1.0$. No significant field appears in the substrate in the direction normal to the source. However, under the gate, Figure 3.15a shows that a field forcing electrons towards the substrate exists, and this field is responsible for the current paths extending further into the substrate. Under the drain, the field in the substrate is reversed, drawing electrons back towards the channel and to the drain.

The density profiles shown in Figures 3.14b - 3.16b are similar to the $V_{ds} = 1.0$ volt case. However, we note that the peak in carrier density under the source is reduced, while the peak under the drain increases. This is, of course, consistent with the higher applied drain bias. Under the gate, the reduced peak density is evident, as is the longer tail of the profile, showing the injection of carriers into the substrate. Note that no significant electron transfer has yet occurred. The central valley carrier temperature under the gate has risen to 1.8 times the lattice temperature, or 540° K. This is not high enough to result in significant transfer. Finally, we see that the central valley velocity has risen to about 8×10^7 cm/sec under the gate.

For the $V_{gs} = 0.0$ volt cases just examined it is apparent that for V_{ds} of two volts and below no significant heating of the carriers occurs and the velocity in the channel under the gate increases in such a manner that when combined with the carrier density profile, the current shows a relatively linear characteristic vs V_{ds}. As V_{ds} increases further, to 3.0 volts, some *transfer* occurs and the current begins to saturate according to the simulations.

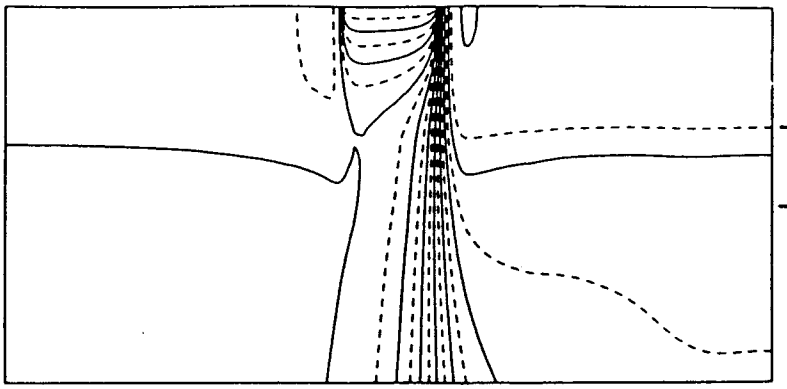

a) Potential.

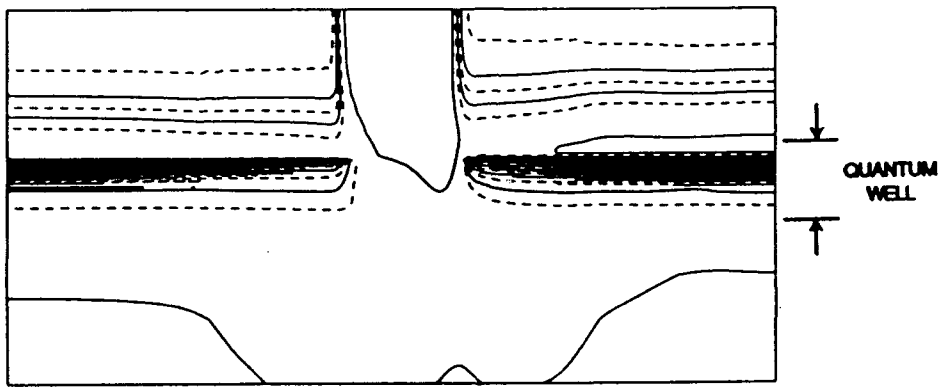

b) Electron Density.

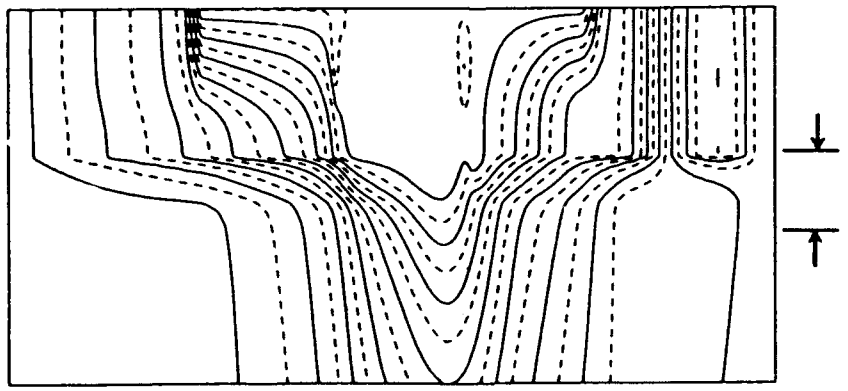

c) Current Streamlines.

Figure 3.13 Computed Contours for $V_{ds} = 2.0$ and $V_{gs} = 0.0$

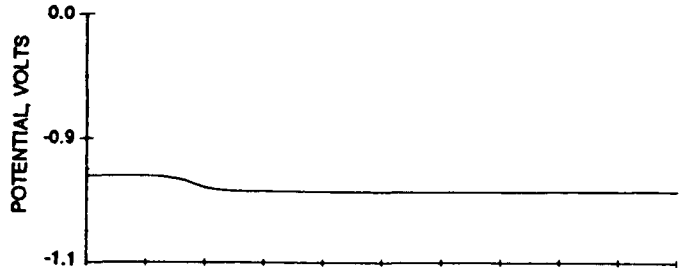

a) Potential.

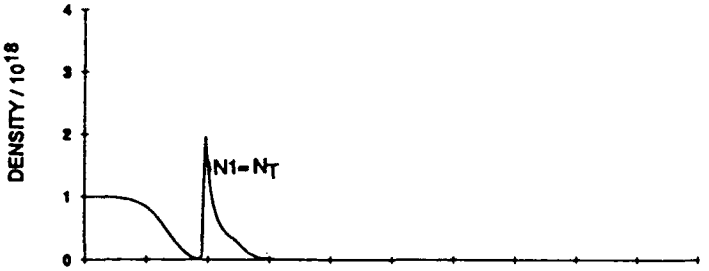

b) Electron Density.

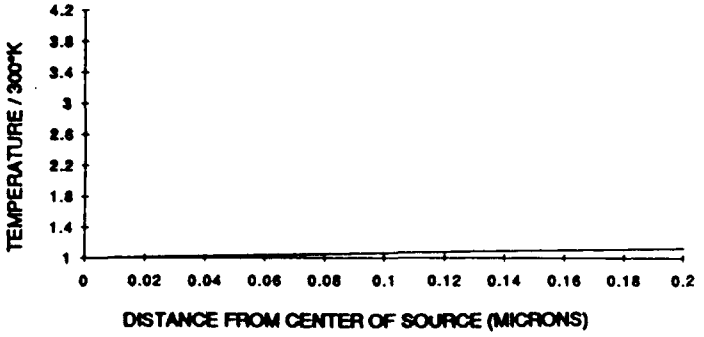

c) Gamma Valley Temperature.

Figure 3.14 Computed Distributions Normal to Center of Source for $V_{ds} = 2.0$ and $V_{gs} = 0.0$

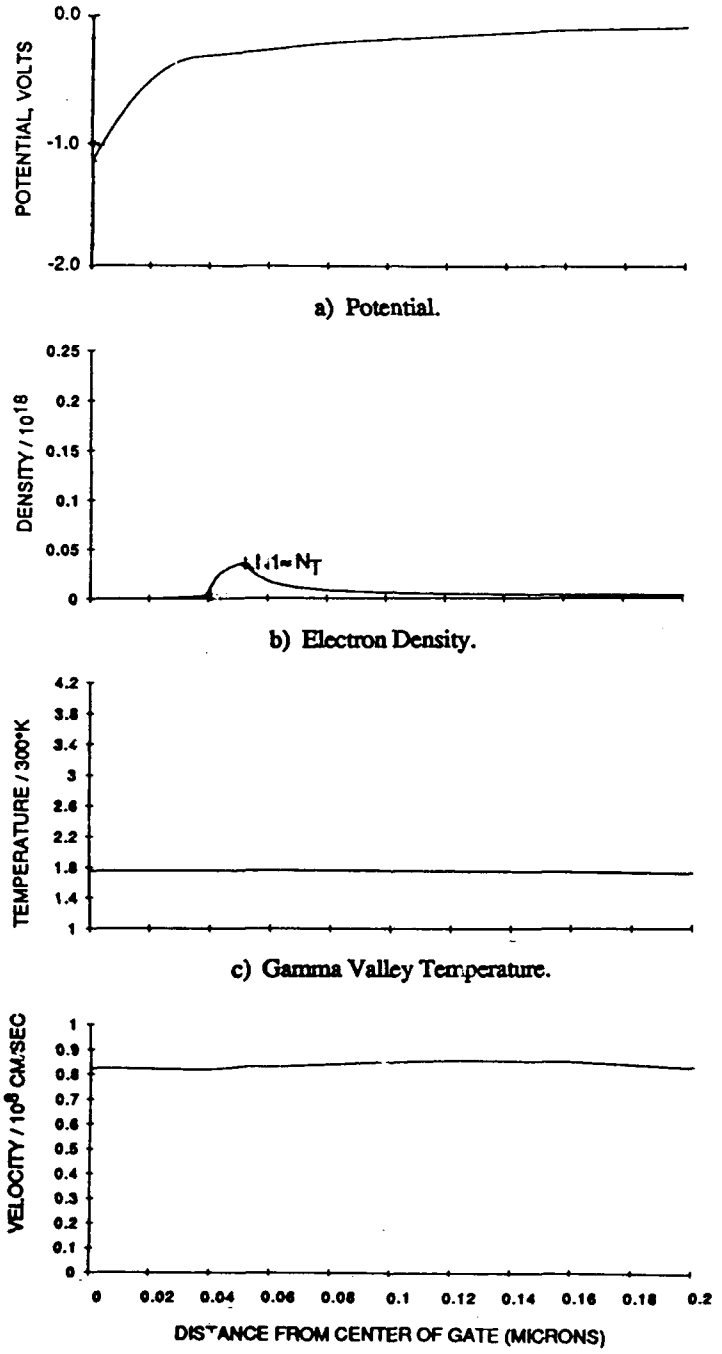

a) Potential.

b) Electron Density.

c) Gamma Valley Temperature.

d) Gamma Valley Horizontal Velocity Magnitude.

Figure 3.15 Computed Distributions Normal to Center of Gate for $V_{ds}=2.0$ and $V_{gs}=0.0$

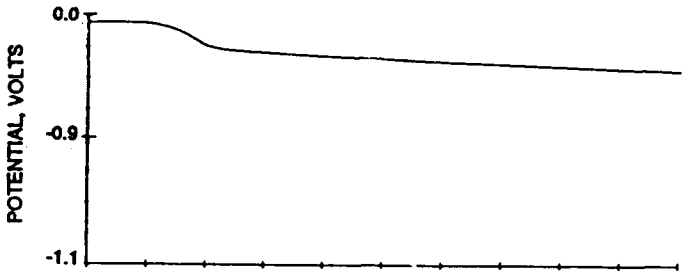

a) Potential.

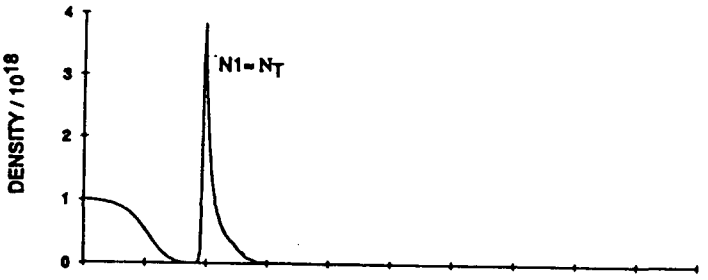

b) Electron Density.

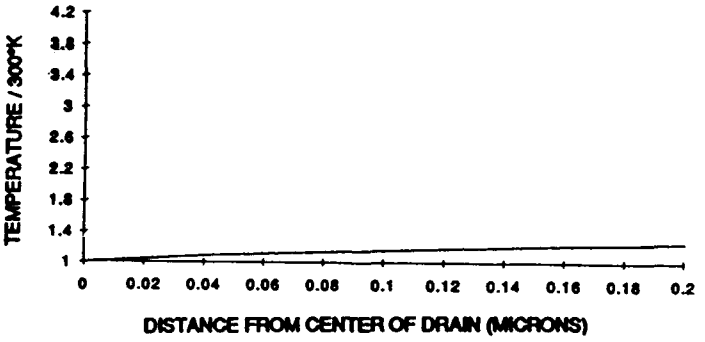

c) Gamma Valley Temperature.

Figure 3.16 Computed Distributions Normal to Center of Drain for $V_{ds} = 2.0$ and $V_{gs} = 0.0$

Steady State, V_{ds} = 2.0 v, V_{gs} = -1.0 v

When the gate bias was reduced to -1.0 volts, the drain current assumes negligible values for V_{ds} below 2.0 volts. Contour plots of the potential and electron density for this case are shown in Fig. 3.17. As shown in Figure 3.17a the potential and carrier distributions under the gate show an extended depletion region penetrating deep into the substrate. The channel is void of carriers under the gate and the device is effectively pinched off. This result is re-enforced in Figure 3.18, where profile plots under the gate are shown. The lack of any free electrons, even 2,000Å into the substrate, clearly shows there will be negligible current. Due to the applied drain potential, the velocity of what few electrons do flow is at a level of $2x10^7$cm/sec, but the net flux of electrons is approximately zero.

Steady State, V_{ds} = 1.0 v, V_{gs} = 0.4 v

When the gate bias is raised to 0.4 volts and the drain bias set at 1.0 volts, the contours of potential, density and current streamlines appear as shown in Figure 3.19. These results may be compared to Figure 3.9, for V_{gs} = 0.0 volts. The potential contours are more widely separated and the source to drain field increases more gradually than for the V_{gs} = 0.0 v case. It is also apparent that there is a greater potential drop between the InAlGa side of the channel and the drain contact. Since a higher current flows, more electrons must cross this barrier to reach the drain and more energy is required. The density contours clearly show the reduced depletion under the gate contact region. It is also evident from the extent of the heavily-shaded areas in this figure that the electron concentration in the 2 DEG is much greater at the drain end of the device. This is similar to the V_{gs} = 0.0 volt case, but more extreme. The current streamlines while qualitatively similar to the V_{gs} = 0 case, showing that the current flows primarily in the 2 DEG region, also show a signficant amount of current crowding on the *gate side* of the drain contact, leading to the possibility of premature breakdown in this region.

Of the profile plots normal to the gate shown in Figure 3.20, it is of particular interest to examine the electron density. With 0.4 volts forward bias on the gate, the density in the 2 DEG approaches $2.5x10^{17}/cm^3$ and it is apparent that the electrons in the heavily-doped AlGaAs layer are not fully depleted, as in the cases when V_{gs} = 0.0 v or below. Also note that the electron temperature under the gate is much higher than at V_{gs} = 0.0 v. Higher drain voltage results in further increases in electron temperature, and consequent electron transfer, and appears to be the largest contributor to the slope change in the current voltage characteristics, as displayed in figure 3.5.

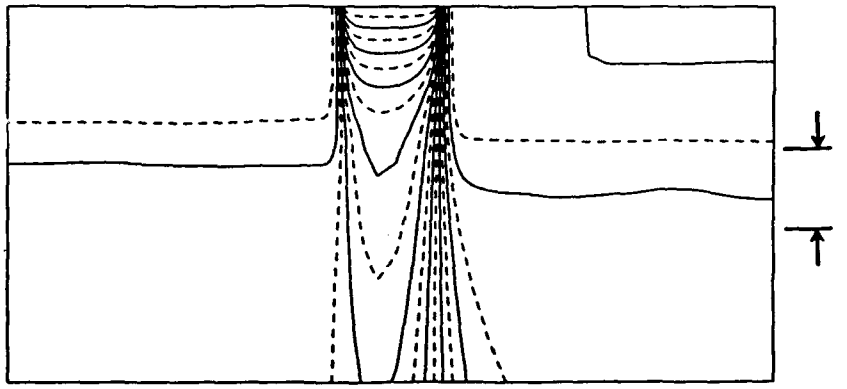

a) Potential.

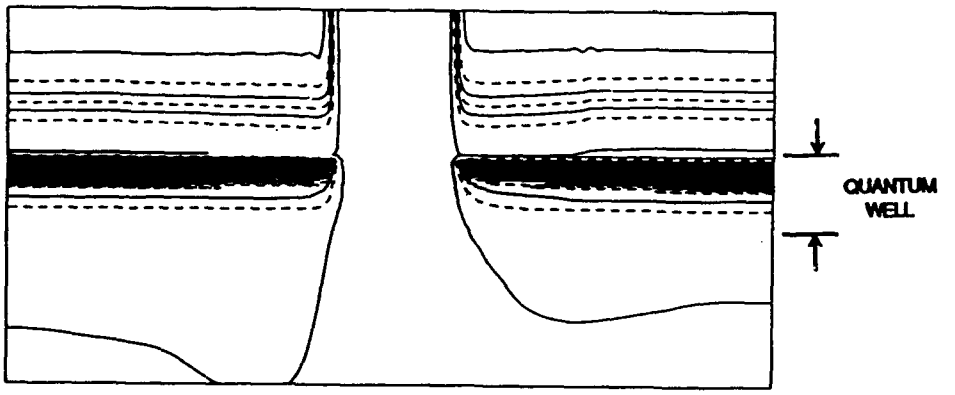

b) Electron Density.

Figure 3.17 Computed Contours for $V_{ds} = 1.0$ and $V_{gs} = -1.0$

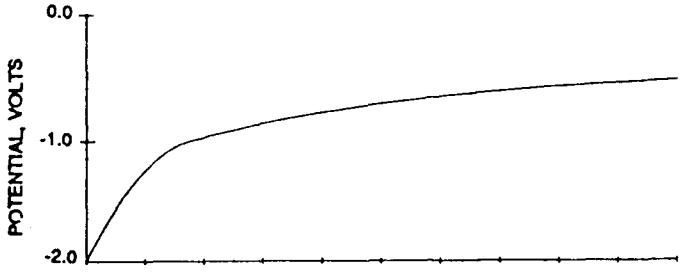

a) Potential.

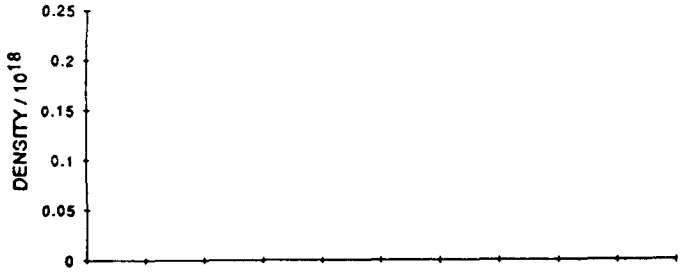

b) Electron Density.

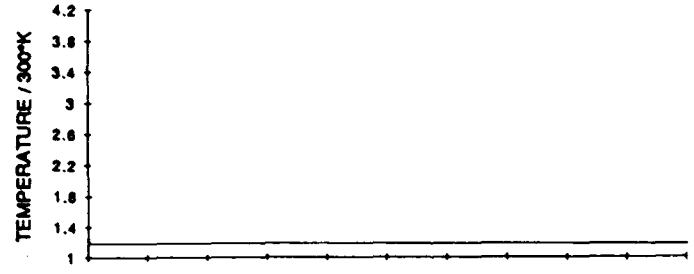

c) Gamma Valley Temperature.

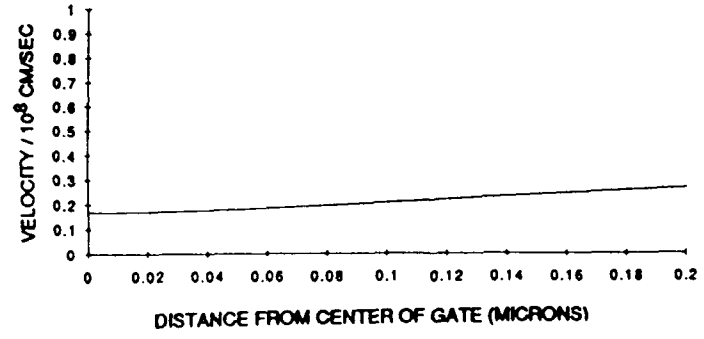

d) Gamma Valley Horizontal Velocity Magnitude.

Figure 3.18 Computed Distributions Normal to Center of Gate for $V_{ds} = 1.0$ and $V_{gs} = -1.0$

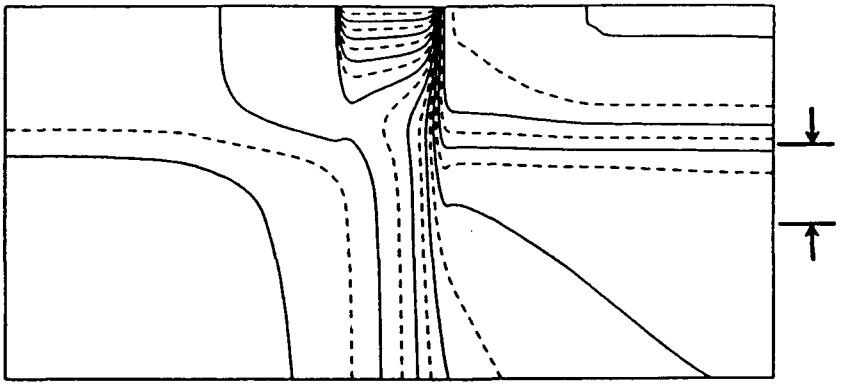

a) Potential.

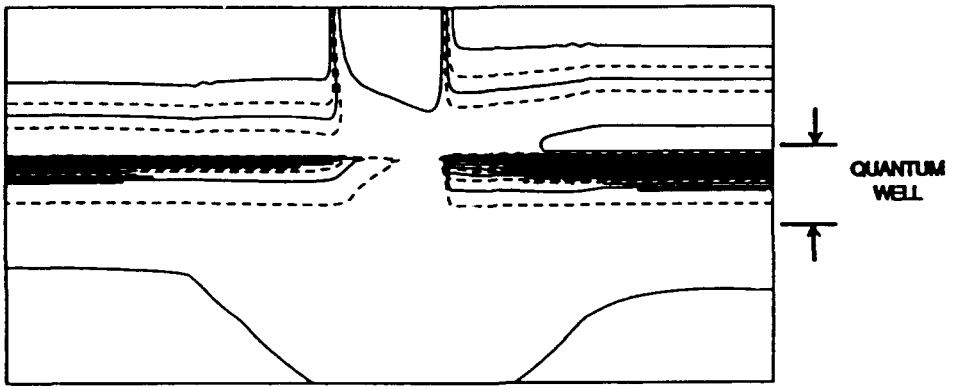

b) Electron Density.

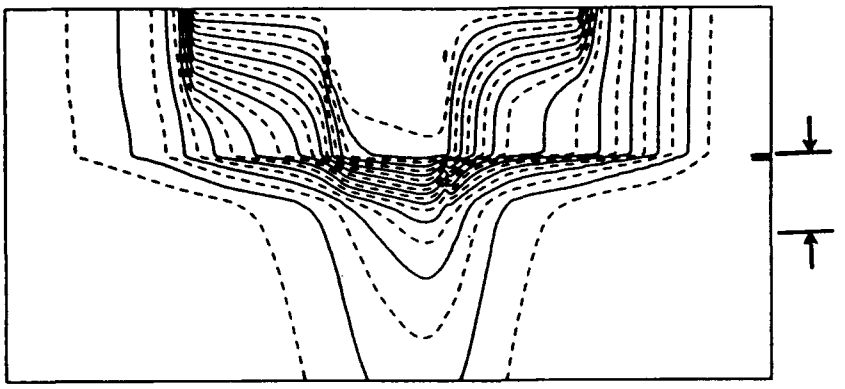

c) Current Streamlines.

Figure 3.19 Computed Contours for $V_{ds} = 1.0$ and $V_{gs} = 0.4$

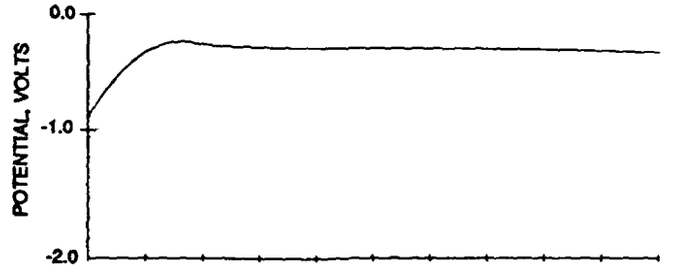

a) Potential.

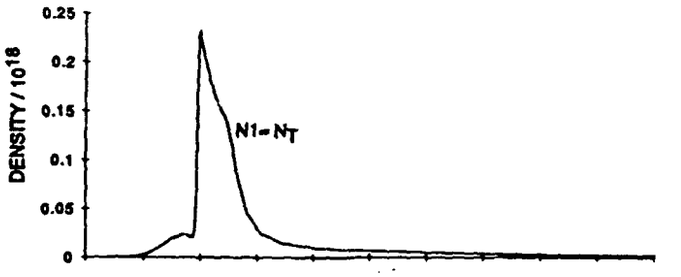

b) Electron Density.

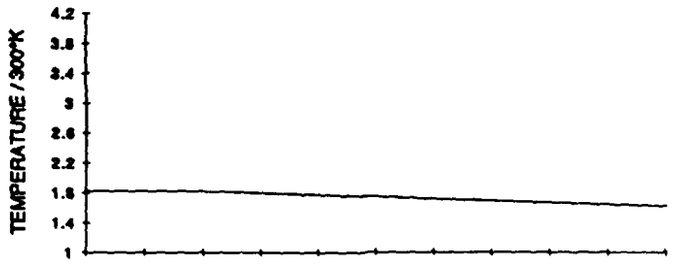

c) Gamma Valley Temperature.

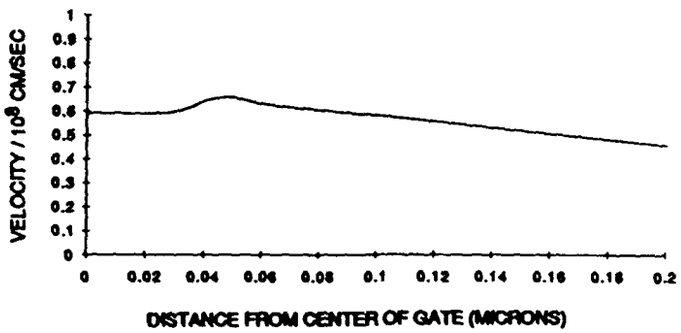

d) Gamma Valley Horizontal Velocity Magnitude.

Figure 3.20 Computed Distributions Normal to Center of Gate for $V_{ds}=1.0$ and $V_{gs}=0.4$

Steady State, $V_{ds}=3.0$ v, $V_{gs}=0.4$ v

When the drain voltage is raised to 3.0 volts, with $V_{gs}=0.4$, the results are as shown in Figure 3.21. The effect of the increased drain bias dominates the potential distribution in the channel, creating a broad region of high field in the source drain direction. The density distribution shows a reduction in the density levels at the source end of the 2 DEG and under the gate. Additionally, at the drain side of the device the electrons accumulate at the extreme right side of the device, under the drain. The current streamlines show a deeper penetration into the substrate, which is characteristic of increasing the drain bias level, and further current crowding.

Distribution normal to the gate, shown in Figure 3.22, indicates substantial electron transfer and a central valley electron temperature near 1260° K. Further there is a large spread of the charge into the quantum well. While there is a reduction in the net charge under the gate the central valley velocity reaches $8x10^7$ cm/sec, and is in major part responsible for the increased current flow at this bias level. The high degree of electron transfer, due to the high current flow and increased drain bias, gives rise to the current saturation observed in the current voltage characteristics shown in Figure 3.5. In addition, it is pointed out that when electron transfer occurs there is a substantial increase in the effective mass. Quantum transport calculations indicate that this increase in effective mass reduces the population of the quantized two dimensional electron gas. While this quantization is not incorporated in this study; a reduction in the current levels should accompany this change.

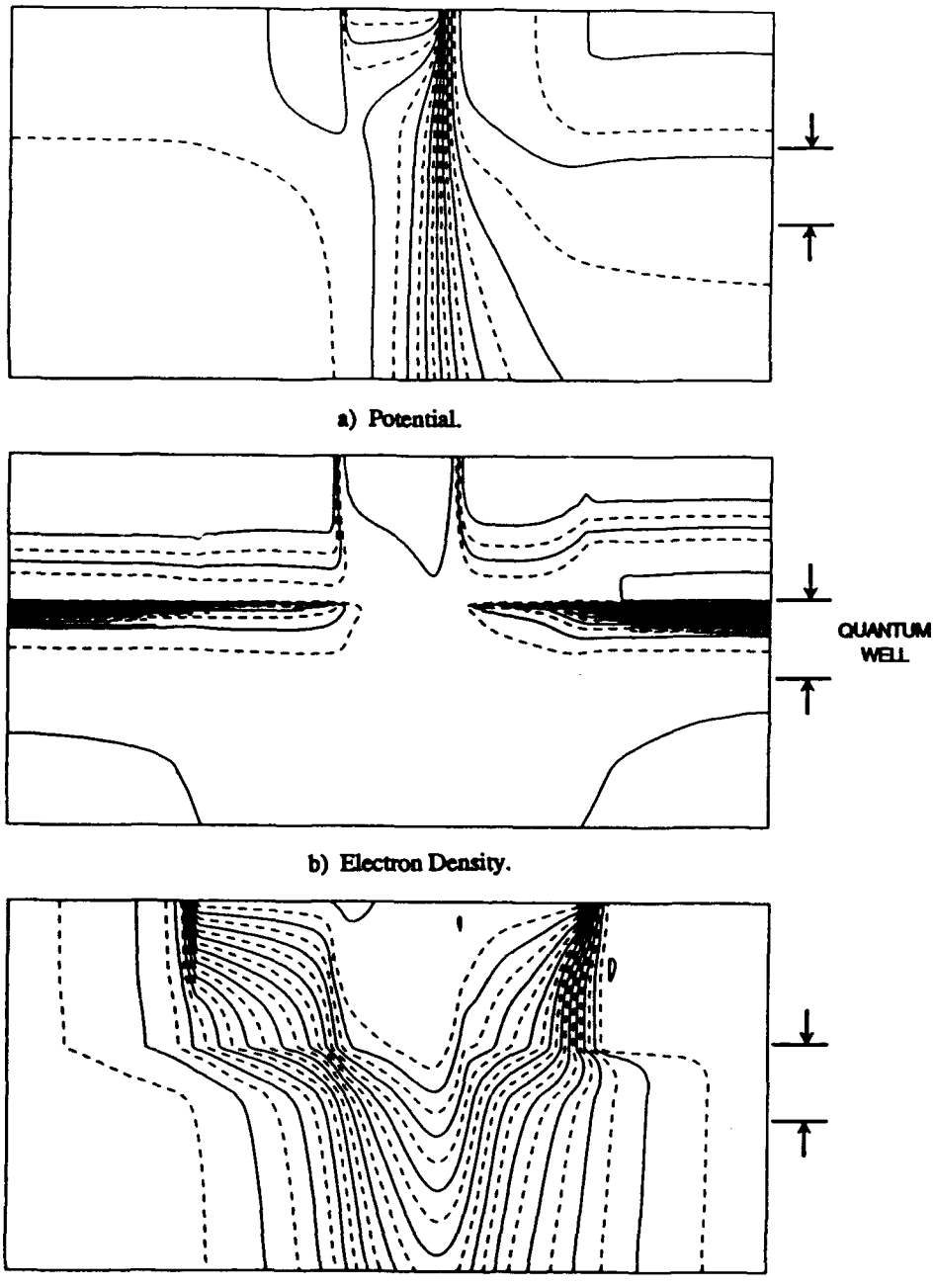

a) Potential.

b) Electron Density.

c) Current Streamlines.

Figure 3.21 Computed Contours for $V_{ds}=3.0$ and $V_{gs}=0.4$

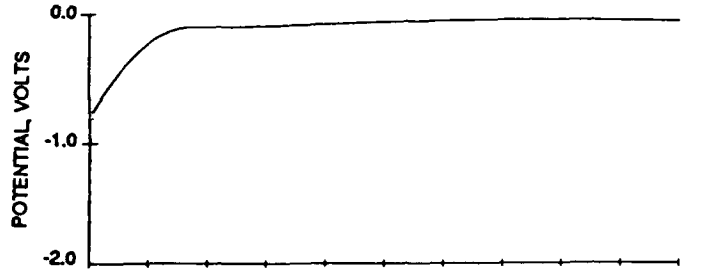

a) Potential.

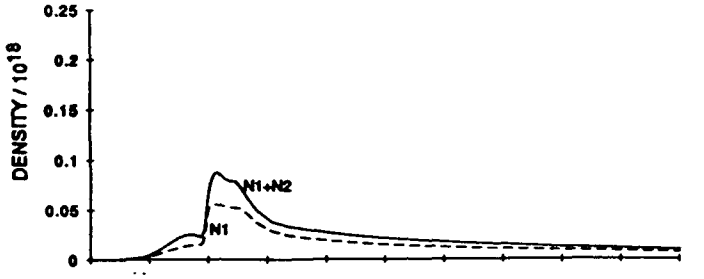

b) Electron Density.

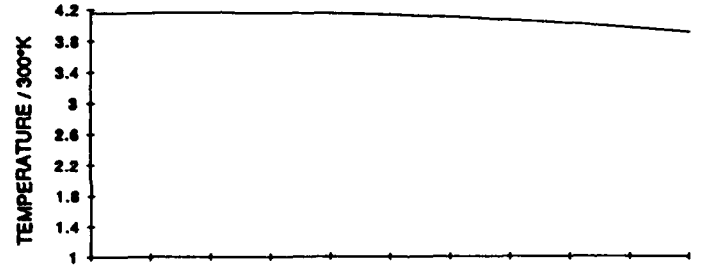

c) Gamma Valley Temperature.

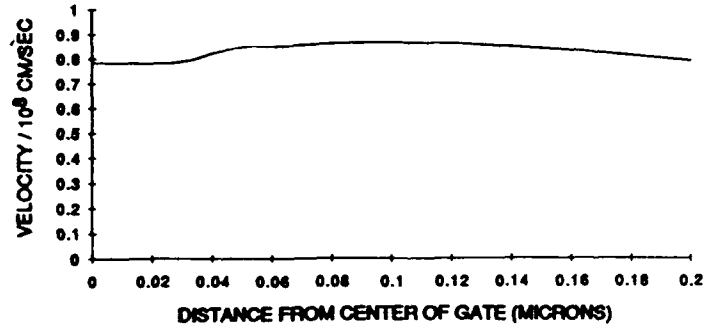

d) Gamma Valley Horizontal Velocity Magnitude.

Figure 3.22 Computed Distributions Normal to Center of Gate for $V_{ds} = 3.0$ and $V_{gs} = 0.4$

4. Transient Simulations of the Pseudomorphic HEMT

Introduction

Perhaps one of the most significant features of the ability to perform transient calculations with either the moments of the Boltzmann transport equation or Monte Carlo methods is that the effects of velocity overshoot on the transient behavior of the devices can be determined. It is recalled that in the early seventies the initial work of Ruch (1972) suggested the possibility of very short time scale devices. Subsequent work by others, (see e.g., Grubin, et al, 1982) indicated that high speeds may not necessarily be attainable since the mechanism for relaxation involved several time scales, (i) the momentum relaxation time and (ii) the energy relaxation time. There is also an intervalley intervally scattering rate to contend with. Finally there is the fact that it takes a finite amount of time to charge a capacitor and that the displacement currents must be accounted form. In an earlier study, Grubin and Kreskovsky (1985) demonstrated that on the time scales of interest the transients associated with the displacement currents are of the same order as the transient hot electron time scales. Thus the simplest question to ask is : *How will the PHEMT respond to sudden and/or controlled changes in the time dependent applied bias?* This question is addressed below.

The first set of calculations discussed involves the response of the PHEMT structure to *sudden* changes in bias. This is followed by a set of calculations involving a *controlled* rate of change of bias.

$V_{gs} = +0.4$ *v; Drain Bias is Switched from 1.0 v to 2.0 v in Zero Time*

Several transient simulations were performed to assess the effects of switching of the drain bias. The first calculation involves a switch in the drain bias from *1.0 volt to 2.0 volts, while the gate bias was maintained at 0.4 volts.* The response of the contact currents is shown in Figure 4.1.

Figure 4.1a shows the response of the total current (conduction plus displacement) at the source, gate and drain. Note that the peak in the drain current is clipped in the plot. The convention used here is that *positive* gate and drain current represents electrons flow out of the structure. *Negative* current at the source represents electrons flowing into the device. At 1.1 psec the gate current is approximately zero while the source and drain currents are approximately equal in magnitude but opposite in sign.

While the response was not carried out to a completely steady result, the current transients indicate several features. The overall transient has a *time scale on the order of several picoseconds and appears to be governed by the gate capacitance.* From the gate response, it

is apparent that the gate current displays an initial transient with a characteristic oscillation at a frequency of the order of two THz. The pattern of current flow indicates, for this transient, that there is strong current and charge coupling through the interaction of the gate and drain regions. However, the drain, which closely follows the gate response, also sustains a higher frequency oscillation of the order of ten THz; this higher frequency response is a consequence of its interaction with the source region.

Examination of the displacement currents in Figure 20b indicates *the origin of these high frequency components of the currents are the rapidly changing levels of charge in the 2 DEG under the source and drain.* As was shown in previous figures, the electron distribution exhibits large peaks at the material interfaces under the source and drain. The magnitude of these peaks was shown to be highly dependent on the drain bias level. Thus, a step change in drain bias results in a readjustment of the charge distribution in this region, giving rise to these capacitance effects.

Further evidence of this effect is presented in Figure 4.2, where the time variation of various parameters at a given point within the device are shown. In Figure 4.2 the plots are labeled "point no. 1", etc. This notation refers to the location within the device where the data was recorded. These locations are indicated in Figure 3.6. Point 1 is within the InGaAs channel *under the source*, point 2 within the channel near the *drain end of the gate*, and point 3 within the channel *under the drain.* The results at points 1 and 3, under the source and drain, respectively, show that there is very little transient effect on the central valley temperature, T1, or velocity magnitude, Q1. However, the central valley density, N1, shows a significant transient effect with variations on the time scale associated with the displacement currents at the source and drain. These transients settle out in about a picosecond. Under the gate a more significant effect is observed. The velocity magnitude, Q1, increases significantly and the density drops. The potential at this point also rises approximately 0.6 volts. Recall that point 2 is located in the high field region, on the drain side of the gate. While these three quantities vary dramatically, it is observed that the transients are smooth without the high frequency components observed at the source and drain. This is because we are dealing with transients associated with length scales along the channel, i.e., the source-drain spacing. Under the source and drain, the relevant length scale is that associated with the accumulation layer at the material interface, i.e., the 2 DEG channel depth. We note also that at point 2 the transients also decay in approximately a picosecond, with the exception of the central valley temperature. As we shall see, the time scale for the temperature to adjust to the bias change is somewhat longer, on the order of 3 picoseconds. *It is this 3 picosecond time scale that determines the time to relaxation for the PHEMT.*

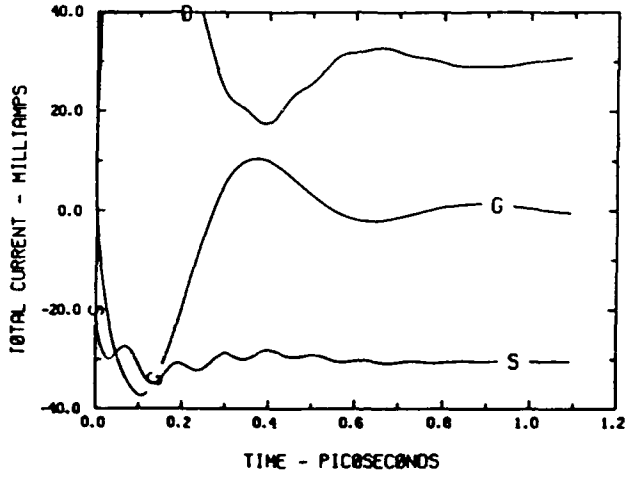

a) Total Current.

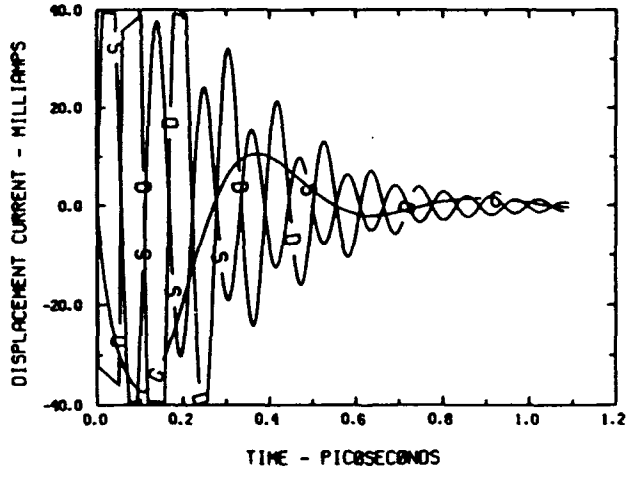

b) Displacement Current.

Figure 4.1 Transient Response for a Change in Bias, V_{ds} = 1.0 to 2.0 and V_{gs} = 0.4

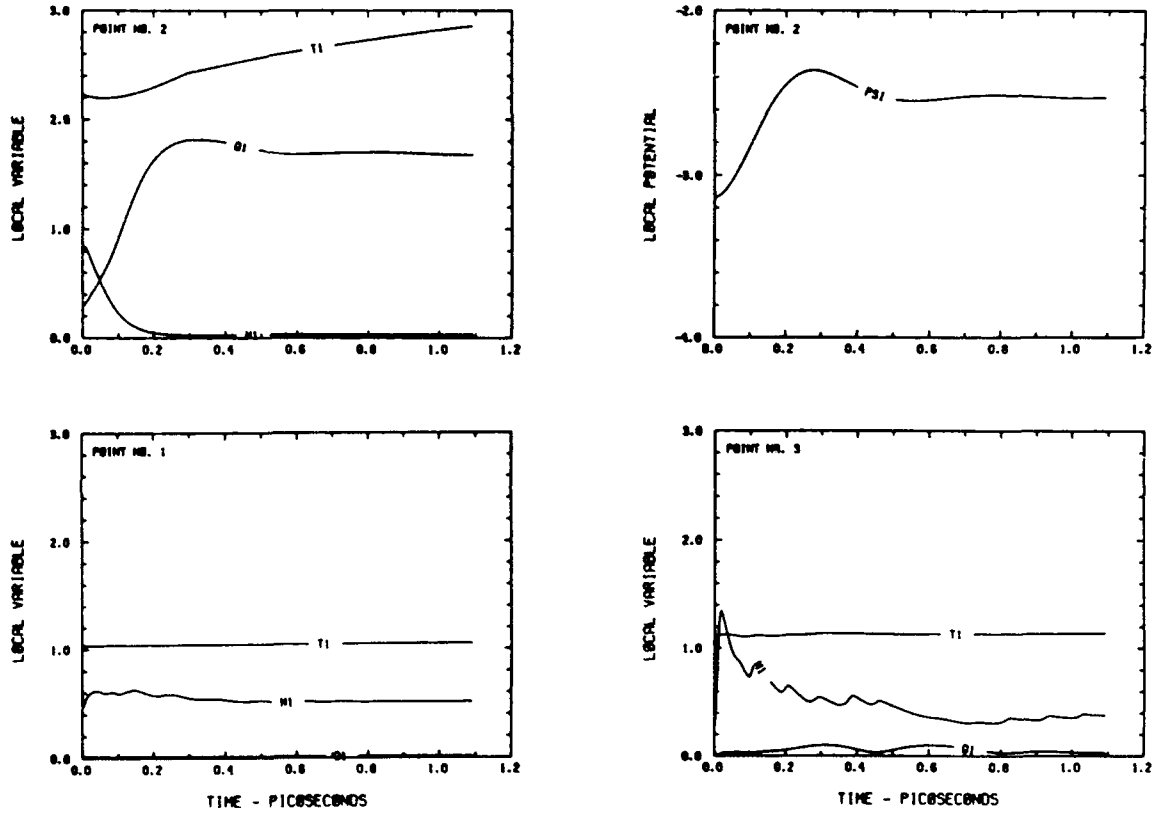

Figure 4.2 Transient Response for a Change in Bias, V_{ds} = 1.0 to 2.0 and V_{gs} = 0.4

V_{gs} = *+0.4 v; Drain Bias is Switched from 1.5 v to 3.0 v in Zero Time*

The results of a similar transient simulation, but with a *greater change in the drain voltage, from 1.5 to 3.0 volts, are shown in Figures 4.3 and 4.4.* These figures exhibit the same characteristics and time scales discussed previously. However, this simulation was extended in time to 3.0 picoseconds. In Figure 4.4 the temperature variation at point 2 clearly reaches a new steady value after 3.0 picoseconds. The results shown in Figures 4.1-4.4 show that switching time of the device is controlled by the thermal energy relaxation time. This is not unexpected, since these relaxation times are the longest.

What is the significance of the above result? It is recalled that during the Phase I study it was argued that the speed of a device is *the time it takes the device response to fall within 5%-10% of its steady state response corresponding to those bias conditions.* The results of the Phase II study indicate that for this specific structure, the time determining the response is the *longest response time*, which is the energy relaxation time. Since momentum relaxation occurs on a much shorter time scale than the relaxation of the electron temperature, energy relaxation in this study is dominated by temperature relaxation. In the above calculations, energy relaxation is represented as being somewhat greater than 3 ps. As a consequence of this if a signal is placed on one of the contacts with a period that is of the order of the energy relaxation time or shorter, that the transport quantities will initially deviate from their steady state values, and ultimately will adjust to periodic values that will differ signficantly from their steady state values. Figure 4.5 displays the results of such a calculation.

$V_{ds} = 3.0\,v,\ V_{gs}(t) = V_{gs}(t + 5.0ps);\ V_{gs} = 0.4 \pm 0.4[1\text{-}exp\text{-}t/(1ps)],\ 0 < t < 2.5ps.$

Figure 4.5 displays the response of the PHEMT to a exponentially rising and decaying gate voltage. Figure 4.5a is a sketch of the applied gate bias which is periodic with a period of the order of the energy relaxation time. The total current through the three contacts is displayed in figure 4.5b. Note that the source current appears to saturate after 1.0 ps, while the gate voltage continues to decrease; and over this same time interval the drain current decreases. Similarly, there is a decreasing gate current over this time interval, suggesting again strong coupling between the gate and the drain regions.

The displacement currents through the source and drain regions are displayed in figure 4.5c. The displacements currents which are qualitatively similar to that discussed in connection with sudden changes in bias, occur when the voltage changes across the gate are at their steepest variation, and suggest that their origin is in the oscillation of the charge density in the 2DEG.

In the calculations associated with the sudden voltage change the high frequency

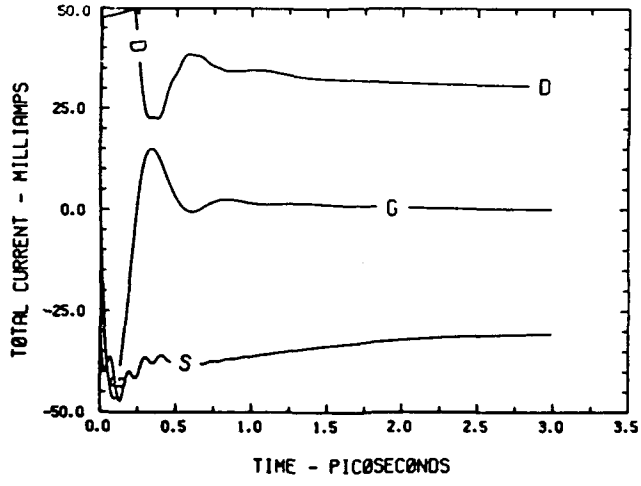

a) Total Current.

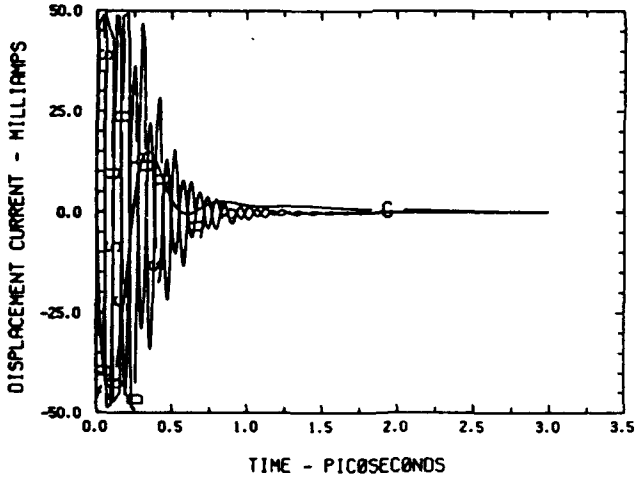

b) Displacement Current.

Figure 4.3 Transient Response for a Change in Bias, V_{ds} = 1.5 to 4.0 and V_{gs} = 0.4

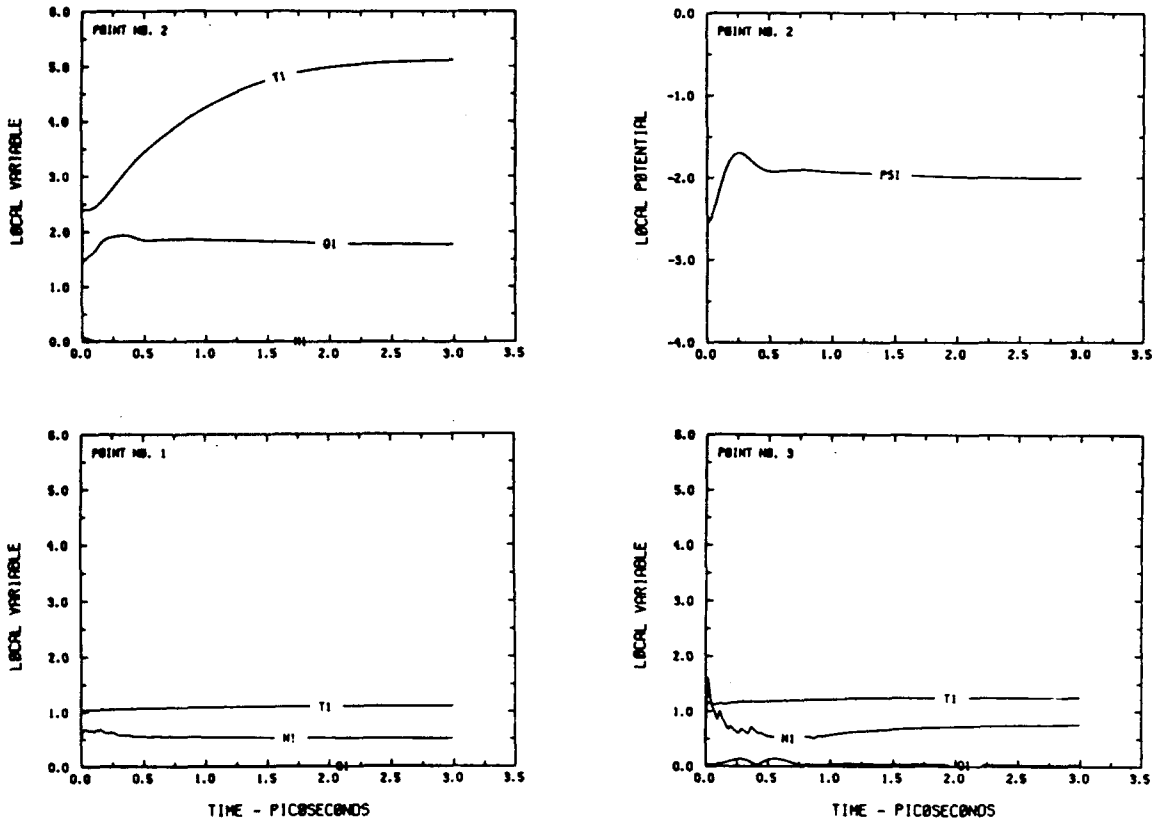

Figure 4.4 Transient Response for a Change in Bias, V_{ds} = 1.5 to 4.0 and V_{gs} = 0.4

charge density variations occured in the 2 DEG within the source and drain regions. The variation of the charge under the gate is dominated by the gate contact. For the calculation here, we display the density, temperature, magnitude of velocity, and potential variation at point '2' of figure 3.6. The steady state results, which incorporate velocity overshoot, show an additional enhancement of velocity overshoot, along with substantial changes in the temperature of the carriers. The carrier velocity, while not periodic, tends to show structure at the end of the 10 ps cycle, indicating that is closely following the changes in gate bias. The electron temperature variation does not display a full two cycles at the end of 10 ps, an indication that the relaxation effects require a longer time to settle in. After some point in time all of the relevant quantities such as energy, density, temperature, etc., will be periodic with a period of 5 ps. At this point the temperature will undergo smaller excursions. While the oscillation has not yet settled to a steady state oscillation, the results again indicate that the charge variations under the gate are determined by the time dependence of the gate contact, but that the oscillation in the region of the source and drain contacts are significantly modified by the high frequency charge density oscillations.

The principle *conclusion of the transient calculation* is that the time to relaxation of the structure is dominated by the longest relaxation time, which for this structure and material is the energy relaxation time; and that this relaxation time will dominate all time dependent oscillatory behavior.

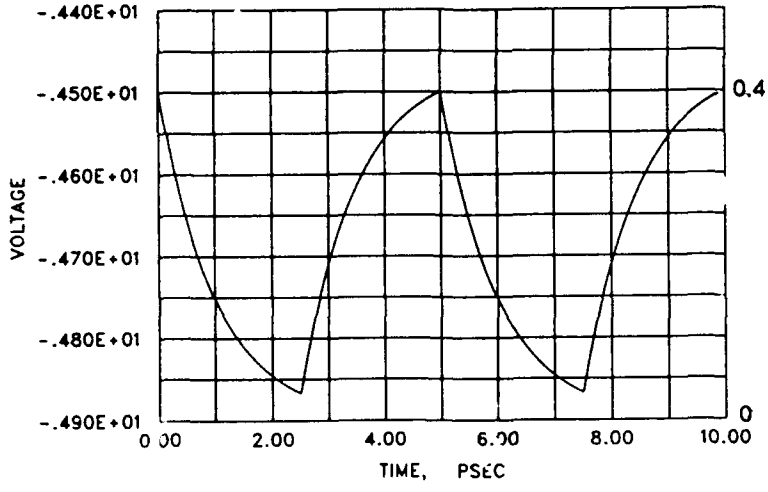

Figure 4.5a Time dependent gate voltage on the PHEMT for a fixed drain voltage of 3.0 v.

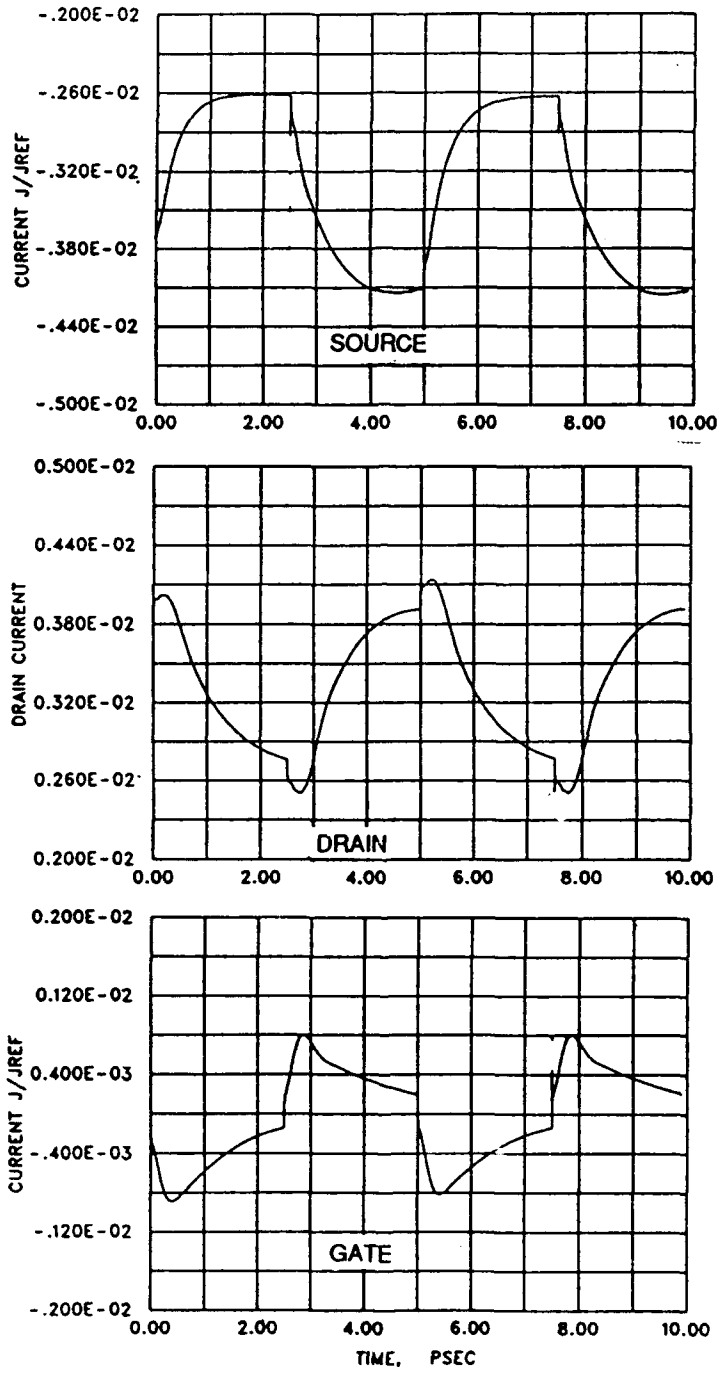

Figure 4.5b Total current out of all three contacts following the time dependent imposition of the gate voltage of figure 4.5a

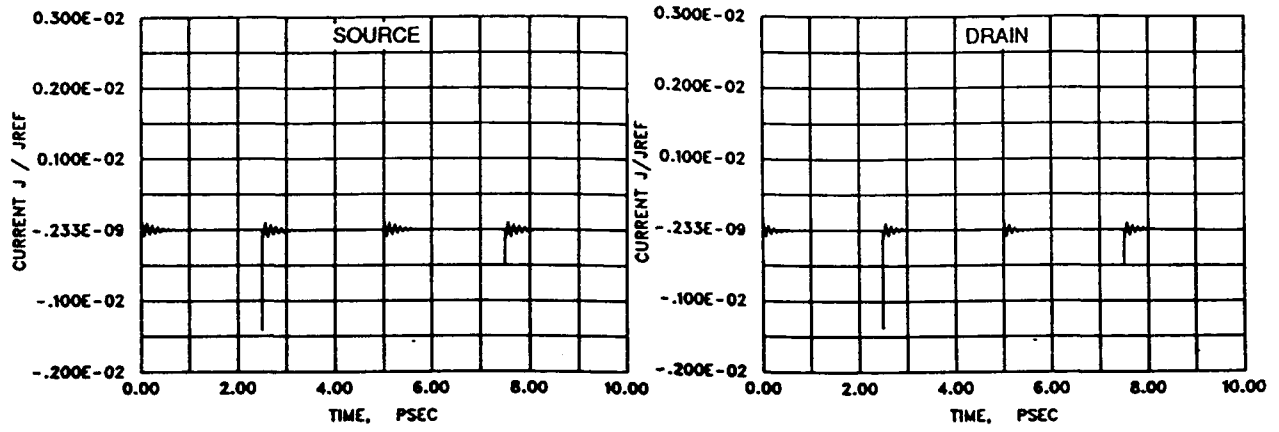

Figure 4.5c Displacement current out of the source and drain contacts following the time dependent imposition of the gate voltage of figure 4.5a

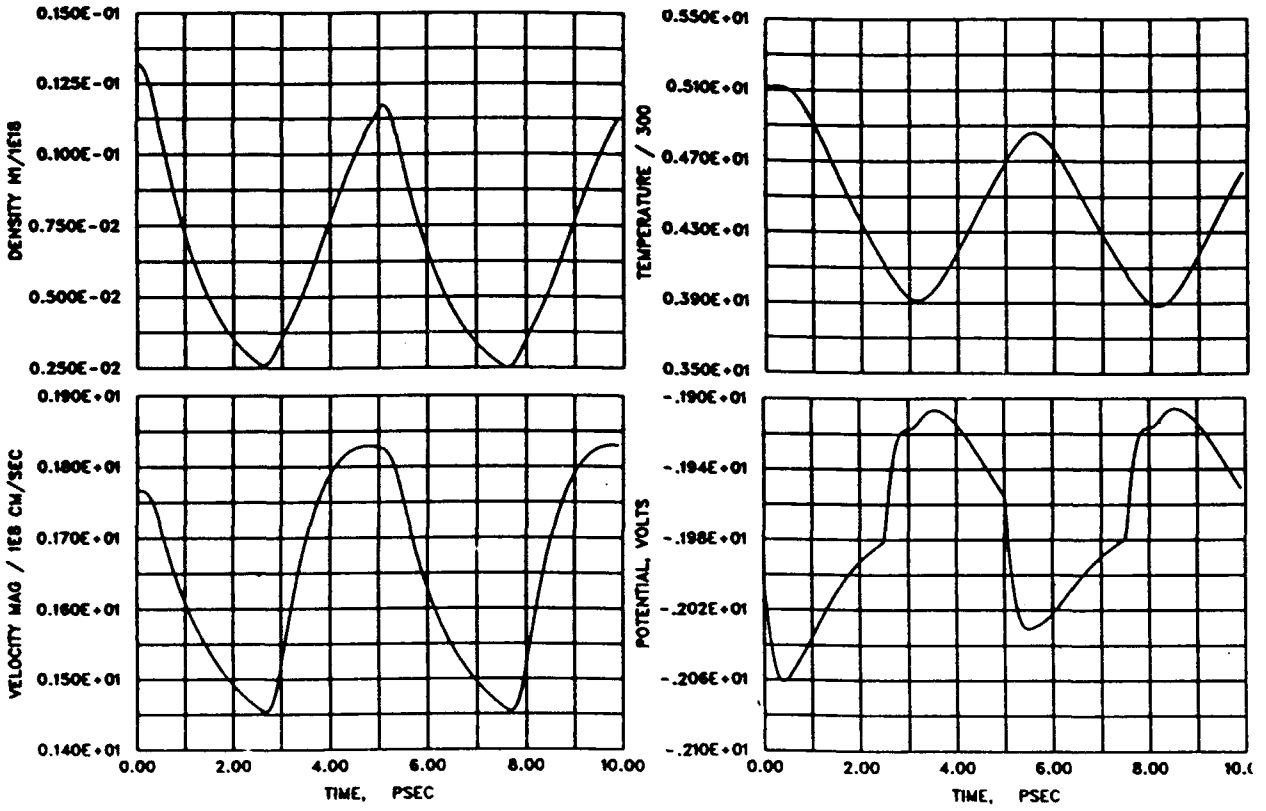

Figure 4.5d Density, temperature, velocity magnitude, and potential at point '2' following the time dependent imposition of the gate voltage of figure 4.5a

5. Monte Carlo Simulations

Introduction

This section is concerned with the development of Monte Carlo procedures for examining transport in FETs. The basic question we asked is why perform Monte Carlo calculations at all; and more specifically why perform them as part of this study. There are several compelling reasons: *First*, MC procedures offer the best means of determining the exact form of the distribution function for semiclassical structures. The moments of the Boltzmann transport equation discussed in the previous sections start off assuming a specific form for the distribution function. *Second*, when transients are incorporated, the exact form of the distribution function tends to reveal transient transport effects not apparent from the moment studies. *Third*, MC procedures offer a check on the assumptions used in the moment formulation; and hence provide a means through which the scattering parameters and dissipation mechanisms can be more representatively handled using the moment methods. This third reason evolved into the primary motivating factor of incorporating the MC procedures in the study, particularly when it was recognized that the transient calculations could be examined more efficiently for complex structures using moment rather than MC procedures. All calculations were for GaAs using standard GaAs parametric values, see, e.g., Grubin (1988).

The discussion that follows describes the evolution of the MC development and its application to FETS. All calculations performed were for two dimensional structures; although initially the two dimensional structure was a two terminal diode with one dimensional symmetry. Performing two dimensional MC simulations on a one dimensional structure permitted us to expose the problems associated with MC methods without introducing complications associated with two dimensional boundary condition effects. Parallel MC and moment calculations were performed for the FET.

Diode Simulations

As discussed above, prior to applying the Monte Carlo simulation procedure to a three-terminal device, such as an FET, the procedure was applied to a two-terminal, uniformly-doped device. The device, shown in Figure 5.1, is 0.2 μm wide with a source drain spacing of 0.5 μm, and is uniformly doped to $2 \times 10^{17}/cm^3$. In this calculation the component 'z' is between the source and the drain, while the component 'x' is normal to 'z'. *We note that while this structure would yield one-dimensional solutions using a drift and diffusion or MBTE approach, the Monte Carlo solution may exhibit some two dimensionality in the solution when a "snapshot" of the solution is taken at any given instant.* However, when averaged over time appropriately the one-dimensional nature of the solution is revealed. This is realized as we examine the solutions for this structure.

The one dimensional calculations are summarized by current voltage characteristics that are nonlinear and reflect the nonuniform distribution of carriers in the structure. Figure 5.2 is the predicted current-voltage characteristic for the structure. (The details of the current calculation are discussed in the FET (next) section.) From this result it is apparent that the low field mobility, as determined from the slope of the curve near the origin, is approximately 2,500 cm/volt-sec. This value is in reasonable agreement with that reported by others. We also note that the current reaches a level of 1160A/m at a bias of 1.0 volt. This yields a mean velocity $<v> = (j/e)/(2x10^{17}/cm^3) = 1.8x10^7$ cm/sec for a mean field $<F> = (1.0\ v)/(0.5\ \mu m) = 20$ kv/cm, and reflects the non-equilibrium nature of the transport within the device.

Figure 5.3 shows the distribution of the components of velocity in the x and z directions and the energy level of carriers in the gamma valley as a function of distance (z) between the cathode (z = 0) and the anode (z = .5). Consider figure 5.3a which is a representation of the x component of Γ valley velocity. *The x component is parallel to the contacts.* As discussed above two dimensional calculations were performed for a two terminal device with one dimensional symmetry. Thus the x component of velocity should fill a three dimensional array with side: (v_x, x, z) as shown in the inset of figure 5.3a. The distribution of points in figure 5.3a represents a projection of all points in the MC simulation onto one plane. Each point in this figure represents one particle, and it is apparent that the x component of velocity sustains a mean value of zero. While the mean x component of velocity is zero, we observe random fluctuations as great as $\pm 9.8 \times 10^7$ cm/sec. However, the majority of particles are in the range of $\pm 2.8 \times 10^7$ cm/sec. We also note a lower population of gamma valley particles towards the anode (z = 0.5). This is due to transfer to the upper valley.

Figure 5.3b shows a projection onto one plane of the z component of velocity. Here the mean value of the velocity of gamma valley carriers is near 5.6×10^7 cm/sec in the middle of the device, a value consistent with the results of Grubin and Ferry [ ] for a field near 20 kv/cm. Towards the anode end of the device the gamma valley carrier velocity is somewhat higher, but fewer carriers remain in this valley.

Figure 5.3c displays a projection of the energy distribution for the gamma valley carriers. The carriers enter in equilibrium with the lattice and gain energy under the influence of the applied field, remaining within the gamma valley for nearly 60% of the structure. The population decreases significantly as the carriers approach the anode.

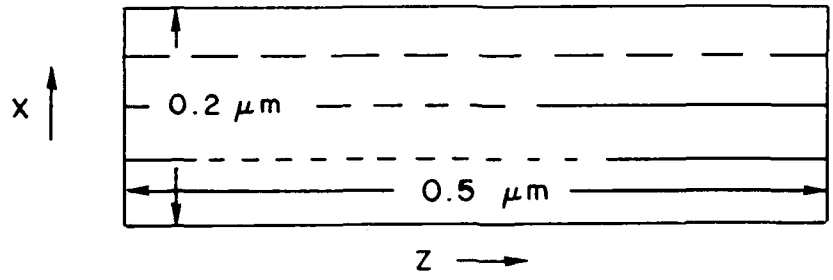

Figure 5.1 Sketch of the one dimensional diode structure used in the Monte Carlo studies.

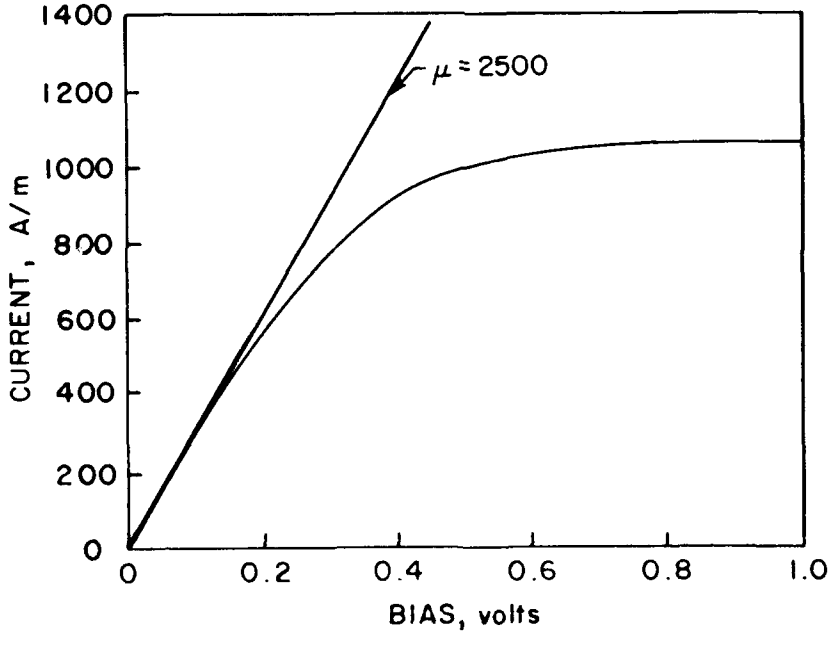

Figure 5.2 Sketch of current versus voltage for the structure used in the Monte Carlo studies.

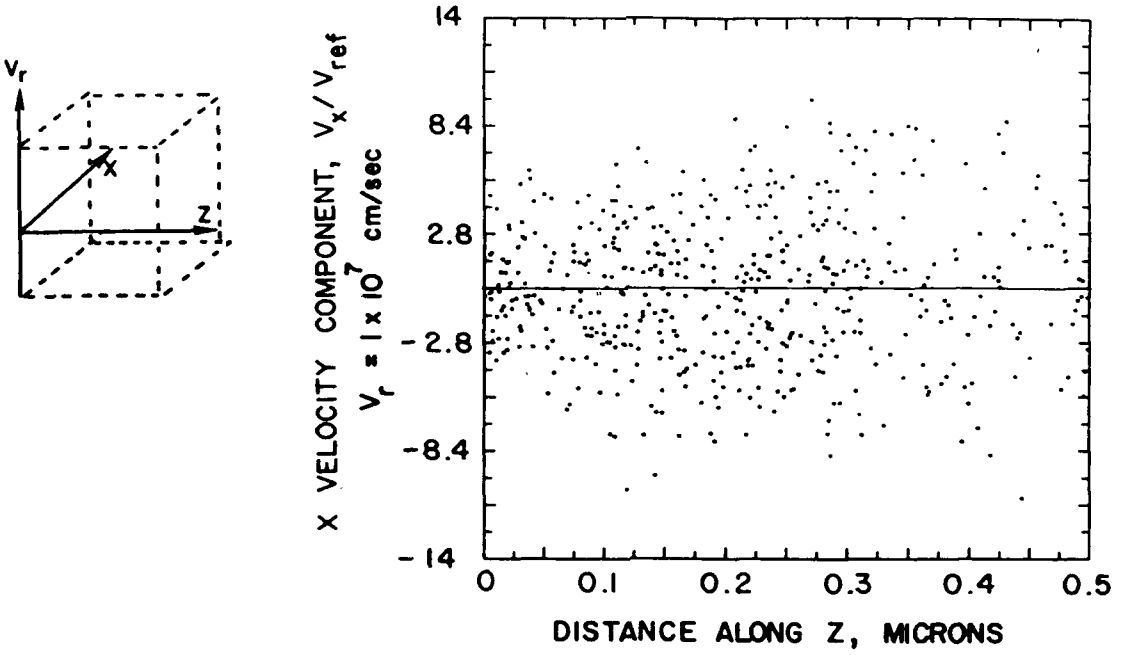

Figure 5.3a Projection of the distribution of Γ velocity in the 'x' direction for a bias of 1.0v.

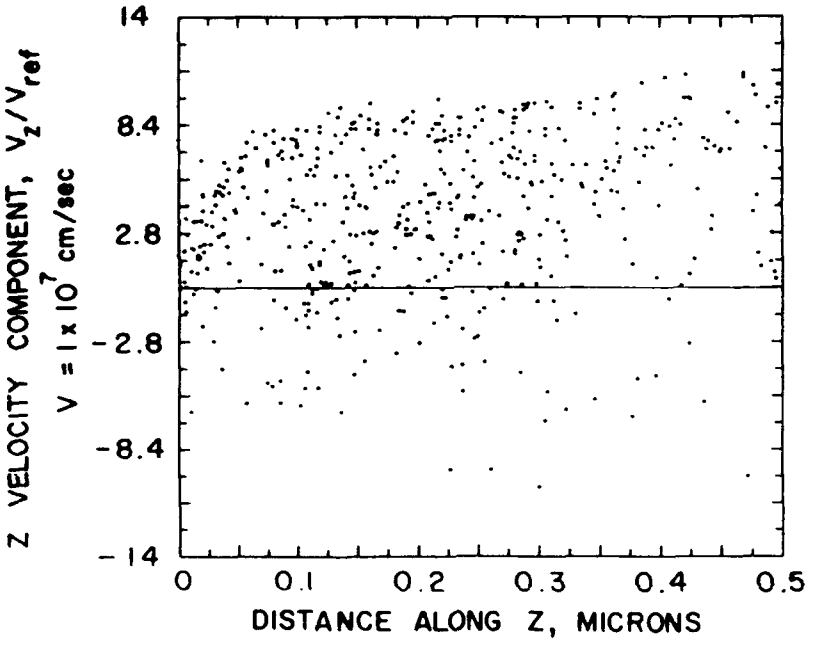

Figure 5.3b Projection of the distribution of Γ velocity in the 'z' direction for a bias of 1.0v.

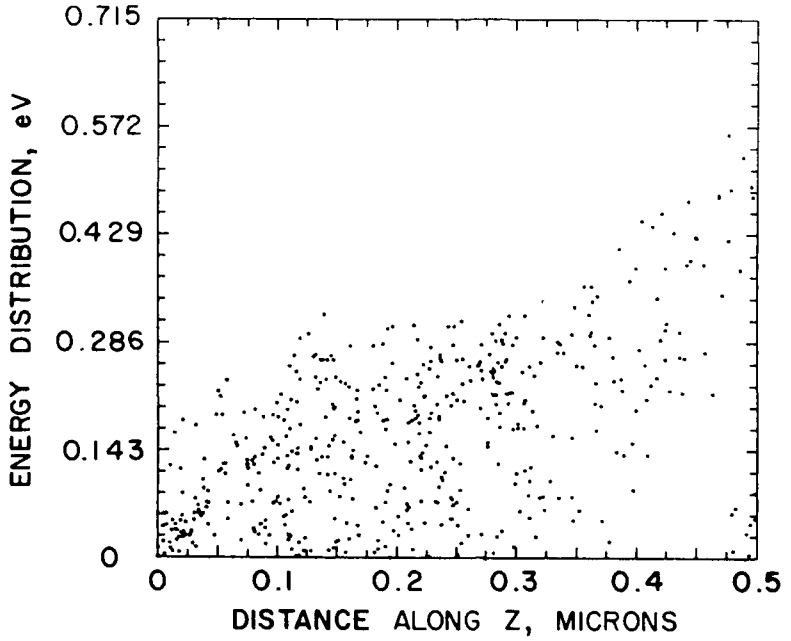

Figure 5.3c Projection of the distribution of Γ energy in the 'z' direction for a bias of 1.0v.

Figures 5.4 show similar plots for L valley carriers. The first observation in all of the plots shown in Figure 4 is the increasing population of L valley carriers as the anode is approached. The x component of velocity, as in the gamma valley result, exhibits a mean of zero. The z component of velocity exhibits a slight positive mean. However, this value is significantly below that of the gamma valley carriers due to the greater effective mass of L valley electrons. Finally, Figure 5.4c shows the energy distribution. Note the large L valley energy distribution at the anode, representing the consequences of electron transfer.

As was indicated in the discussion previously, in which we are solving a one dimensional problem within a two dimensional grid, the instantaneous *statistical* distribution of electrons and, hence, potential within the device displays an apparent two dimensional structure. This is due to the limited number of particles used in the simulation, and as the number of particles increases, the deviation from the one-dimensional norm should asymptotically reach zero. To show this two-dimensional effect the *net* charge distribution along lines of constant x, running from cathode to anode, at x values of 0.02, .06, .10, .14, and .18 μm are presented in Figure 5.5.

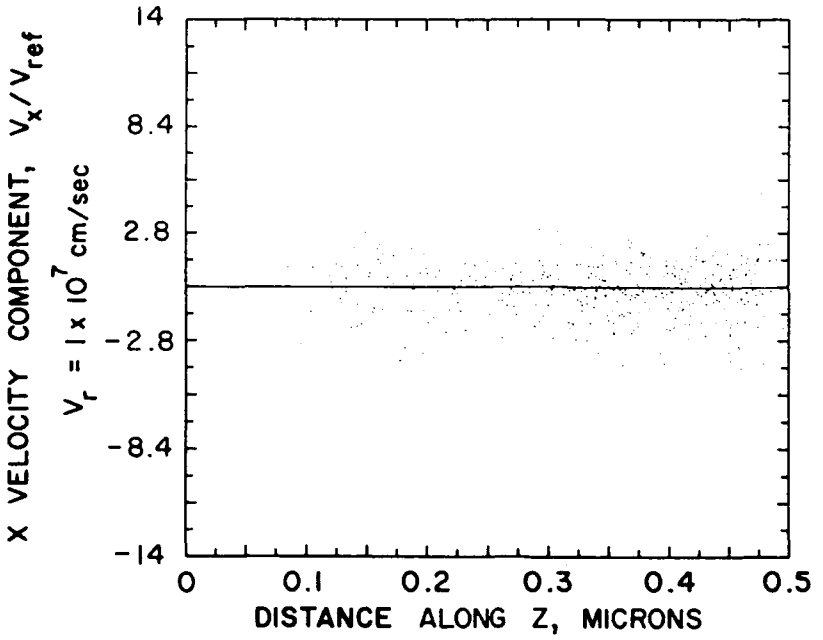

Figure 5.4a Projection of the distribution of L velocity in the 'x' direction for a bias of 1.0v.

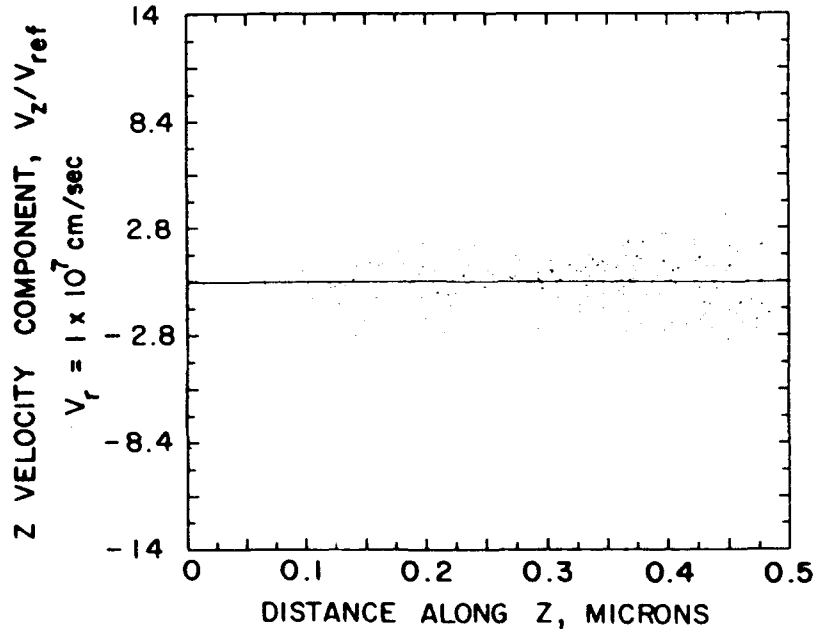

Figure 5.4b Projection of the distribution of L velocity in the 'z' direction for a bias of 1.0v.

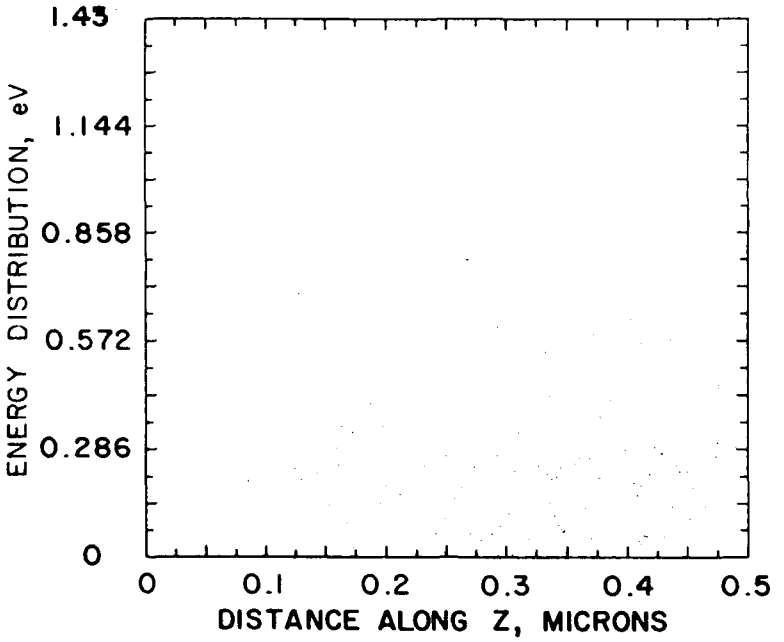

Figure 5.4c Projection of the distribution of L energy in the 'z' direction for a bias of 1.0v.

The net charge distribution at point (z) is $-e(n-N_D)$, and if the density were constant and equal to background the net charge distribution would be centered about zero. For the one dimensional diode problem, the initial condition of net charge neutrality was imposed. For this solution, which yields a nonuniform potential distribution that increases from cathode to anode, there is a subsequent accumulation of carriers in the vicinity of the anode and a depletion of carriers in the vicinity of the cathode.

As seen in figure 5.5 the net charge distributions are negative in the vicinity of the cathode (indicating charge depletion) and positive in the vicinity of the anode (indicating charge accumulation). The charge distributions in figure 5.5 are obtained from a cloud-in-cell smoothing of the particles for use in Poisson's equation. The particular results shown are for a 1 volt bias across the device. As can be seen, there is considerable scatter in the results, but all plots show some degree of depletion at the cathode and accumulation at the anode. We note that at the cathode, electrons are injected to maintain charge neutrality.

The potential variation along the same planes in the device are shown in Figure 5.6. The variation across the device, while still apparent, is less obvious due to the smoothing nature of solutions to Poisson's equation. The curvature of the resulting distribution of potential reflects the depletion and accumulation of carriers within the structure. As is apparent, the solution is not a uniform field solution.

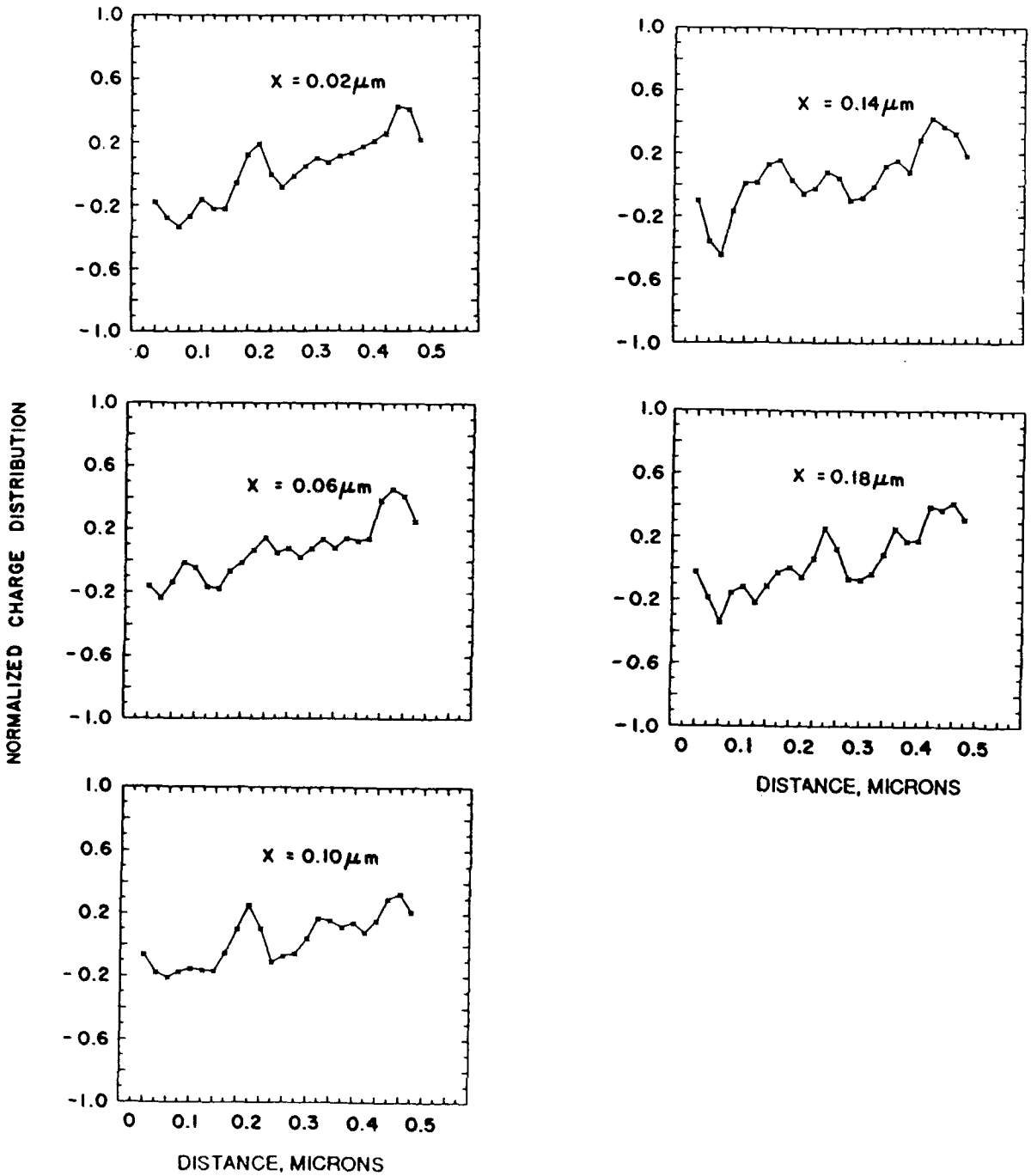

Figure 5.5 Normalized net charge distribution along the z direction at five different values of x : 0.02, 0.06, 0.10, 0.14, 0.18 microns.

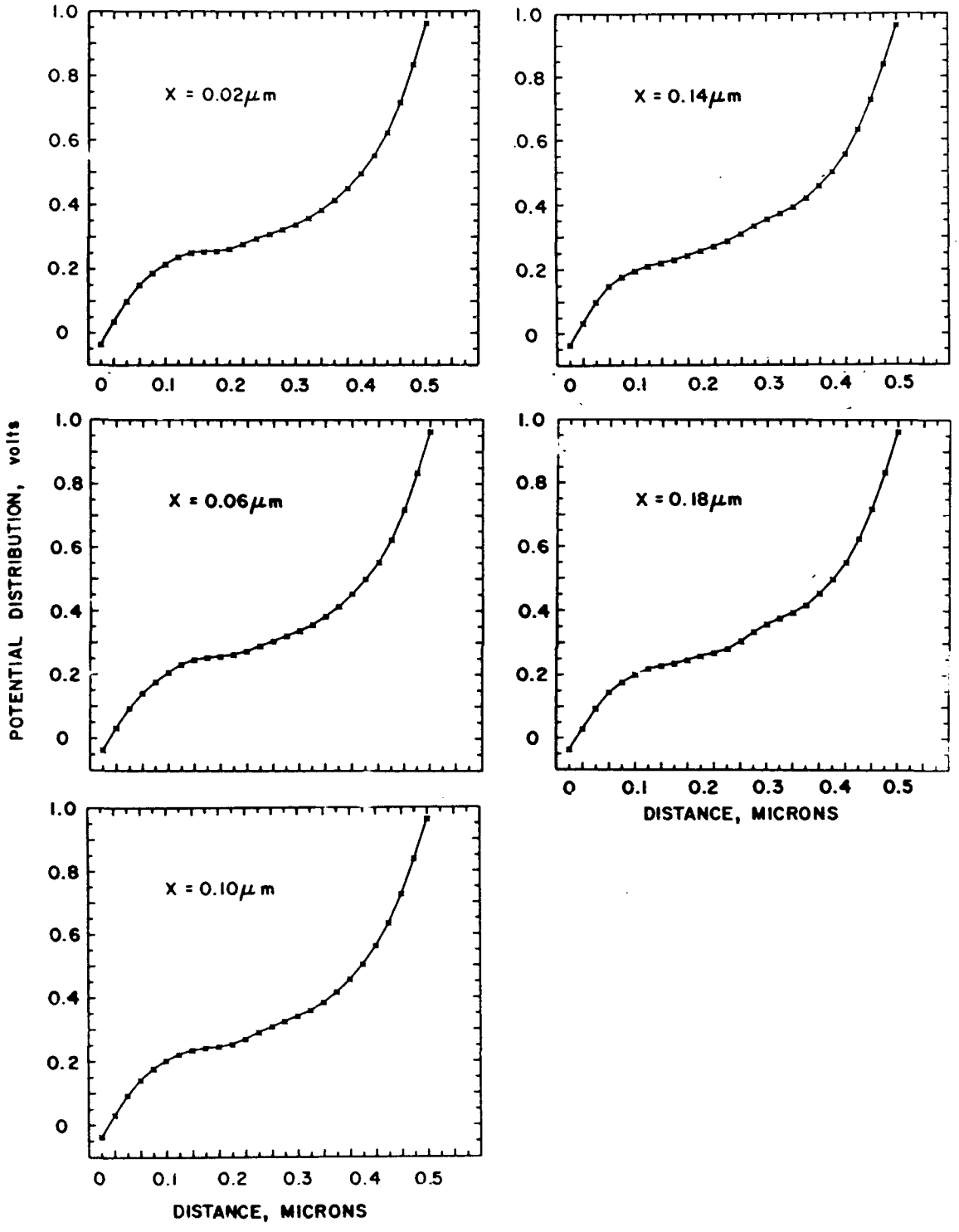

Figure 5.6 Potential distribution along the z direction at five different values of x : 0.02, 0.06, 0.10, 0.14, 0.18 microns.

GaAs FET Simulations

Test Structure, $V_{gs} = 0.1$ v, $V_{ds} = 0.5$ v

The first structure considered, shown in Figure 5.7, was a small modification of the diode structure, and enabled us to develop procedures for studying FETs using MC methods. The device length is 0.6 μm, with a centrally placed 0.2 μm gate. The channel depth was taken as 0.2 μm and uniformly doped to 1 x $10^{17}/cm^3$. This device constitutes a normally-on device. The Schottky gate depletion layer thickness was estimated to be 0.1 μm. A simulation was run for a drain bias, $V_{ds} = 0.5$ volts and a gate bias, $V_{gs} = -0.1$ volts. Four hundred time steps (Poisson updates) were used.

Calculation of Current

For these calculations, which were taken to steady state it was assumed that *no* particle current passed through the gate contact; reflecting boundary conditions at the gate were imposed. The source and drain currents were calculated by determining the numbers of particles passing through the source and drain regions as a function of time, figure 5.8. In steady state the curves are linear with the slope (drawn in each of these figures) of these curves yielding the current at the contacts. Note the nonlinear time dependence of the particle history at the early time stages. For this calculation the gate particle current is zero and the source and drain currents, agree to within numerical accuracy; the source current is 5.41 x 10^2 A/m, the drain current is 5.49 x 10^2 A/m. These currents are approximately a factor of two lower than the current obtained with the simple diode structure discussed earlier; and may be accounted for, in part, due to differences in the background charge density, and under the gate by much higher values of velocity, indicating the prominence of velocity overshoot, as discussed below.

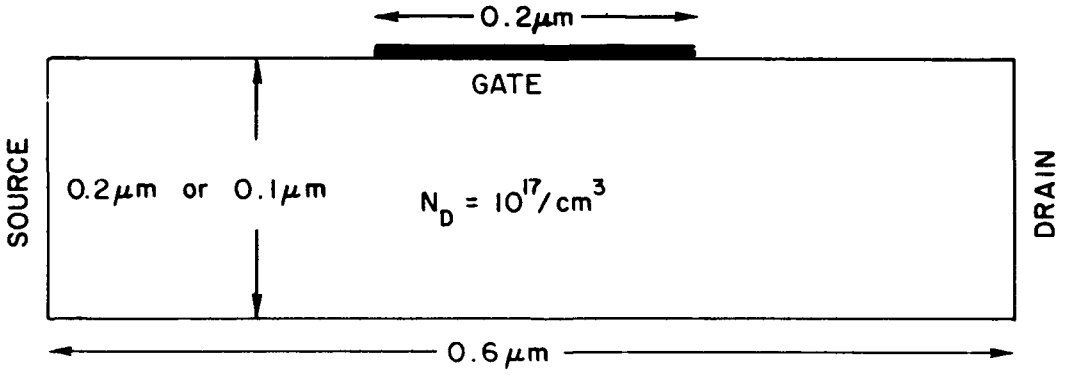

Figure 5.7 Sketch of the GaAs FET structure used in the Monte Carlo studies.

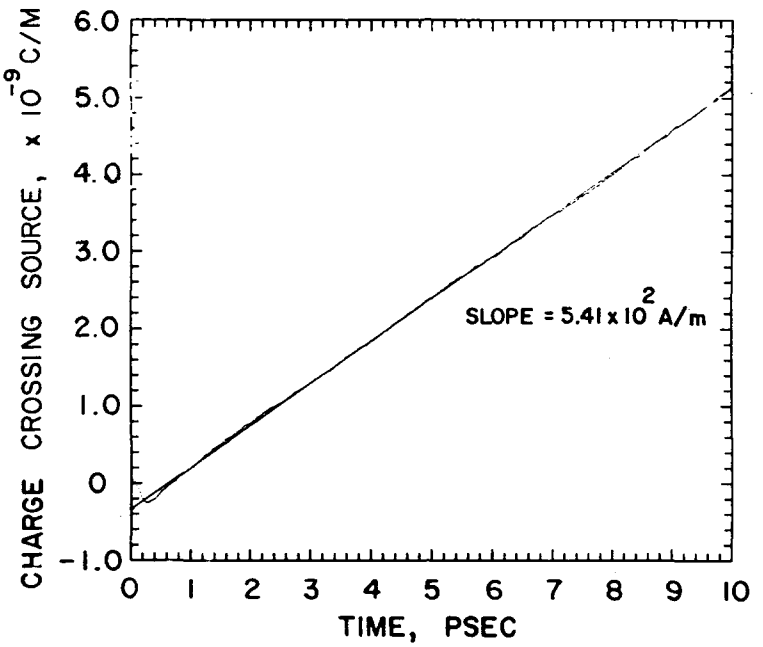

Figure 5.8a Time history of charge across the source contact for V_G= v, V_D=0.5 v

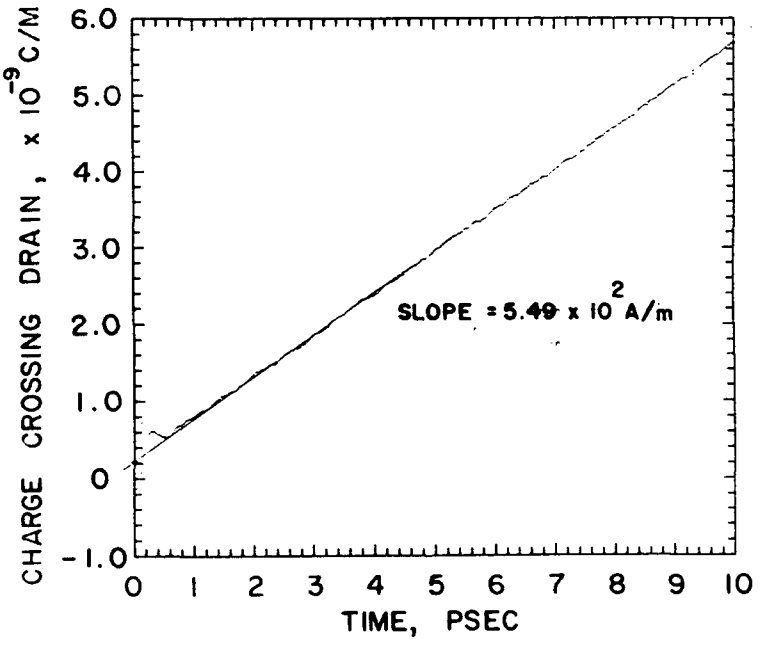

Figure 5.8b Time history of charge across the drain contact for V_G=0.1 v, V_D=0.5 v

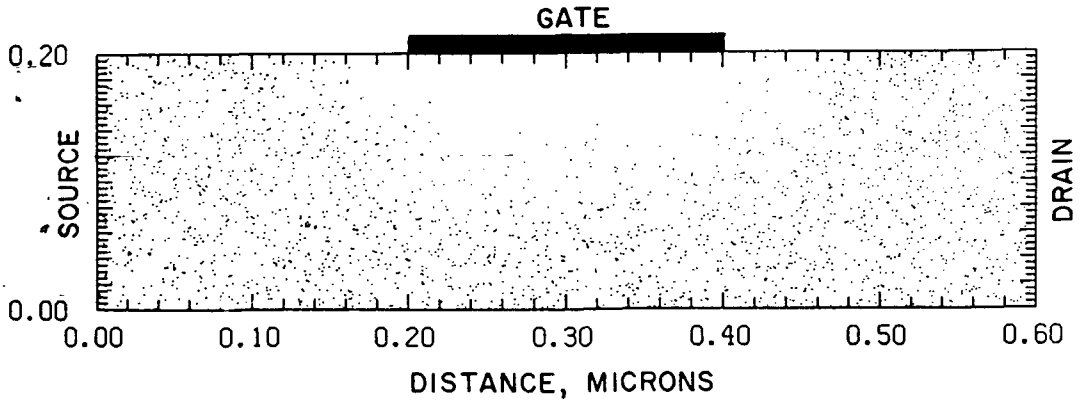

Figure 5.9 Distibution of charge at the termination of the calculation for $V_G=0.1$ v, $V_D=0.5$ v

The distribution of *all* particles in the device at the termination of the calculation is shown in Figure 5.9. Here we observe the expected result of a uniform distribution of electrons under the source and drain with the depletion under the gate clearly evident.

Figure 5.10 shows the *projections* of the distributions of: (a) Γ particle velocity along the z direction parallel to the channel (figure 5.10a); (b) Γ particle velocity along the x direction normal to the channel (figure 5.10b); and (c) Γ energy (figure 5.10c). The results are only apparently similar to the diode calculation, because the current paths through the device suggest that the higher carrier velocities will not be uniformly distributed along the channel. But we note that the calculations show a velocity distribution in the vicinity of the source contact similar to that associated with the diode calculation (figure 5.3b); this is expected as the current density is a factor of two smaller, and the background density is a factor of two smaller than the diode calculation. Under the gate region the velocity distribution displays larger values than the diode calculation, as expected on the basis of current continuity.

Figuure 5.10b displays the expected result that the mean component of the x component of Γ velocity is near zero. The energy variation (figure 5.10c) shows the greatest increase at the drain side of the gate, and while there are still high energy carriers at the drain, there are also a greater number of lower energy carriers there as electrons relax in the lower field at the drain. The results for the L valley electrons are shown in Figure 5.11. As the figures show, by the low number of particles, very few electrons transfer to the L valley and their velocity mean is near zero in both the x and z directions.

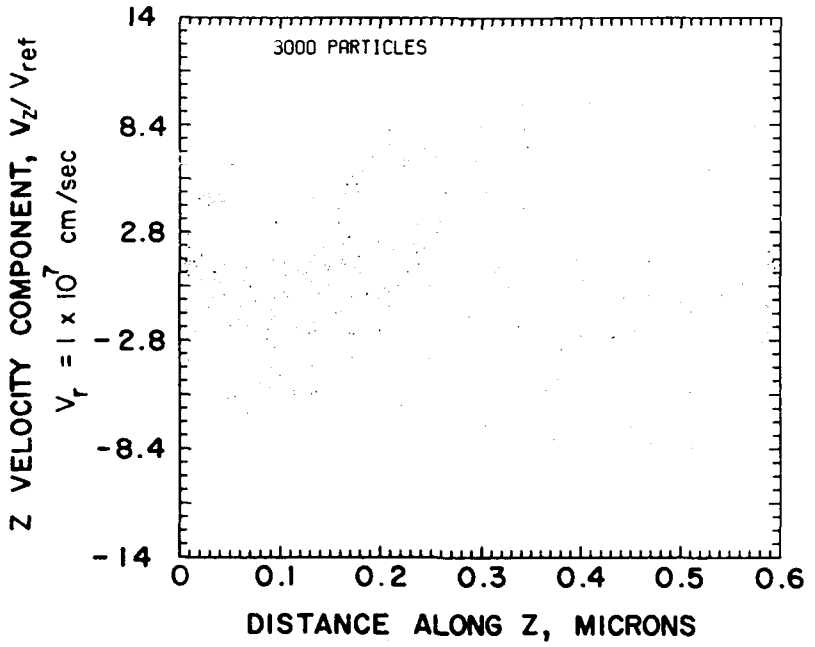

Figure 5.10a Projection of the distribution of Γ velocity in the 'z' direction for V_G=0.1, V_D=0.5v

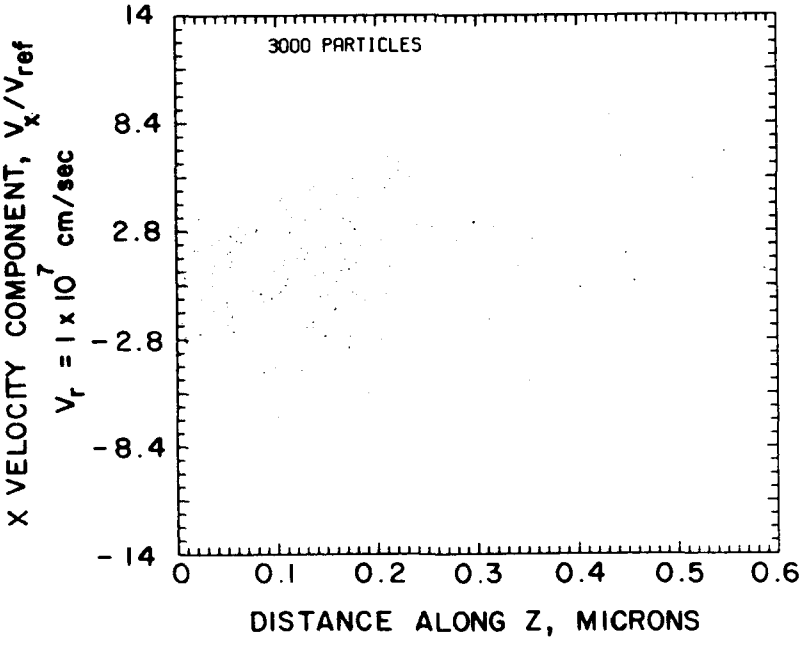

Figure 5.10b Projection of the distribution of Γ velocity in the 'x' direction.

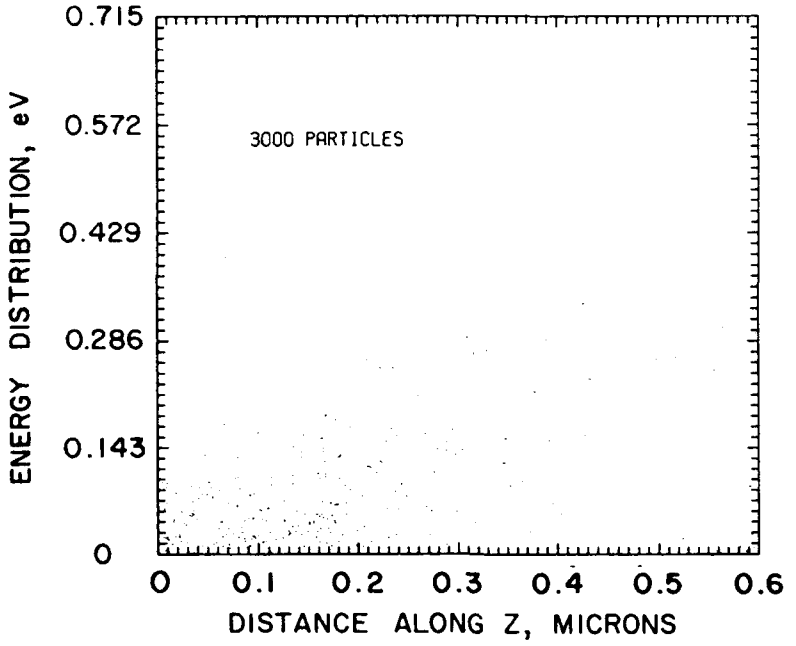

Figure 5.10c Projection of the distribution of Γ energy in the 'z' direction.

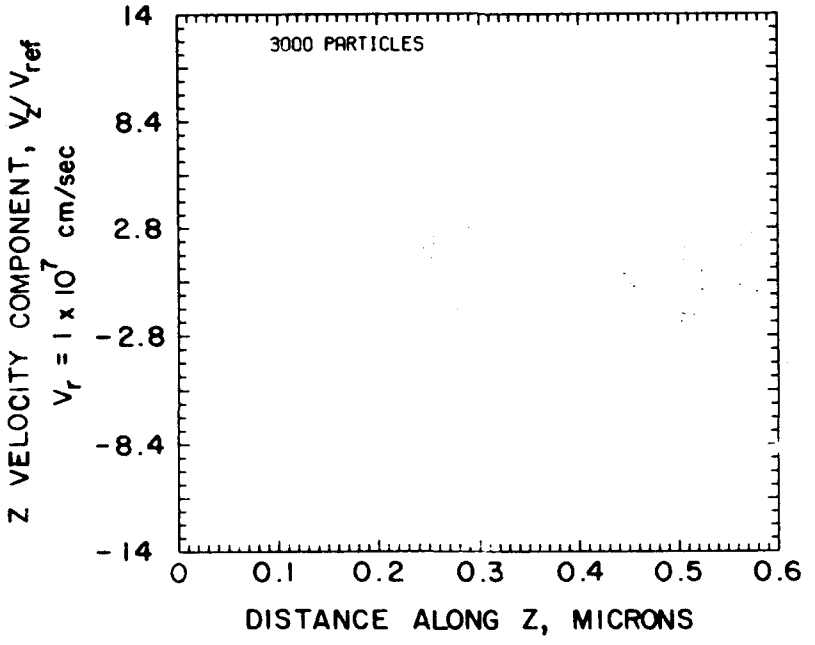

Figure 5.11a Projection of the distribution of L velocity in the 'z' direction.

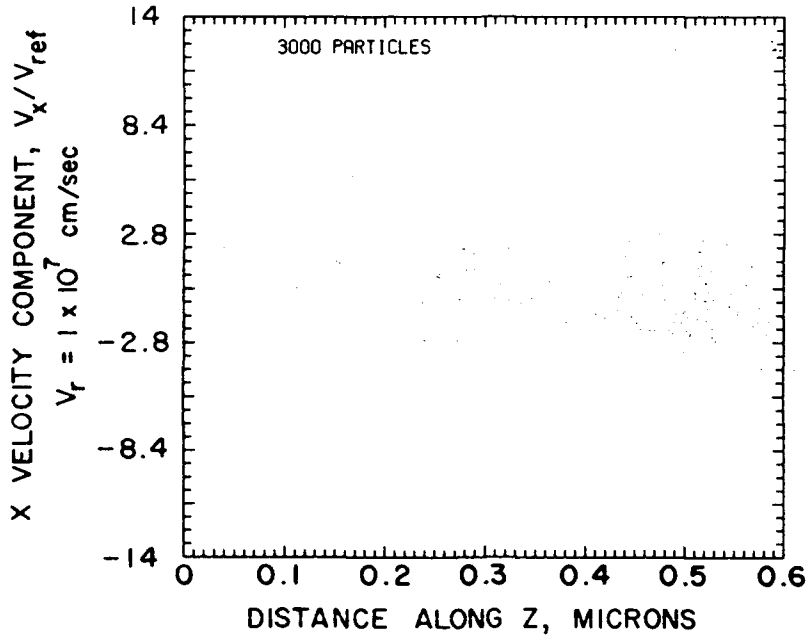

Figure 5.11b Projection of the distribution of L velocity in the 'x' direction.

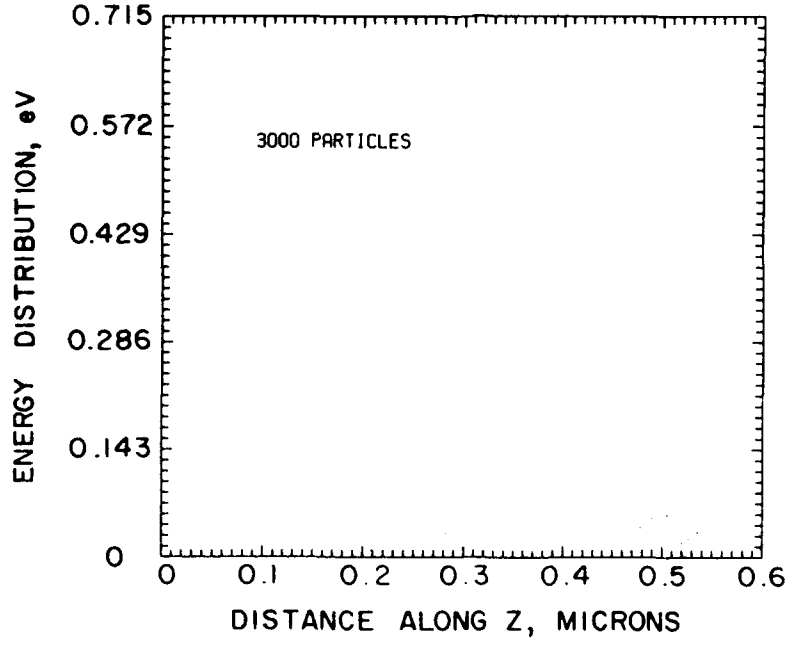

Figure 5.11c Projection of the distribution of L energy in the 'z' direction.

FET Simulations, Monte Carlo and Moment Equation Comparisons

Full MC FET simulations were performed for the structure shown in figure 5.7, but *with the channel width reduced to 0.1 μm.* These calculations were then compared to parallel calculations performed using the moments of the Boltzmann transport equation.

A complete set of current-voltage curves was generated for this device. These characteristics are shown in Figure 5.12. (*An additional set of calculations were performed for a similar device with a 0.1 μm undoped substrate at V_{gs} = 0.3 volts. These calculations yield a current level approximately four times higher over a large bias range that for the basic 0.1 μm channel height structure at V_{gs} = 0.3 v.*) The results for the device without a substrate are in good agreement with those reported for a similar device others. For this device, without the substrate, the drain current at V_{gs} = 0.1 and V_{ds} = 0.5 volts is about 16A/m or about 35 times smaller than the 0.2 μm channel depth device discussed previously; this device is 'normally-off'.

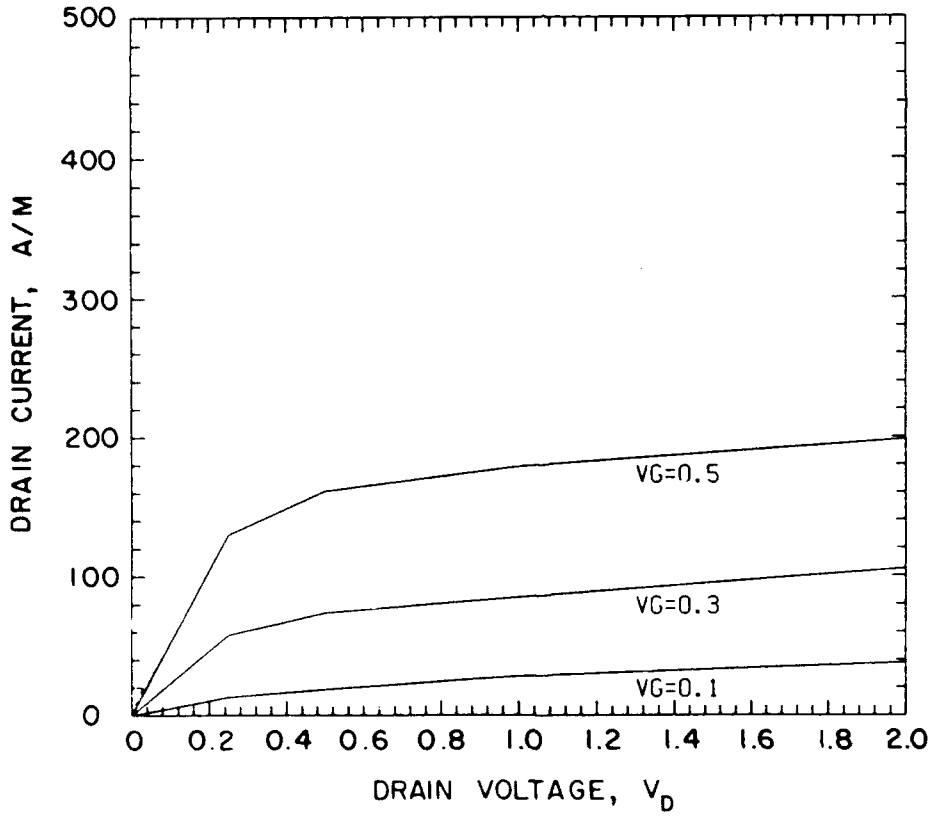

Figure 5.12 Sketch of current versus voltage for the 0.1 micron channel height FET.

Detailed Results for V_{ds} = 0.5 v, V_{gs} = 0.1 v.

The time history of the charge crossing the source and drain contacts for V_{gs} = 0.1, V_{ds} = 0.5 is shown in Figure 5.13. While the scales for the source and drain charge are different, the calculations indicate that it takes a longer time for the source contact to reach steady state. At the end of 10 psec, the calculation was terminated with the resulting slopes at the source and drain yielding current levels at the source of 15.4 A/m, and at the drain of 18.5 A/m.

The total electron distribution in the device at V_{ds} = 0.5 v and V_{gs} = 0.1 v is shown in Figure 5.14. Here we observe the complete depletion of carriers under the gate, pinching off the channel and an *extension* of the depletion region downstream of the gate towards the drain.

Figure 5.15 shows the *projection* of the distribution of the velocity components and energy for the gamma valley carriers at this bias. Both the z component of velocity parallel to the channel (figure 5.15a), and the x component of velocity normal to the channel (figure 5.15b), are very small. From the current it was determined that the mean velocity of carriers crossing the source and drain contacts is of the order of 10^6 cm/sec. We note that the few gamma valley carriers under the gate have a much higher velocity ranging from 3 x 10^7 to 6 x 10^7 cm/sec. Recall that these projection plots are *instantaneous* distributions at the end of the computation and do not reflect the variation which may be expected from time increment to time increment. Due to the low velocity at the source and drain and low current, the gamma valley carrier energy levels are very low, as shown in Figure 5.15c. The results for the L valley carriers are not shown for this case, since very few carriers transfer from the gamma valley.

Detailed Results for V_{ds} = 0.5 v, V_{gs} = 0.5 v.

When the gate bias level is increased to V_{gs} = 0.5 volts, while holding V_{ds} at 0.5 volts, the electron distribution is as shown in Figure 5.16. There are significantly more particles in the channel under the gate at this bias level, indicating the reduction in the depletion layer thickness. The current level is a higher 160A/m.

Figure 5.17 displays the projections of the z component of gamma velocity (figure 5.17a), the x component of gamma velocity (figure 5.17b), and the gamma energy (figure 5.17c). When compared to Figure 5.15, we observe substantially more high velocity carriers throughout the structure, and a correspondingly broader distribution of higher energy carriers in figure 5.17. There are also many more carriers in the device. This occurs because of the greater depletion in the V_{gs} = 0.1 volt case.

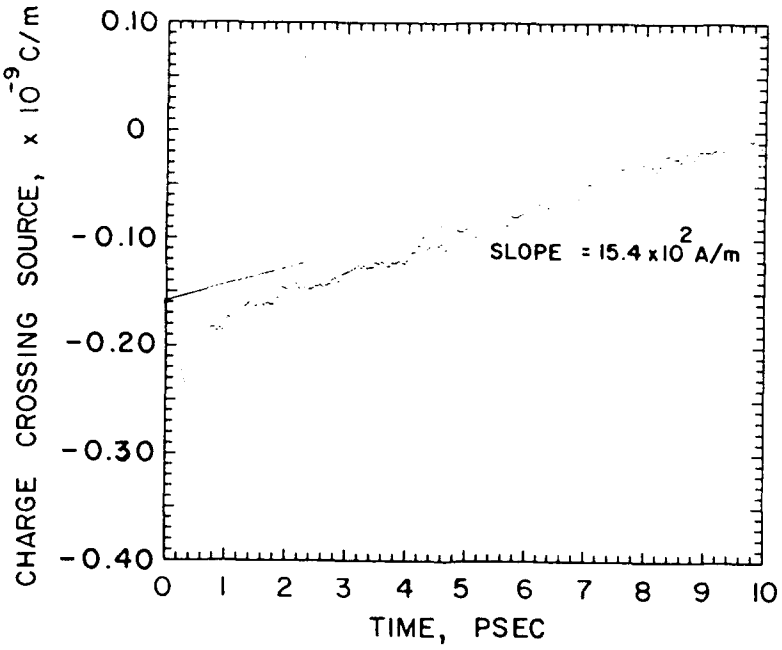

Figure 5.13a Time history of charge across the source contact for $V_G=0.1$ v, $V_D=0.5$ v.

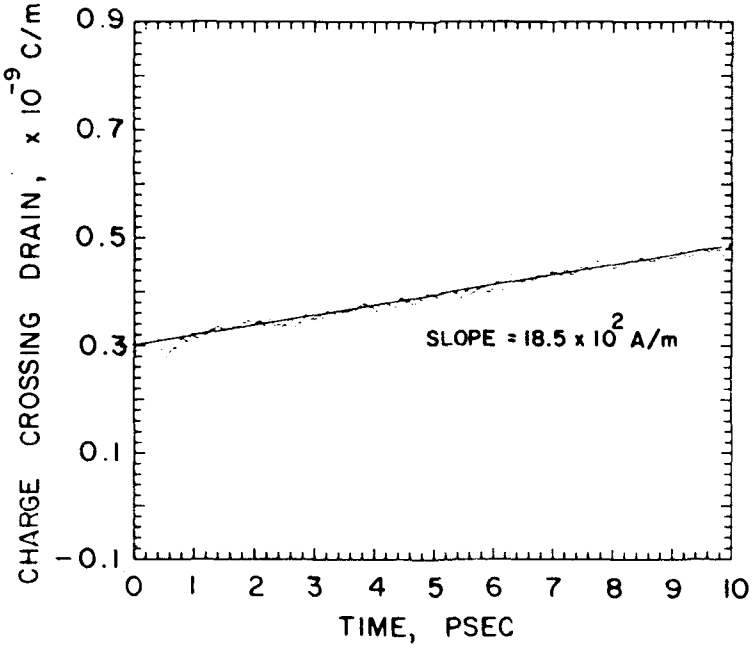

Figure 5.13b Time history of charge across the drain contact for $V_G=0.1$ v, $V_D=0.5$ v.

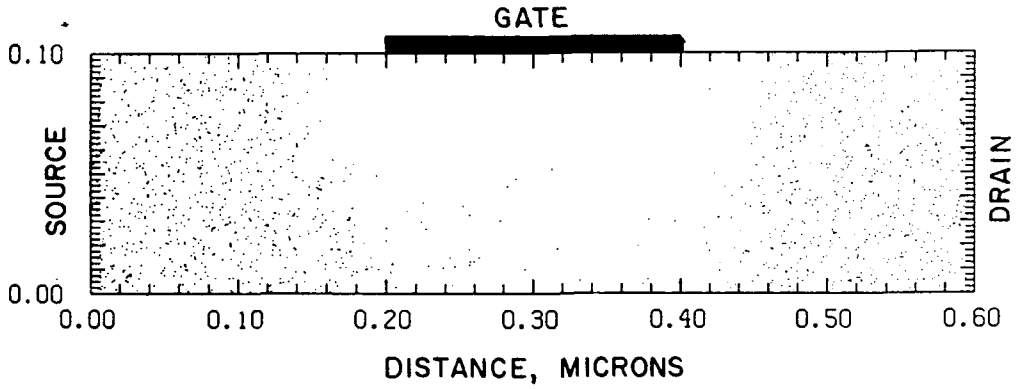

Figure 5.14 Distibution of charge at the termination of the calculation for V_G=0.1 v, V_D=0.5 v

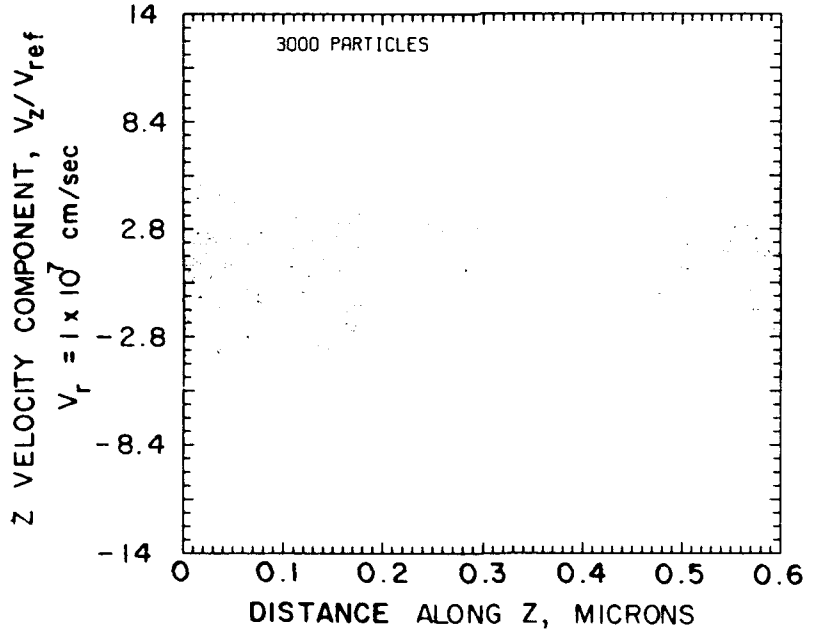

Figure 5.15a Projection of the distribution of Γ velocity in the 'z' direction for V_G=0.1, V_D=0.5v

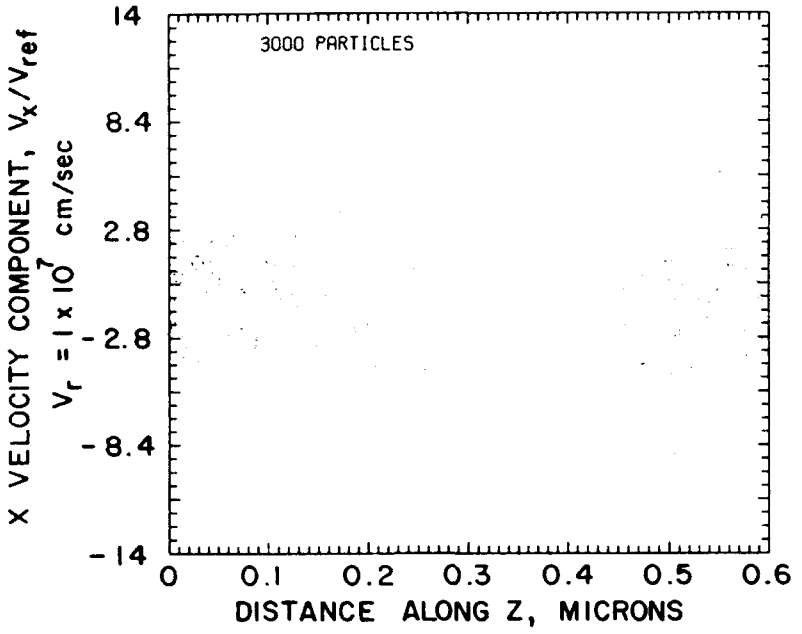

Figure 5.15b Projection of the distribution of Γ velocity in the 'x' direction.

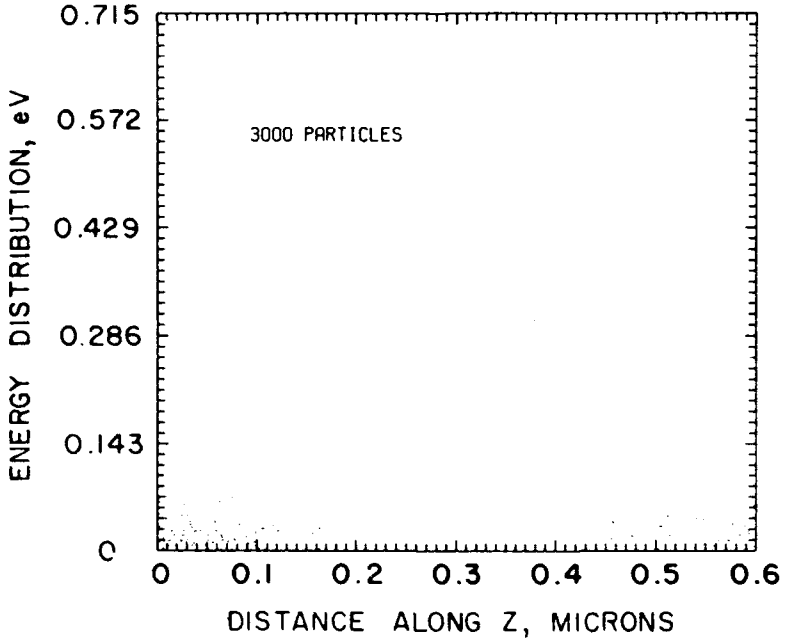

Figure 5.15c Projection of the distribution of Γ energy in the 'z' direction.

Several additional generic comments are in order: (i) In the MC simulation, 3,000 particles represent a charge neutral situation. As the depletion layer evolves, the total number of particles in the device drops below 3000 to a number dependent on the gate bias and depletion layer structure. (ii) Comparing figures 5.15b and 5.17b we recall that the mean z velocity component at the source and drain in Figure 5.15b, where the current level was 16A/m, was 10^6 cm/sec. In Figure 5.17b, where the current level is 160A/m, the mean velocity at the source and drain is 10^7 cm/sec. This result is difficult to obtain from the velocity projections. It is however apparent that very high particle velocities, approaching 9 x 10^7 cm/sec and above, are present in the channel. (iii) The energy distribution, shown in Figure 5.17c, shows energy levels in excess of 0.3 eV, and electron transfer would be expected.

The L valley carrier velocity and energy distributions are shown in Figures 5.18a-c. The figures indicate transfer occurs at the drain end of the device, somewhat past the end of the gate. The carrier velocities remain low, as does the L valley energy, due to the higher effective mass. The point to note is that while the numbers of particles transferred to the L valley is substantial, *current* is still dominatedy the fewer gamma valley carriers with their higher velocities.

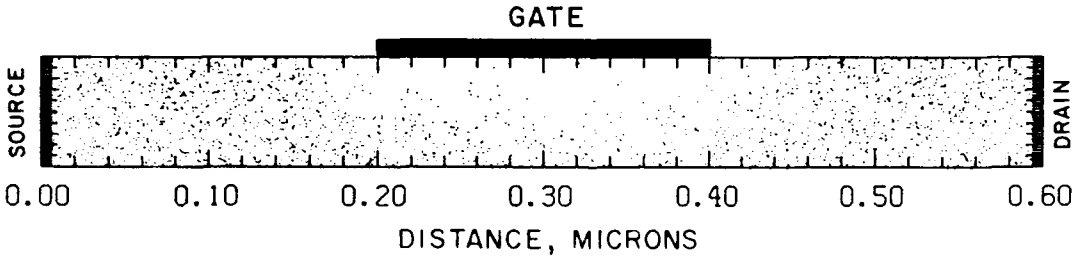

Figure 5.16 Distribution of charge at the termination of the calculation for $V_G=0.5$ v, $V_D=0.5$ v

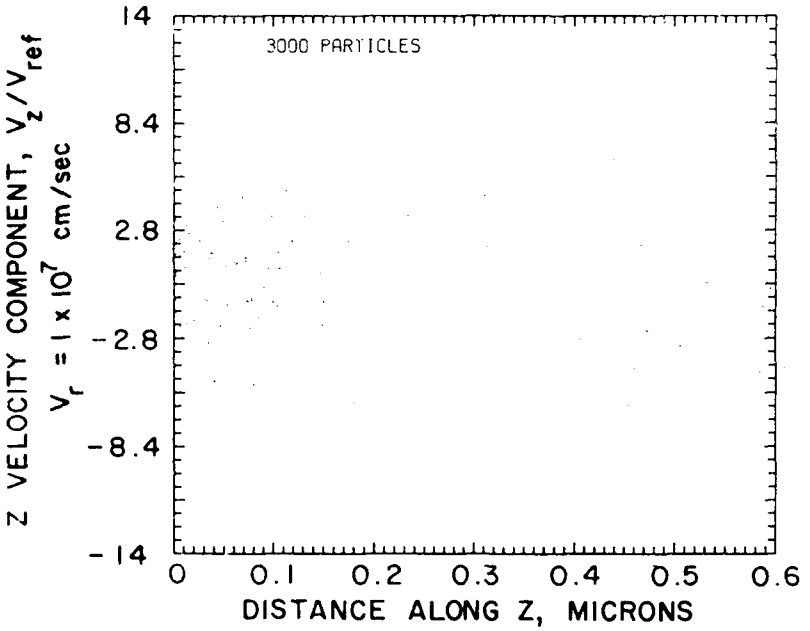

Figure 5.17a Projection of the distribution of Γ velocity in the 'z' direction for $V_G=0.5$, $V_D=0.5v$

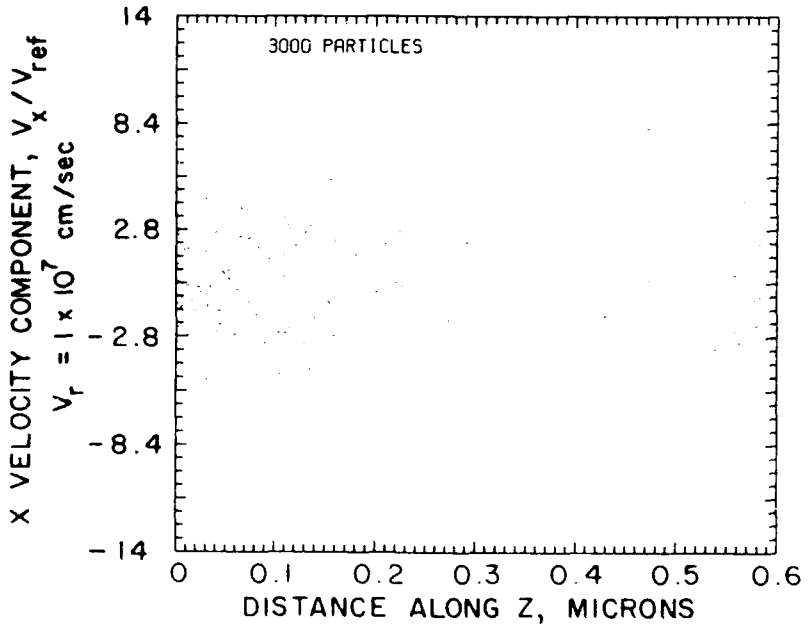

Figure 5.17b Projection of the distribution of Γ velocity in the 'x' direction.

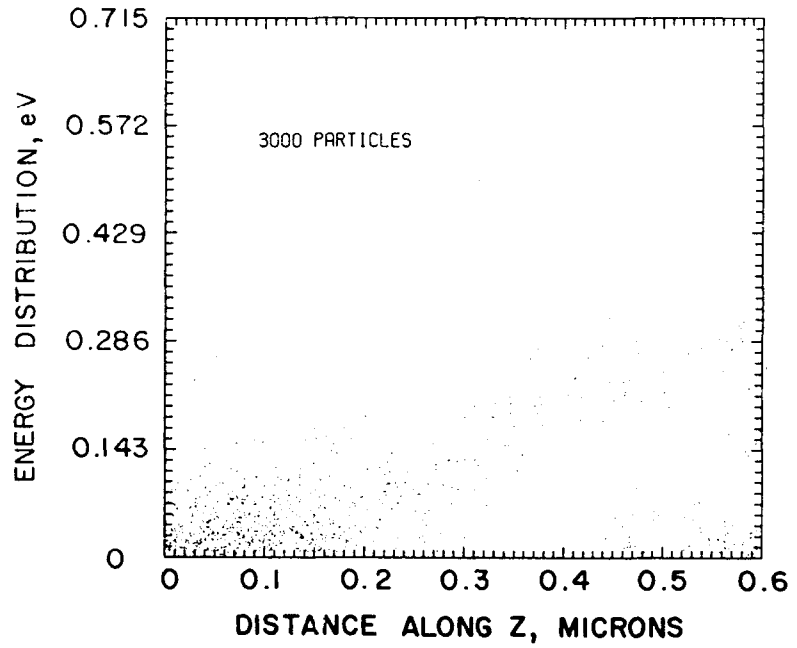

Figure 5.17c Projection of the distribution of Γ energy in the 'z' direction.

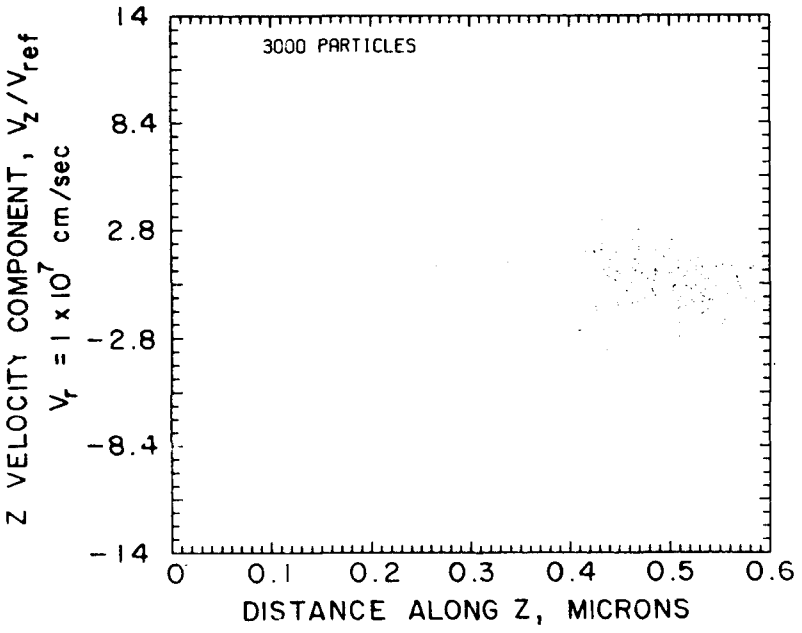

Figure 5.18a Projection of the distribution of L velocity in the 'z' direction for $V_G=0.5$, $V_D=0.5v$.

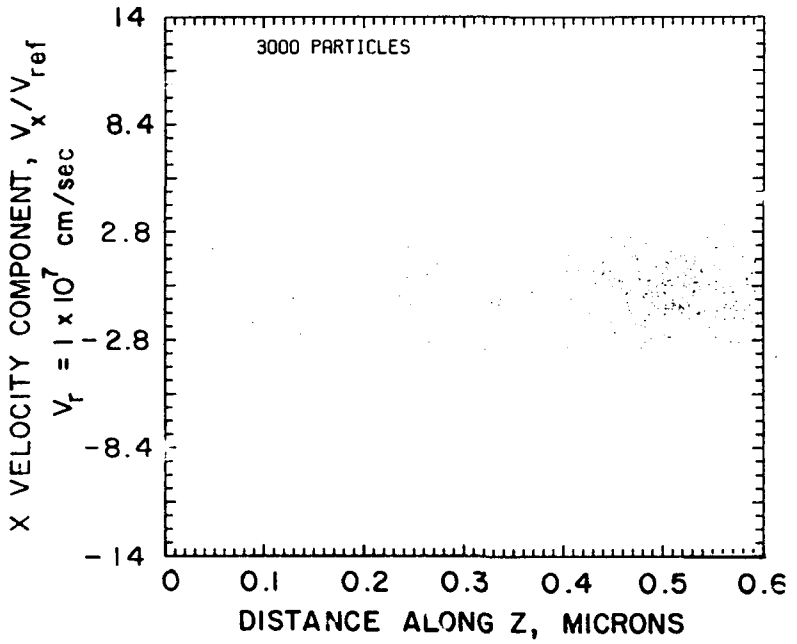

Figure 5.18b Projection of the distribution of L velocity in the 'x' direction.

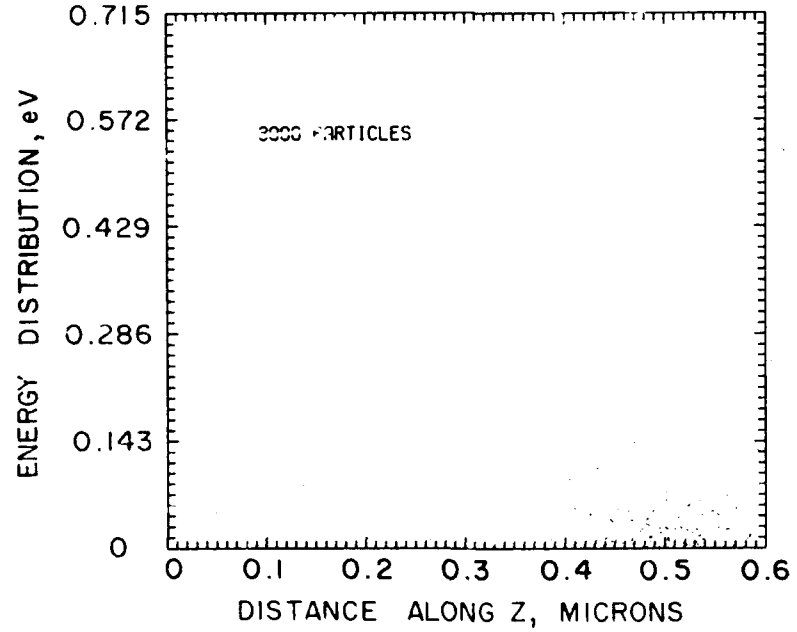

Figure 5.18c Projection of the distribution of L energy in the 'z' direction.

Comparison to MBTE Calculations

The MC calculations were compared to calculations using the moments of the Boltzmann transport equation algorithm. This was the algorithm implemented for the study of the pseudomorphic HEMT. For this comparison a complete set of current voltage characteristics was obtained. As discussed in the earlier chapters the calculations performed with the moment equations involve the incorporation of scattering integrals whose value depends upon assume scattering constants such as the acoustic deformation coupling constant, the Frohlich field, etc. Very often in performing these calculations the values chosen for the parameters are adjusted until a uniform field dependent velocity is computed and compared to a similar calculation using MC procedures. Adjustments in the MBTE field dependent velocity parameters are then made until agreement with the MC results is obtained.

Two comparative calculations were performed here. In the MBTE calculation only two velleys were considered. In one case the Γ-L separtion was 0.33 ev, which was greater than the 0.30 value used in the MC study. In the second, the Γ-L separation was 0.284 ev. Additionally, in the larger energy separation calculation the static dielectric constant was taken as 12.53. In the lower intervalley calculation the static dielectric constant was set to 13.81. In all three calculations the current voltage characteristics for $V_{gs} = 0.1$ v, were similar as shown below.

Before discussing the current voltage characteristics it is useful to compare the detailed results for the MC and MBTE calculations at a specific bias point: $V_{ds} = 1.0$ v, $V_{gs} = 0.3$ v. For example figure 5.19 is a comparison of the density distribution obtained from both the MC and the MBTE calculations. The top frame displays contours of constant charge density. The half-ellipses represent the shape of the depletion region. It appears to be qualitatively similar to the shape of the depletion region obtained from the MC calculation.

Figure 5.20 is a projection of the potential surface for this calculation at $V_{ds} = 1.0$ v and $V_{gs} = 0.3$ v. Note that for the MBTE calculation and on the channel side, the potential increases monotonically from the source to a value one volt higher at the drain contact. The dip in potential on the gate side represents the effect of the gate boundary condition. For the MC calculations, apart from some irregularities in the surface, due to the statistical nature of the MC particle distribution, the potential surfaces are very similar.

The predicted current-voltage characteristics for this structure as obtained from the MC and MBTE are compared in figures 5.21 and 5.22. In figure 5.21, the larger intervalley energy separation was assumed, in figure 5.22, the smaller value was used. The curves labeled "A" were obtained for a finite but small value of the thermal conductivity (see

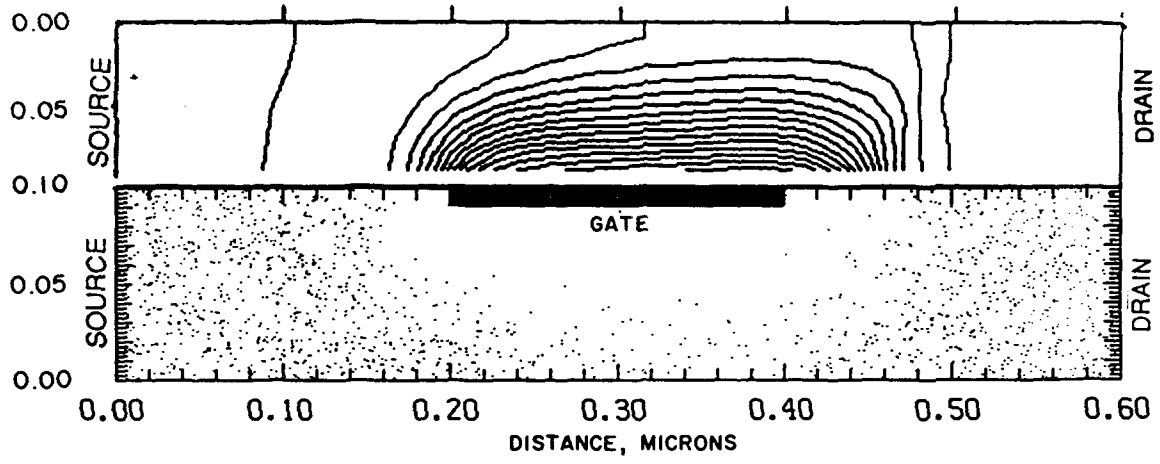

Figure 5.19 Comparison of Monte Carlo particle Distribution (lower) with MBTE density Contours (upper) for V_G=0.3v, V_D=1.0 v. Γ-L separation = 0.33 ev.

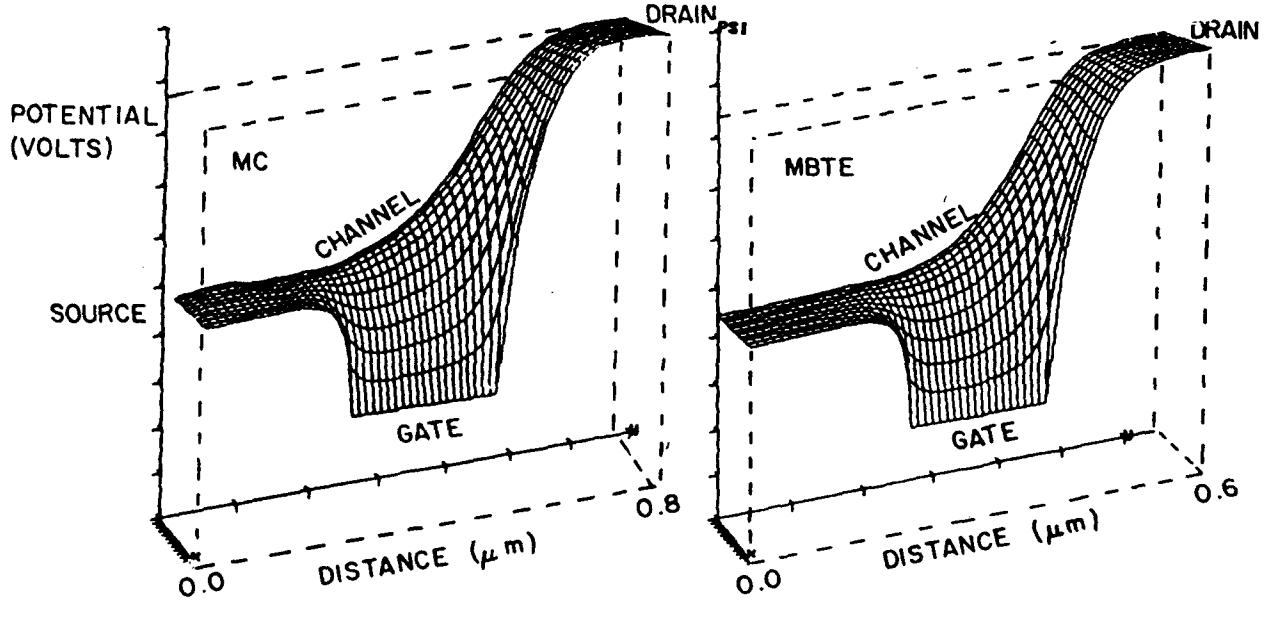

Figure 5.20 Potential surface from MC and MBTE calculations for V_G=0.3v, V_D=1.0 v

section 2) As a result, the heating of the Γ valley carriers is a maximum and remains highly localized due to minimal heat conduction. This gives the highest level of intervalley transfer and results in the observed negative conductance at higher gate voltages, which is in disagreement with the MC result. The cause of the discrepancy lies in either the value of the thermal conductivity chosen, or the scattering rates, or both. That is, the predicted Γ valley temperature is too high, or at the predicted temperatures the intervalley scattering is too large. We emphasize that under uniform field conditions both the MC and the MBTE approaches yield similar field dependent velocity curves. Thus the result is further complicated by non-uniform field effects. If the problem lies with the predicted levels of the Γ valley temperature, then the thermal conductivity and the momentum and energy relaxation times may be suspect. Assuming the problem is limited to thermal conductivity, a limit may be explored by setting the thermal conductivity to infinity. Under such conditions the *electron temperature will remain constant everywhere within the structure at the lattice temperature* (electrons enter the device at equilibrium with the lattice and the electron temperature reflects this.) Such a condition results in the current voltage characteristics shown as "B" in figure 5.21. From this result we observe that the manipulation of the thermal conductivity brackets the MC result and the numerical results could be matched if desired. However, this approach is not satisfactory.

A second investigation was performed using the initial finite value of thermal conductivity but with the smaller value of Γ-L separation. The field dependent velocity is nearly the same for both. The MBTE calculation performed using scattering rates based on these parameters yield the current voltage characteristics presented in figure 5.22. Here we see excellent agreement between the MC and MBTE results.

Without editorializing about *better or worse* agreement between different sets of numerical procedures and different sets of calculations, the results tend to isolate differences in the physical assumptions and consequences of the two approaches. We note that in the MC calculation carriers with an energy sufficient for intervalley transfer undergo such transfer. In the MBTE where we are dealing with mean energies, at every value of energy there are always carriers in the upper valley. Thus the transition is not sudden. If the Γ-L separation is larger than that used for the MC, then there is a delay in the field value at which intervalley transfer occurs. This delay in field value does not imply that negative conductance in the IV characteristics will necessarily occur, for the rate of intervalley transfer is controlled by a number of parameters including the coupling constants. The best that can be said in comparing the MC and MBTE calculations is that: (a) they both provide qualitatively similar physics, and (b) adjustments of parameters can lead to close quantitative numerical agreement. The choice of using either MC or MBTE then rests with other issues, such as ease of the computational procedure, etc.!

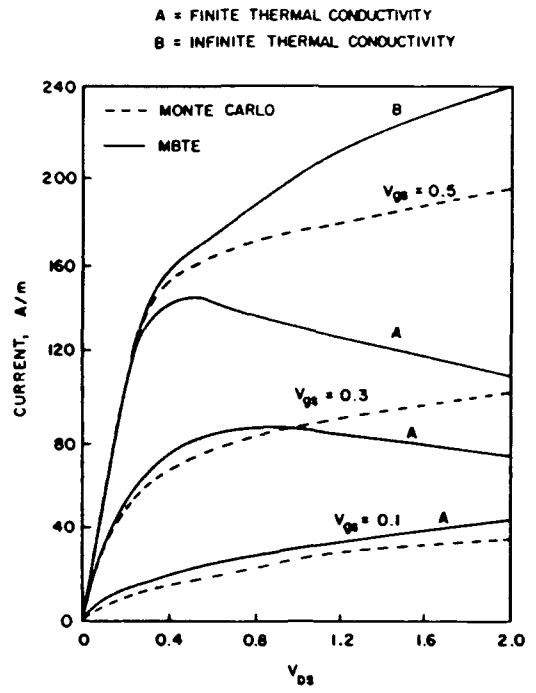

Figure 5.21 Comparison of I-V Characteristics as determined from the Monte Carlo, and MBTE solutions with Δ_{Γ}-L = 0.36 ev.

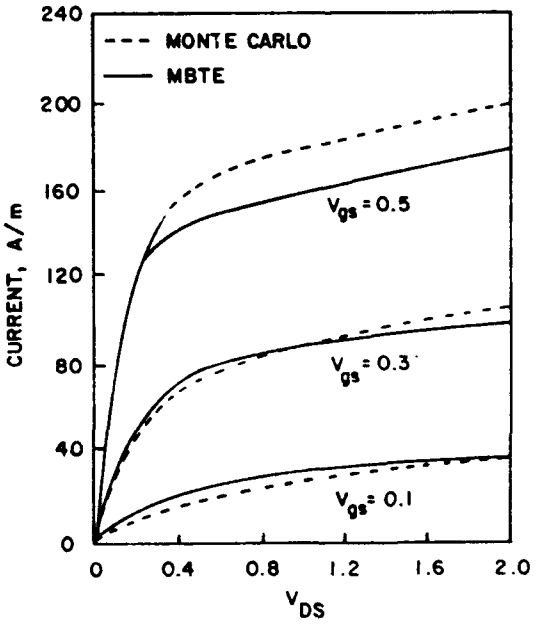

Figure 5.22 Comparison of I-V Characteristics as determined from the Monte Carlo, and MBTE solutions with Δ_{Γ}-L = 0.284 ev.

6. One Dimensional Transient Simulations: Search for Overshoot

The search for velocity overshoot has occupied the attention of many workers over the last decade. The difficulty lies in measuring velocity overshoot, since it is always present. Furthermore all electrical measurements involve the time dependent passage of charge, which in turn is sensitively affected by local strong and weak nonuniformities in the distribution of carriers. Additionally, as the time scales are reduced, a large number of calculations, including those discussed in section 4, indicate that the transients associated with displacement currents occur on time scales commonly associated with velocity overshoot transients. Nonetheless, both transient and steady state experiments have been deviced to identify velocity overshoot. For example: (i) In the early 70's it was demonstrated that the transient operation of GaAs would exhibit microwave heating and electrical behavior that would be directly attributable to velocity overshoot, while (ii) Laval et al (1980) attempted to show that the current voltage curves would show an increase in current saturation as the active region of the structure was decreased and that this increase in current saturation could be attributed to velocity overshoot. None of these approaches is regarded by the present authors as representative of velocity overshoot. Rather we should not be looking at velocity overshoot but at the more general problem of nonequilibrium, since during the course of a transient there are essentially four time scales to deal with: *(i) carrier relaxation, (ii) momentum relaxation, (iii) energy relaxation, and (iv) displacement current (capacitive),* time scales.

The simplest type of experiment to exhibit velocity overshoot is a two terminal experiment that isolates the different time scales associated with energy, momentum and capacitive contributions. In section 4, involving the transient behavior of the pseudomorphic HEMT, it was determined that the time to relaxation was determined by the longest time scale, which was the relaxation of the electron temperature. The two terminal transient simulations discussed below are intended to highlight the differences between the temperature, momentum and capacitive time scales-and to identify the differences as representative of nonequilibrium phenomena.

As discussed by the present workers, the issue of velocity overshoot is nonlinear in the sense that at low values of bias there is very little electron transfer, at very high values of bias there is a great deal of electron transfer. If the signals imposed on a device do not result in the transfer of carriers from the lower to upper valleys or from the upper to lower valleys, then any nonequilibrium contributions arise from differences between energy and momentum relaxation time without the competing effects of intervalley transfer. At intermediate values of bias intervalley transfer occurs and complicates the issue. To determine the means of resolving some of these competing effects we consider the following numerical experiments. The transient calculations are obtained from a solution to the moments of the Boltzmann transport equation for the structure of figure 6.1.

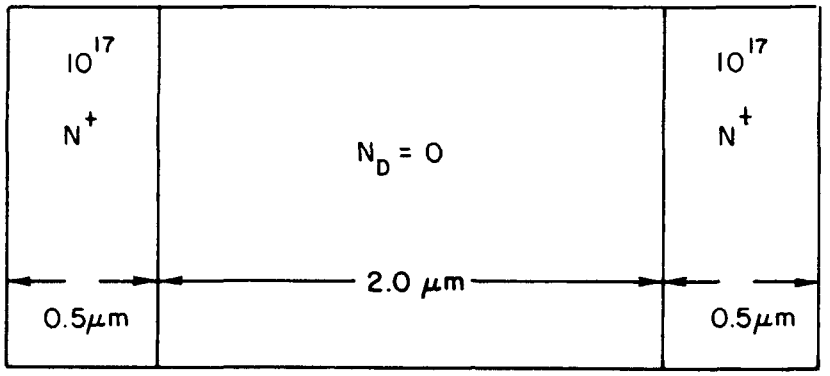

Figure 6.1 Structure used in the transient simulations.

We consider the NIN structure identified in figure 6.1. The end regions are doped to $10^{17}/cm^3$ with the interior 2.0 micron region being undoped. The structure is subject to a DC bias of 2.0 v, and reaches steady state with a current level of $4.2A/cm^2$.

Superimposed upon the DC result is a time dependent AC voltage. The time dependent voltage is periodic exhibiting, repetitive excitation and relaxation. The excitation portion generally results in an increase in current beyond the dc value. The relaxation phase results in a decrease in current toward the steady state value. As a baseline calculation consider figure 6.2.

Figure 6.2a displays the applied voltage, and the resulting total current response for the diode. The voltage train consists of a step change in voltage from a DC value of 2.0 v, to 4.0 v, followed by an exponential decay to 2.0 v. The period of the oscillation is 5 ps and is of the order of the relaxation time for the electron temperature as discussed in section 5. The numbers listed in the voltage pulse of figure 6.2a are keyed to the spatial dependent distributions in the remaining parts of figure 6.2. We point out that these calculations were for the first ten picoseconds of the transient. In steady state all of the variables computed will reach steady state with the period of five picoseconds. As will be apparent from the discussion, not all variables reach steady state during the first ten picoseconds. The consequences of this will be discussed.

The current oscillation displayed in figure 6.2a shows characteristics of the displacement current contributions identified in section 4. Anticipating later results (see figure 6.5) the high frequency oscillations are dependent upon the doping level of the N^+ regions and decay more rapidly with increasing doping density. Recall that the dielectric relaxation time decreases with increased doping level. A comparison of the two figures indicates the more rapid oscillation and decay for the higher doping density calculation. Note also that the steady state current for both cycles of the figure 6.2a calculations are the same. *For this transient there is little that can be extracted concerning nonequilibrium effects.* Nevertheless the details of this calculation are worthwhile considering.

Figure 6.2b is a plot of the self consistent voltage within the structure during one cycle of the oscillation. The numbers in each frame correspond to the numbers on the oscillatory profile of figure 6.2a. The general feature of the potential profile is that there is a slight retarding potential in the vicinity of the cathode N^+I interface with a monotonic increase in potential toward the anode boundary where the potentials is flat at the anode N^+ region. The distribution of charge accompanying this potential change is shown in figure 6.2c, with breakdown between the Γ and L valley contributions represented by their magnitudes. For this oscillation most of the carriers are in the Γ valley, with most of the transfer occuring for this range of bias near the downstream N^+ region. Nonequilibrium electron transfer occurs near the downstream interface. The gamma valley carrier velocity corresponding to the voltage changes is displayed in figure 6.2d. Within the undoped region the carriers are reaching speeds near $4x10^7$ cm/sec, (without any apparent way to detect them, since an independent means of ascertaining the exact density distribution is not possible.) The velocity distribution shows complete relaxation during the latter half of the cycle, a feature consistent with the short momentum relaxation time. The gamma valley electron temperature, shown in figure 6.2e requires a little more time to relax, but for all practical purposes the structure has relaxed to its steady state value within the time frame of five picoseconds.

The calculations of figure 6.2 are such that the structure spends little time in the high voltage range. There is a sudden increase in voltage followed by an exponential drop to a steady state. Thus the detailed transient behavior or transfer from the lower to the upper valleys and then return is not exposed. To expose this detail the applied voltage must permit some fraction of the electrons to undergo transfer to and from a specific value. *We point out that when dealing with the steady state equilibrium velocity field curves of Phase I the issue of the transient transfer, which is at the core of velocity overshoot, did not enter the discussion.* Figure 6.3 displays results in which the voltage is exponentially increased from two volts to near four volts and exponentially decreased to two volts. The period of oscillation is again five picoseconds. The keying on the voltage profiles has the same significance as the keying of figure 6.2.

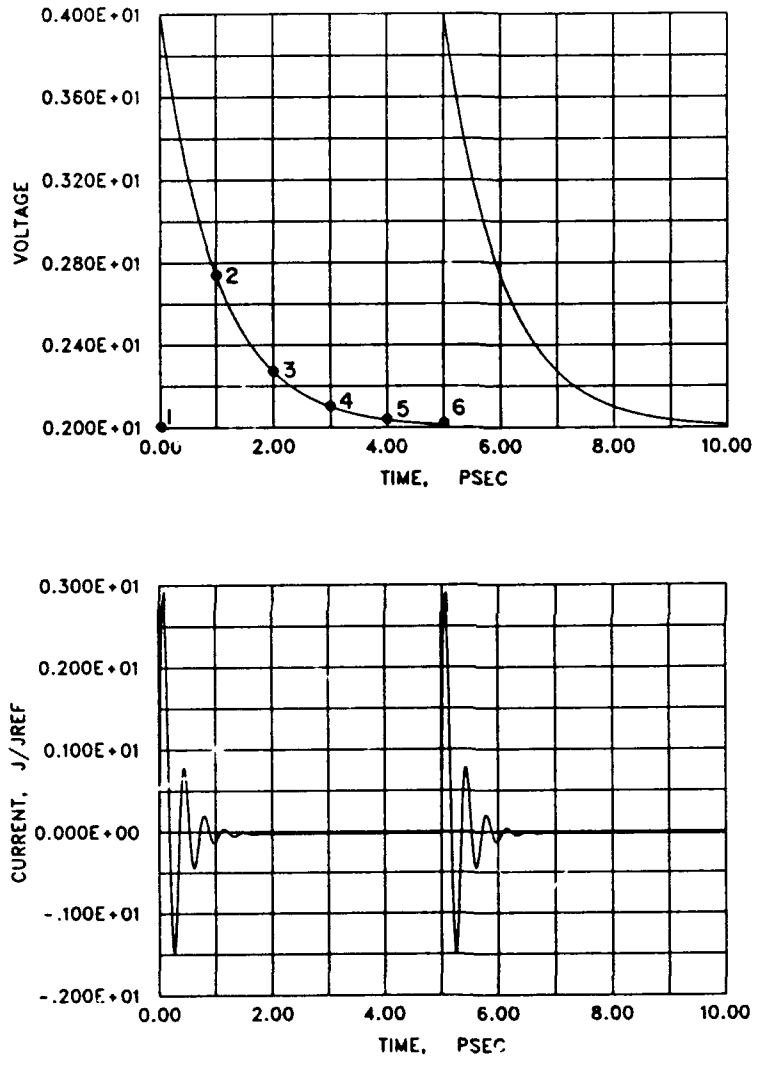

Figure 6.2a Voltage and current profiles for the nominal NIN structure, with a step change in voltage followed by an exponential decay. The dc values of current and voltage for this calculation are $V(DC) = 2.0v$, $J(DC) = 4.22x10^4 A/cm^2$.

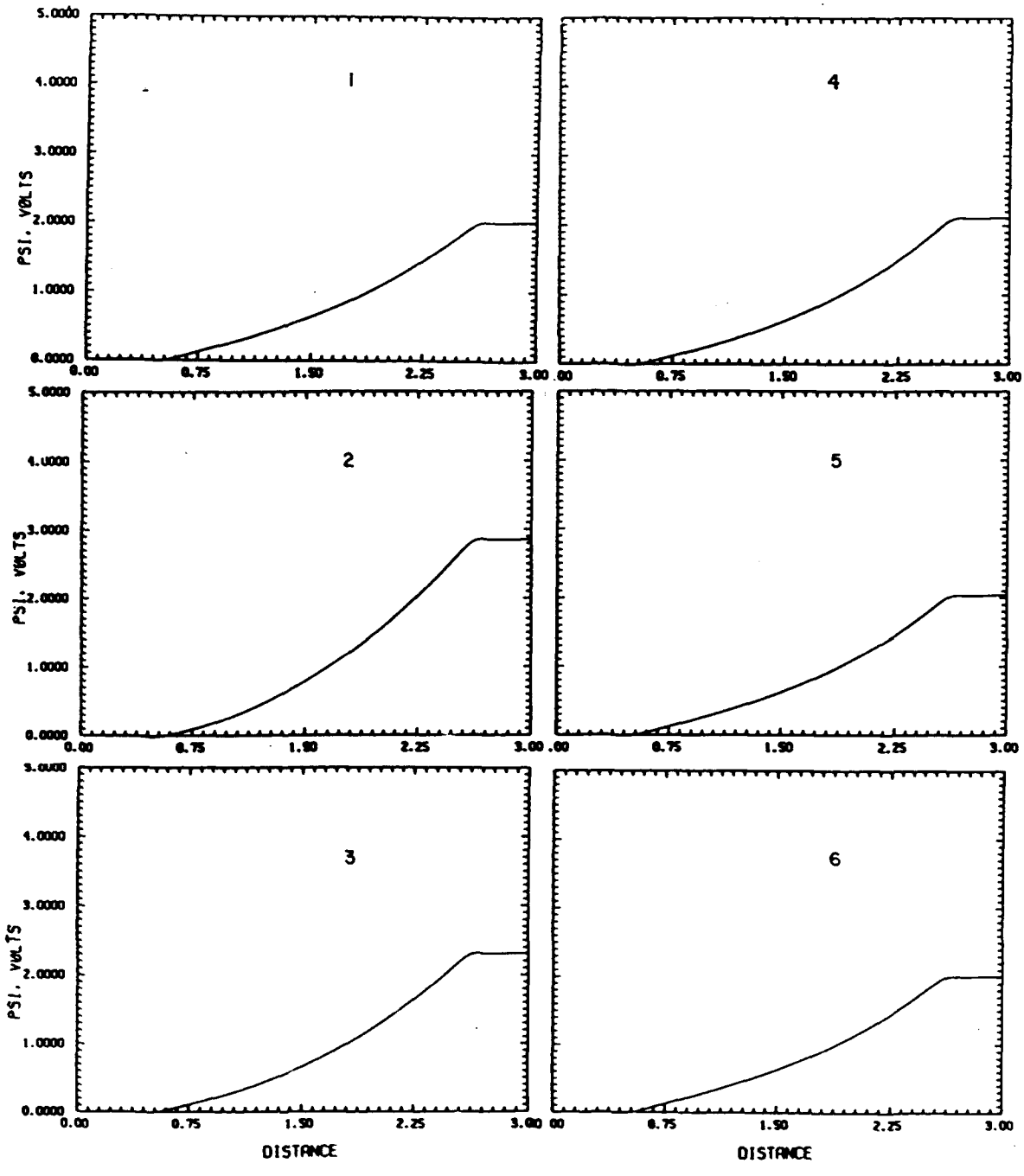

Figure 6.2b Time sequence of potential proiles corresponding to the time dependent calculation of figure 6.2a.

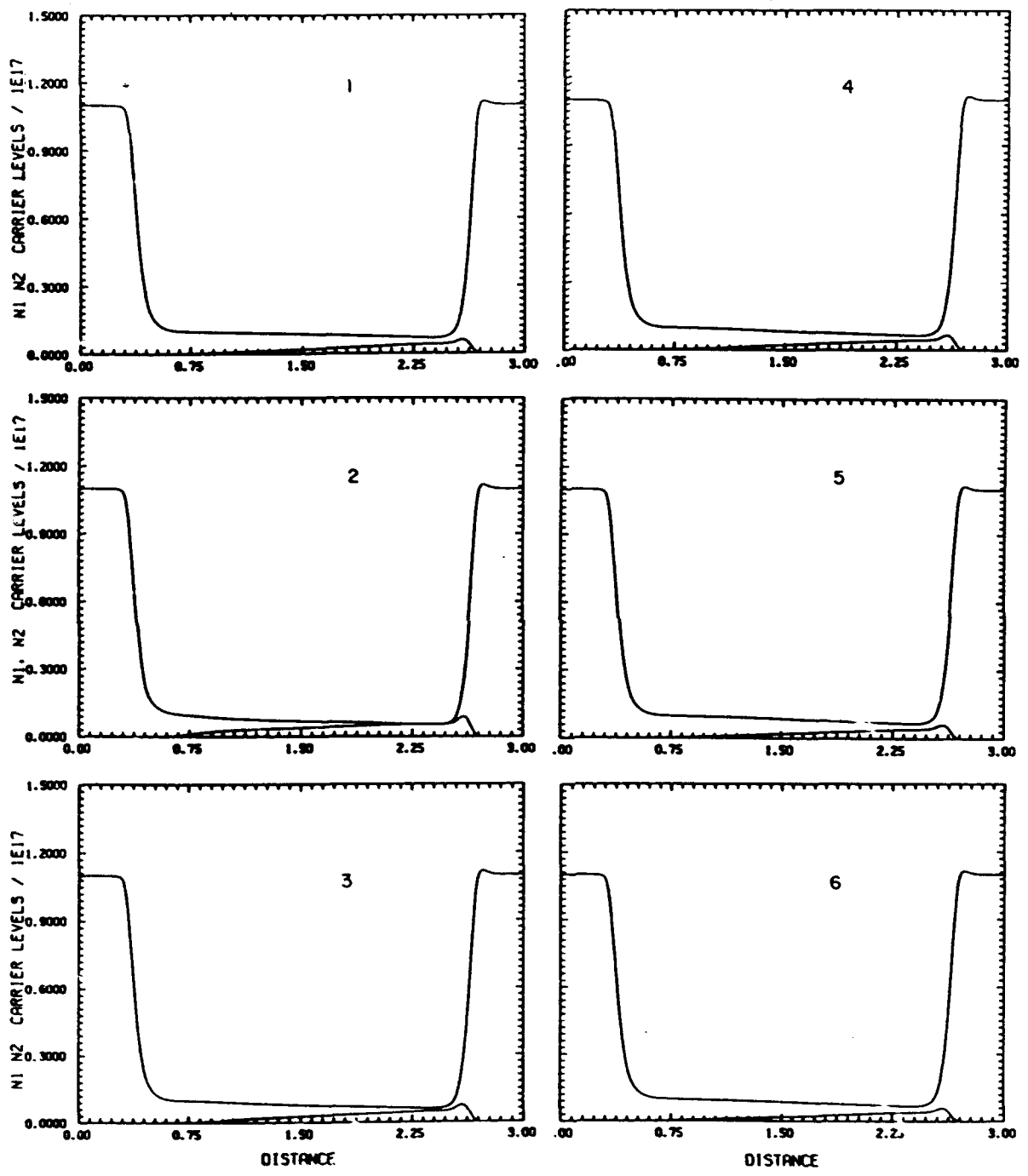

Figure 6.2c Time sequence of density proiles corresponding to the time dependent calculation of figure 6.2a.

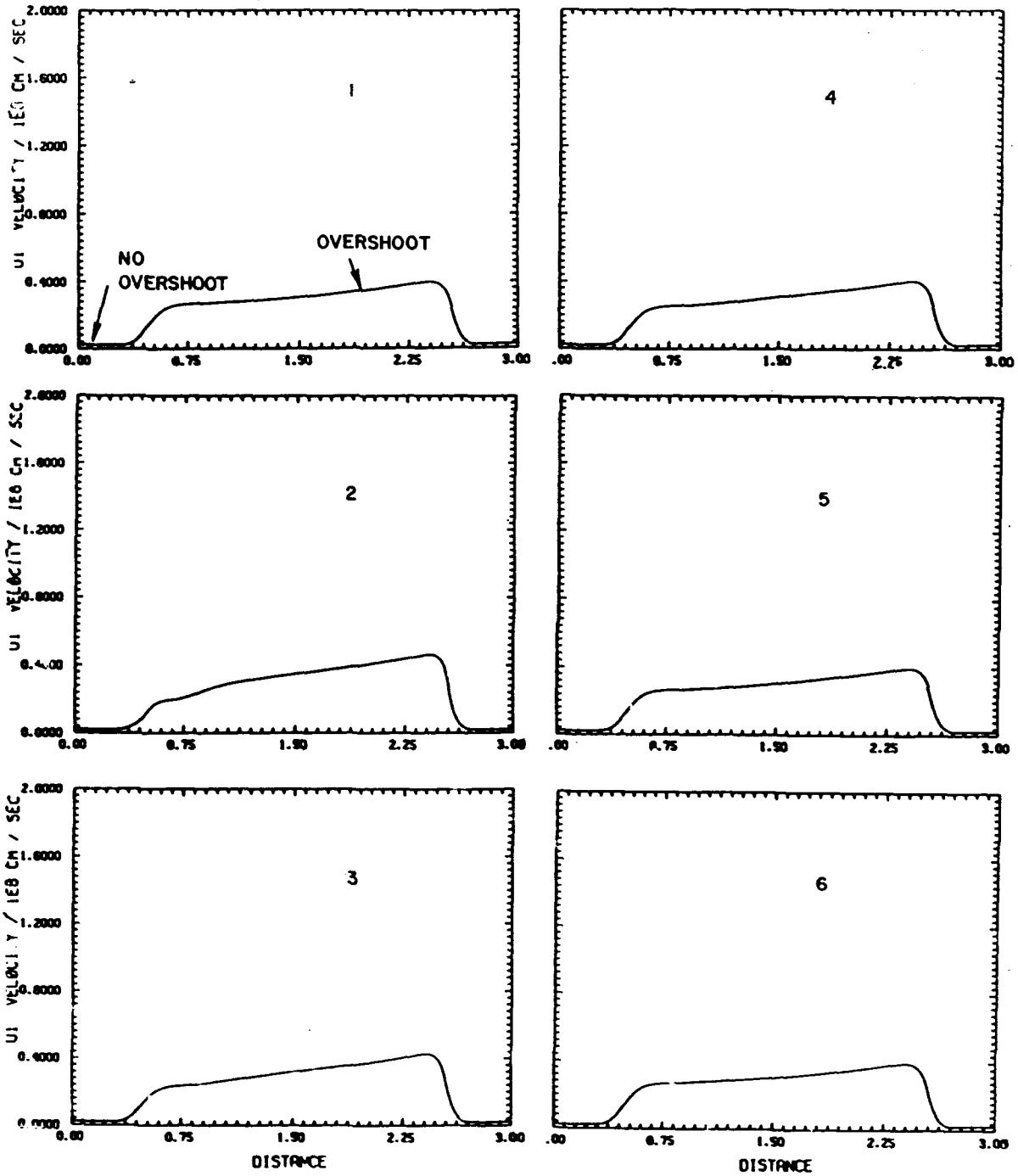

Figure 6.2d Time sequence of gamma valley velocity profiles corresponding to the time dependent calculation of figure 6.2a.

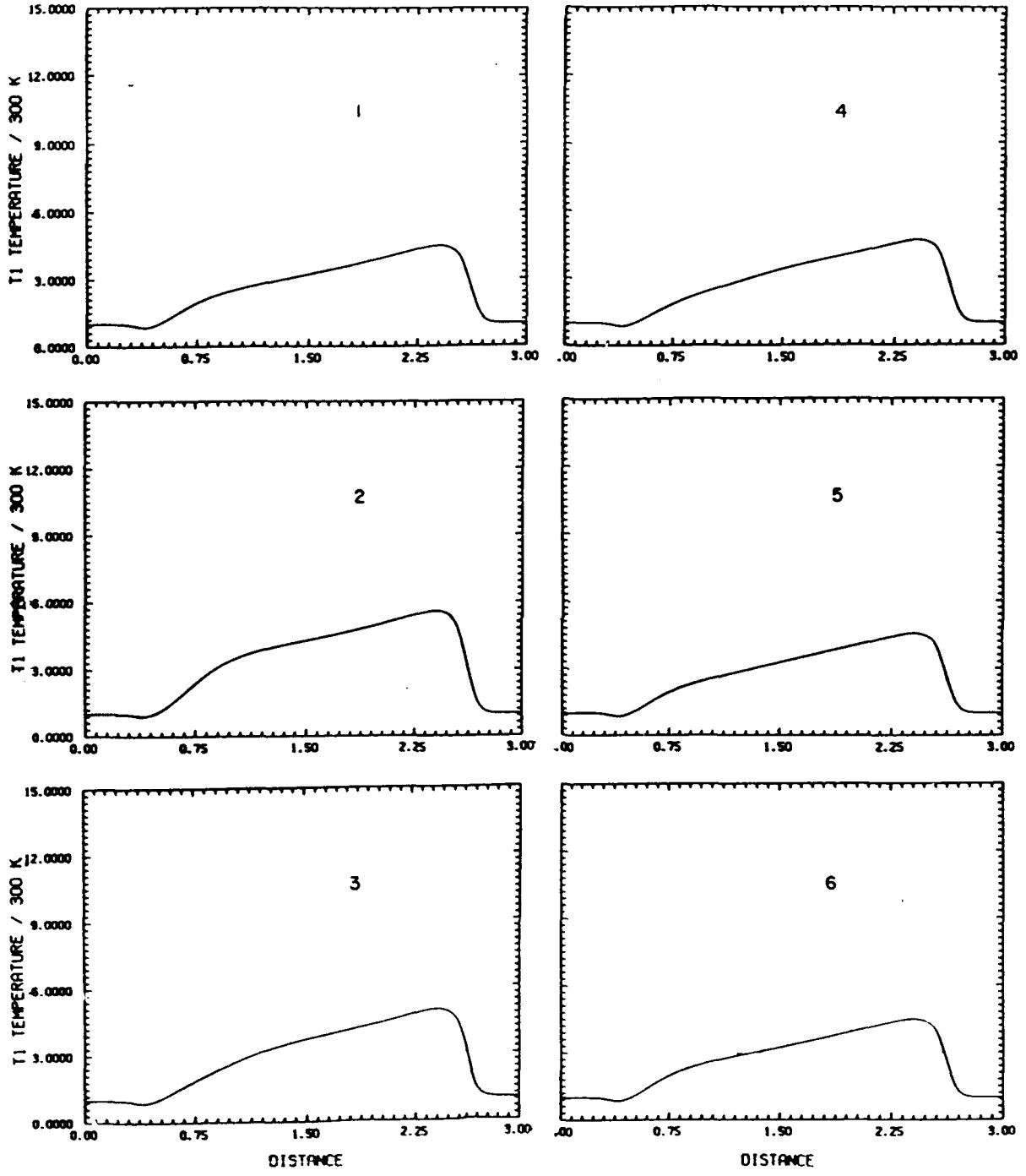

Figure 6.2e Time sequence of gamma valley temperature profiles corresponding to the time dependent calculation of figure 6.2a.

There are several important features to note about the figure 6.3 results when compared to the figure 6.2 results. *First*, the displacement current contributes to the diode current twice during the oscillation, once as the voltage increases and a second time as the voltage decreases. In other words a significant change in the structure of the applied voltage profile introduces the displacement current effects. *Second*, the current level to which the system is relaxing to after the displacement current effects damp out is different *and higher* for the figure 6.3 calculations than for the figure 6.2 calculations (the current is negative, and higher current is more negative current). The implication is that momentum relaxation has occurred, but energy relaxation has not occurred. *Third*, on the first cycle, the steady state current during the first half cycle is greater than the steady state current during the second half, indicating that for this value of bias transfer from lower to upper valleys occurs on a different time scale than transfer from the upper to the lower valleys. During the second part of the cycle this difference is negligible, as indicated by the inset, but as later calculations show this difference is prominent at other voltage levels.

The time sequence of the voltage profiles are shown in figure 6.3b, where we see that the voltage drop across the device spends a longer period of time at the higher values than the corresponding profiles of figure 6.2b. The density profiles in figure 6.3c show more electron transfer during the first part of the cycle than for the corresponding profiles of figure 6.2c. The gamma valley velocity profiles are shown in figure 6.3d. Note that for every frame the velocity is higher than that of the corresponding figure 6.2d profiles. It is this higher velocity that is responsible for the larger value of steady state current. The temperature profiles are displayed in figure 6.3e. We note that everywhere within the structure the electron temperature is higher than for the figure 6.2e calculation. At the downstream N^+ region the electron temperature is highest and is responsible for most of the electron transfer. It is interesting to point out that at the end of each cycle for the figure 6.3 calculation, although the electron temperature is higher than for the figure 6.2 calculations, more of the diode is within the high temperature region in the latter calculations.

The above results indicate that when a signal with a period of the order of the energy relaxation time is imposed upon the structure, the detailed *intra-signal* shape can determine when strong nonequilibrium effects will occur. Differences in the shape of the pulse will manifest themselves in significant differences in the current level which are a direct measure of the differences in the energy and momentum relaxation time. Essentially the calculations of figure 6.3 teaches that if there are time constants associated with the intra-pulse shape and these time constants approach the momentum relaxation time then the current levels will reflect these time constants through increased values. The degree to which these relaxation effects appear will depend when the intervalley exchange is most prominent.

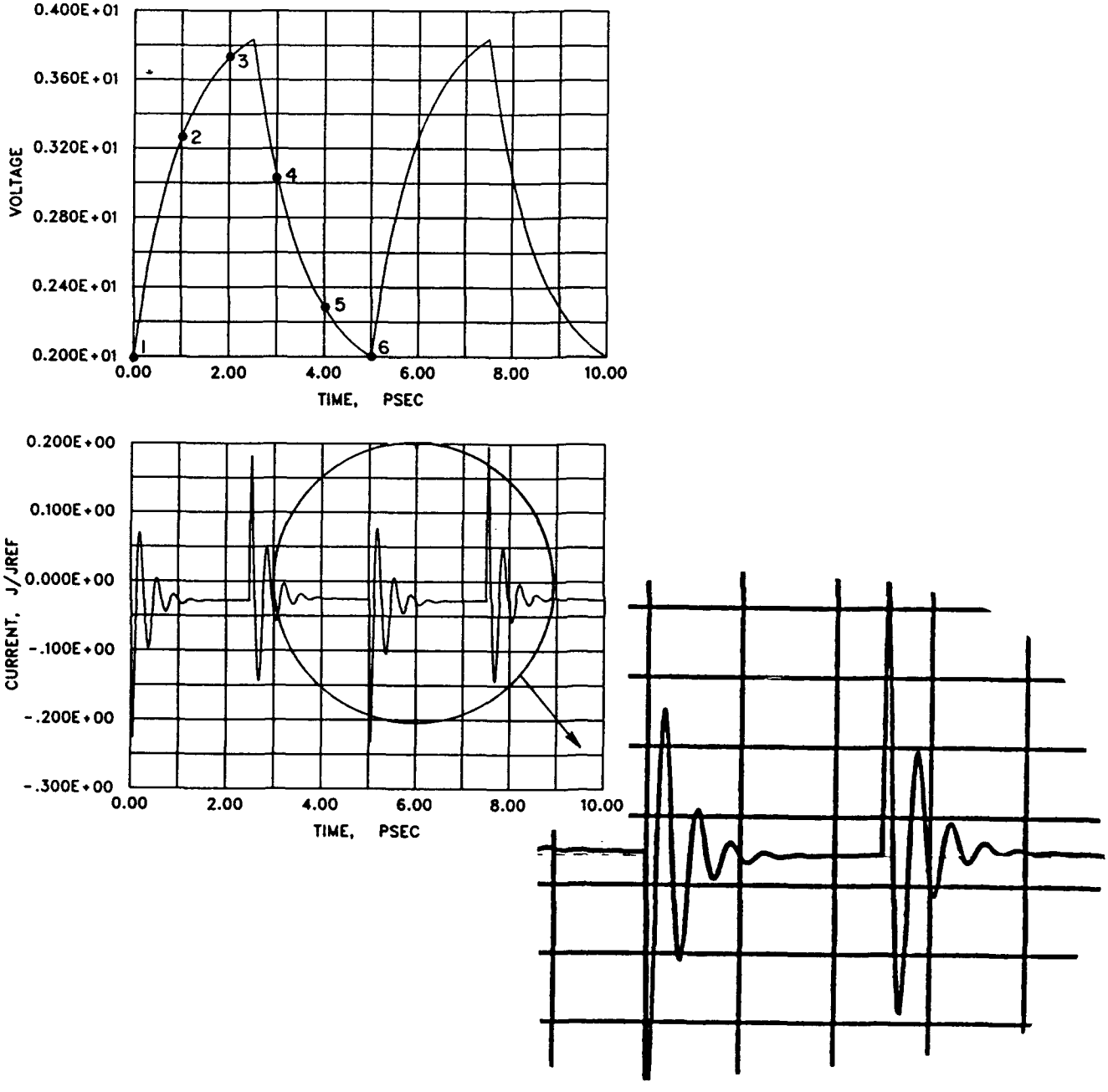

Figure 6.3a Voltage and current profiles for the nominal NIN structure, with an exponential increase and decrease in voltage. The dc values of current and voltage for this calculation are V(DC) = 2.0v, J(DC) = 4.22x10⁴ A/cm².

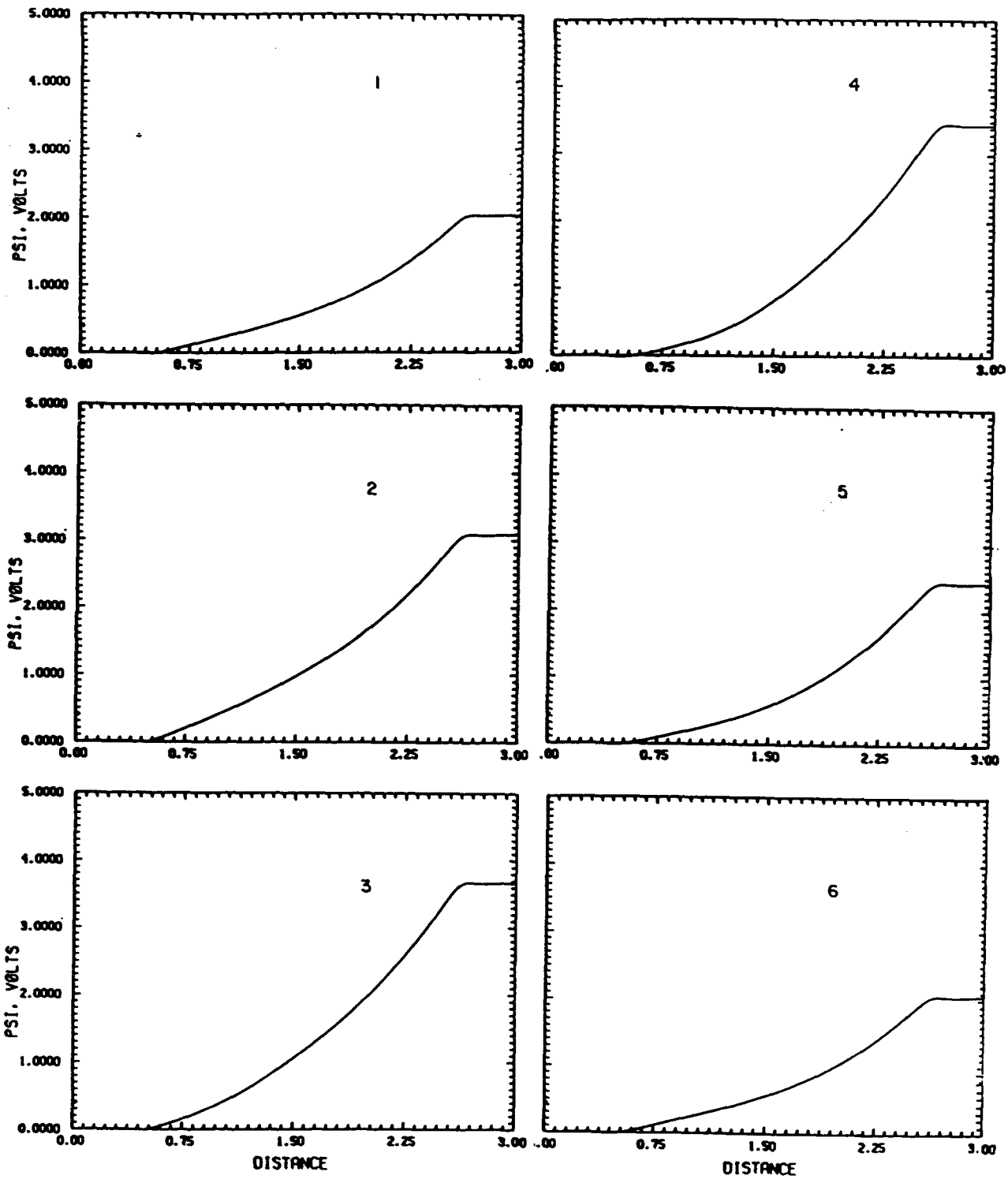

Figure 6.3b Time sequence of potential proiles corresponding to the time dependent calculation of figure 6.3a.

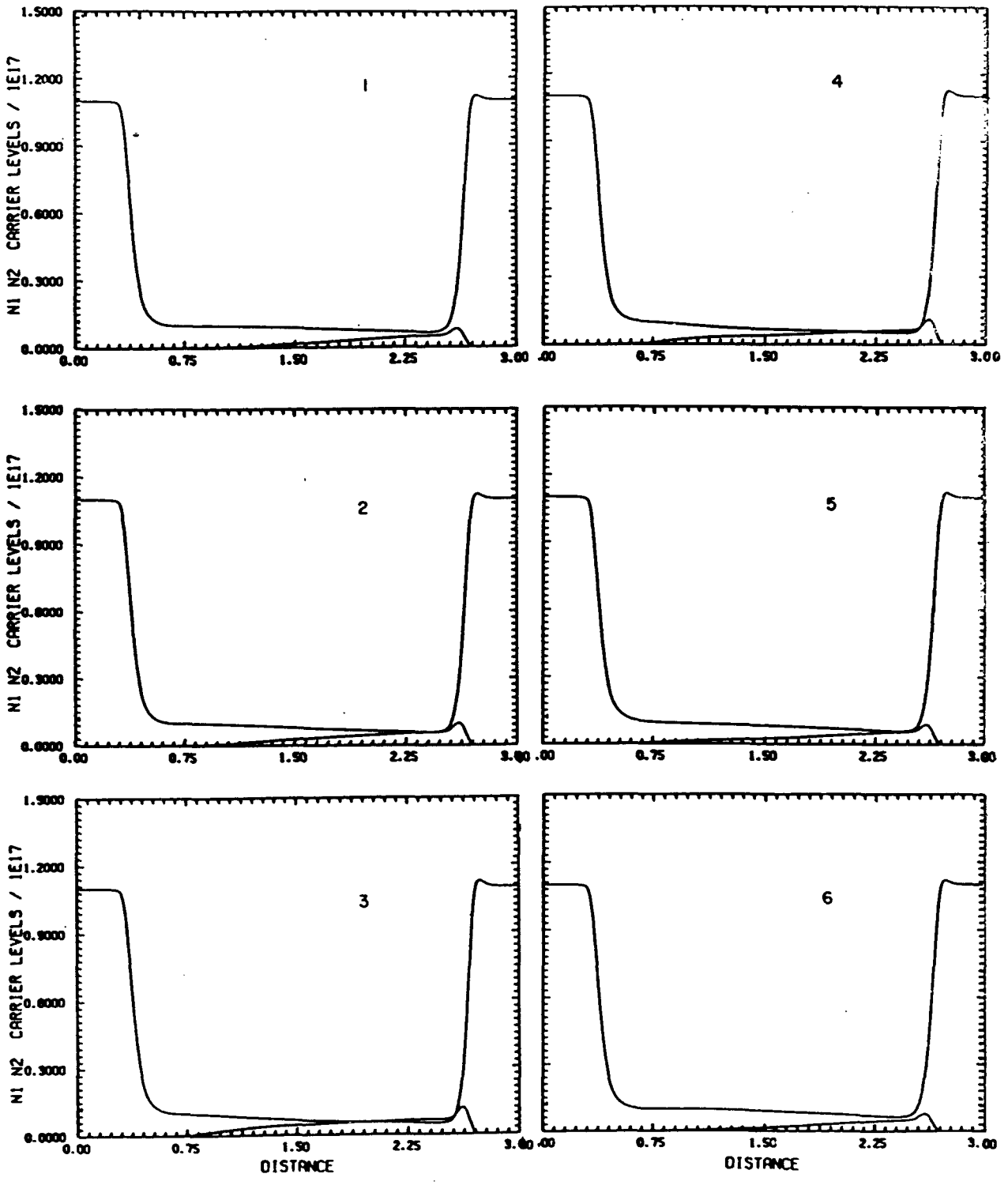

Figure 6.3c Time sequence of density proiles corresponding to the time dependent calculation of figure 6.3a.

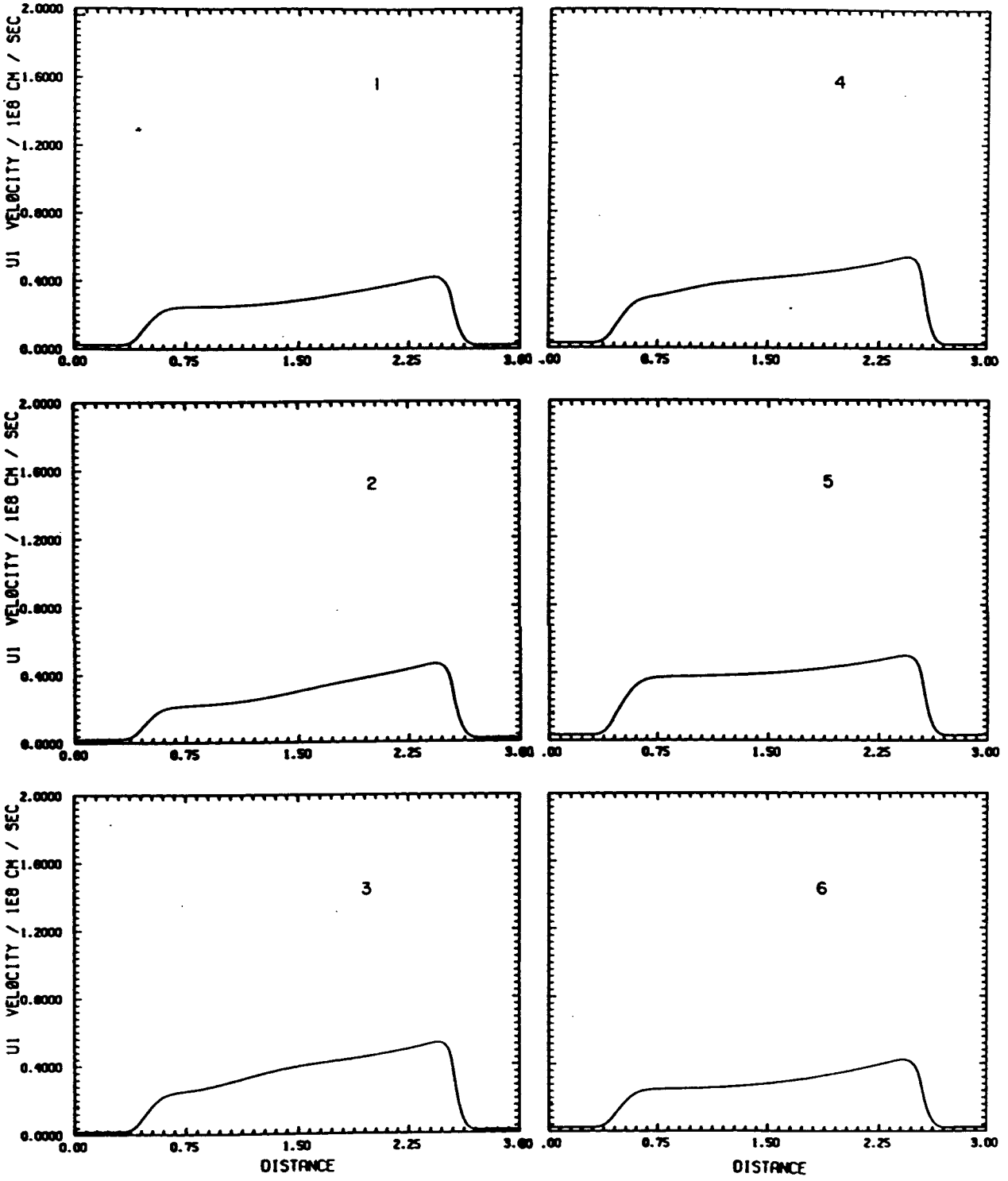

Figure 6.3d Time sequence of gamma valley velocity profiles corresponding to the time dependent calculation of figure 6.3a.

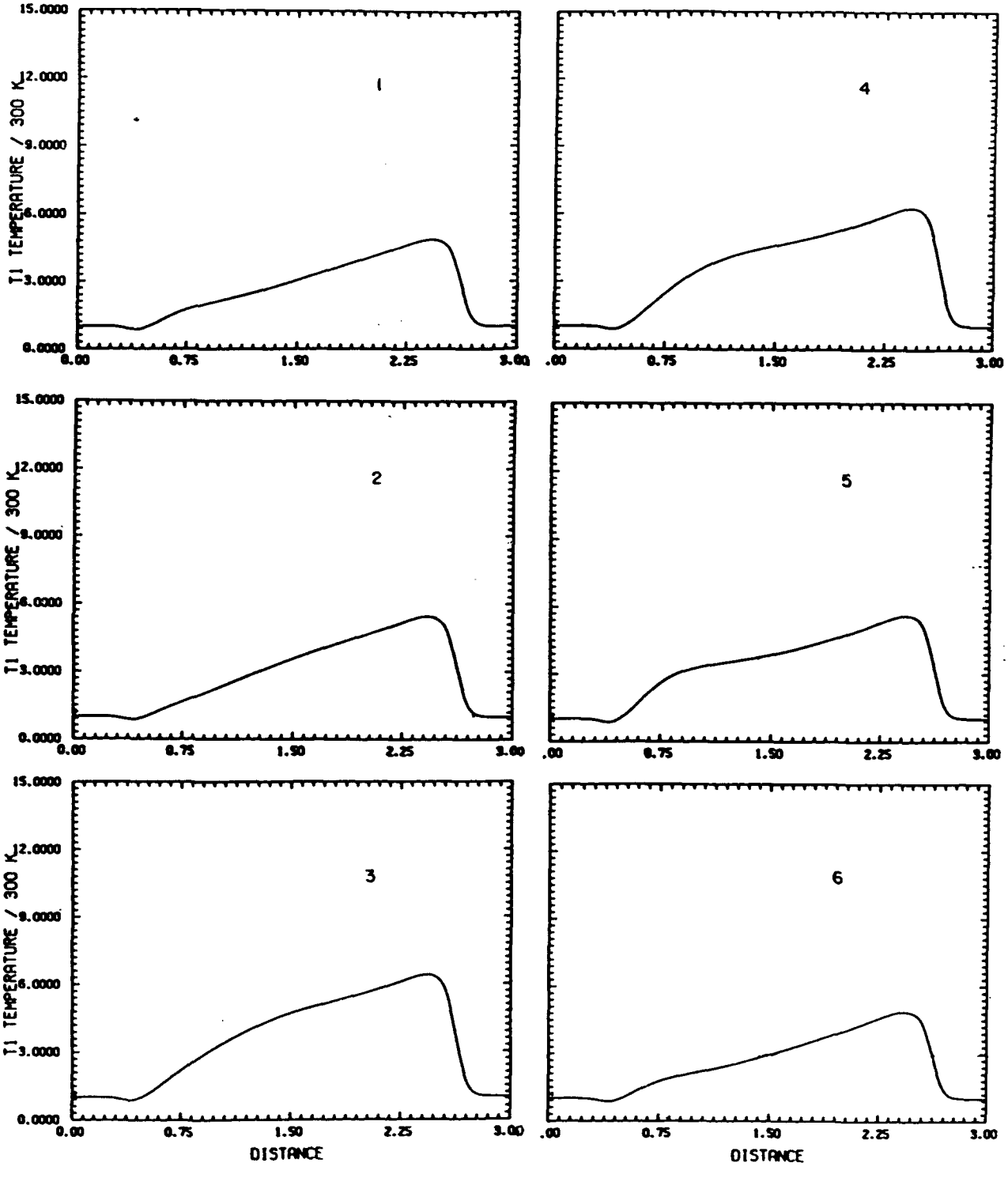

Figure 6.3e Time sequence of gamma valley temperature profiles corresponding to the time dependent calculation of figure 6.3a.

The comparative calculations of figures 6.2 and 6.3 demonstrated that pulses of the order of five picoseconds in duration were not sufficient to elucidate information concerning velocity overshoot, but that intrapulse structure of the order of two picoseconds could emphasize overshoot contributions. An interesting feature of the calculation was that there was a hint that the structure of the current oscillation could provide detailed differences about the rate of intervalley transfer for carriers transferring from the gamma to L valleys and/or from the L to the gamma valleys. Since it is known that the most significant effects of this transfer manifest themselves when transfer is initiated, the calculation of figure 6.3 was repeated but with a *lower* DC bias voltage of one volt.

The calculations are shown in figure 6.4, which should be compared to figure 6.3. In comparing we note several points. There are: (i) two displacement current contributions, (ii) higher steady state values of current, and (iii) the differences between the steady state values on the up and downswings of voltage. But unlike the calculations of figure 6.3, the steady state current differences are more apparent in this calculation. The details of this calculation follow.

Figure 6.4b displays the distribution of voltage across the structure as a function of time. There is still a small retarding field at the upstream N^+ region, and note the strong variation in potential at the downstream boundary. The profiles of electron density, displayed in figure 6.4c show electron transfer near the anode N^+ region, but significantly less than the figure 6.3c calculation. One the basis of these profiles, we note that at the end of three picoseconds there was a gradual transfer of carriers from the gamma to L valley, while in the fourth picosecond there was a rapid return of carriers from the L to the gamma valley. The gamma valley velocity profiles show a more uniform distribution of velocity across the entire undoped region, with values near $4x10^7$ cm/sec, with higher values near the anode occurring later in the cycle when the transfer is greatest to the L valley. Because of the slow electron transfer as the voltage increases, the corresponding high velocities on the upswing; and the rapid transfer of carriers from the L to gamma valleys on the downswing, the steady current on the upswing is considerably larger than the current on the downswing. Note: the electron temperature, figure 6.4e, shows the skewed values near the anode with most of the values hovering around the point where electron transfer should occur. The comparison of figures 6.3 and 6.4 suggest that *if the relaxed current differences during one cycle can be measured we will have an unequivocal measurement of nonequilibrium transients in semiconductors.*

There are several other points that must be addressed, one concerned with the dependence of capacitive or displacement current effects on doping, and the second being the effect of dealing with a voltage source whose period is significantly shorter than the energy relaxation time. Consider first displacement current effects.

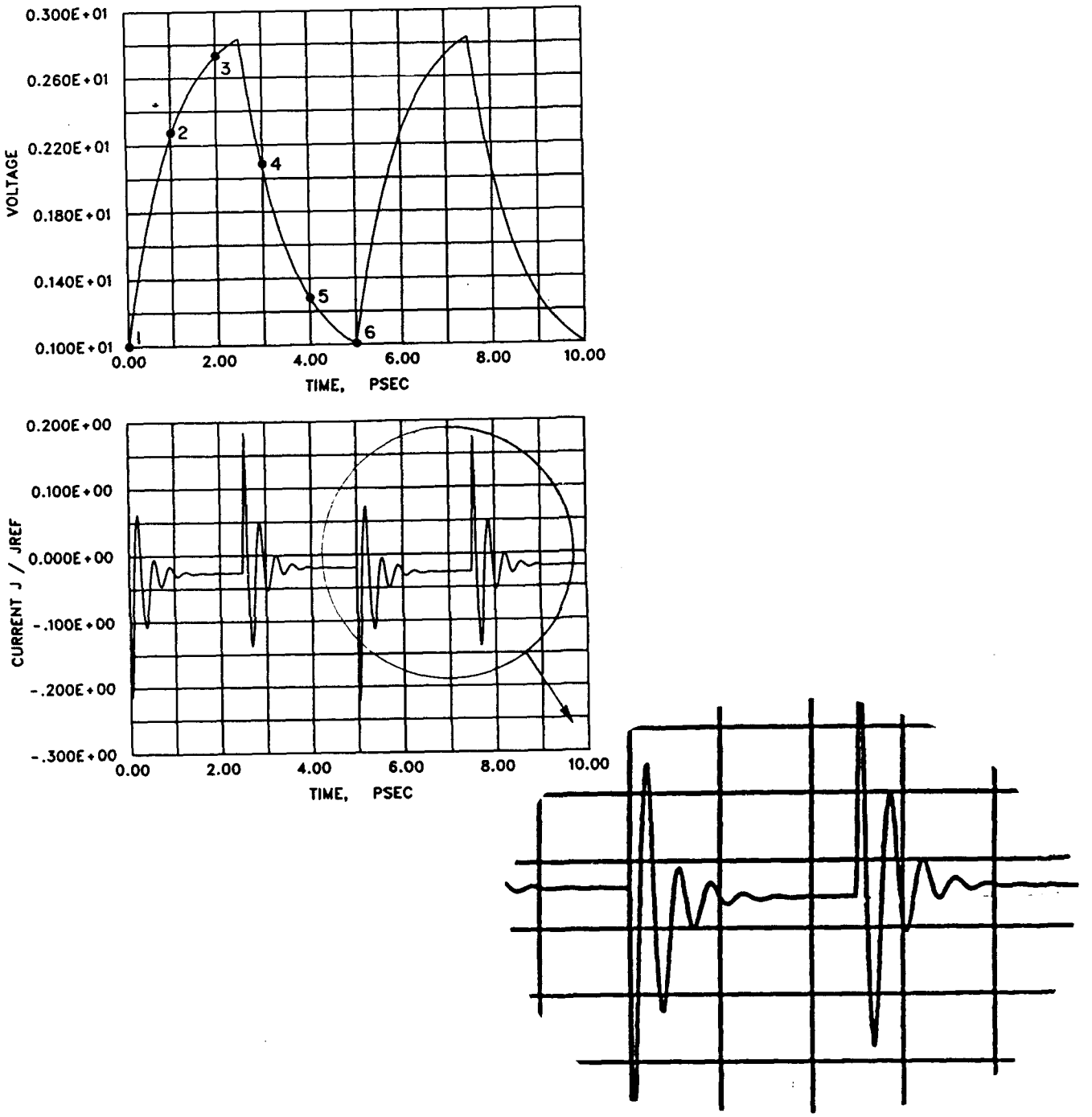

Figure 6.4a Voltage and current profiles for the nominal NIN structure, with an exponential increase and decrease in voltage. The dc values of current and voltage for this calculation are V(DC) = 1.0v, J(DC) = 3.57x10⁴ A/cm².

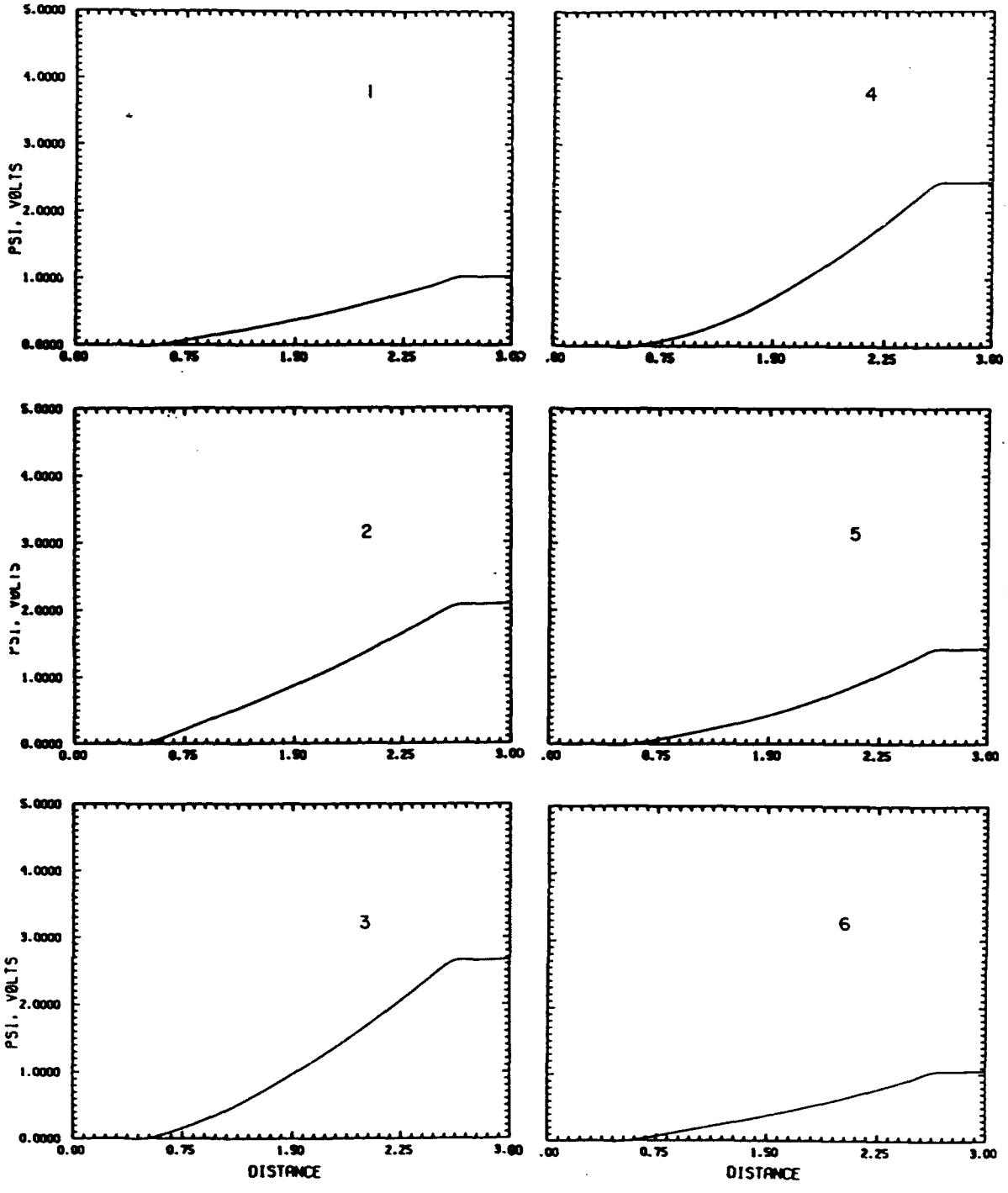

Figure 6.4b Time sequence of potential proiles corresponding to the time dependent calculation of figure 6.4a.

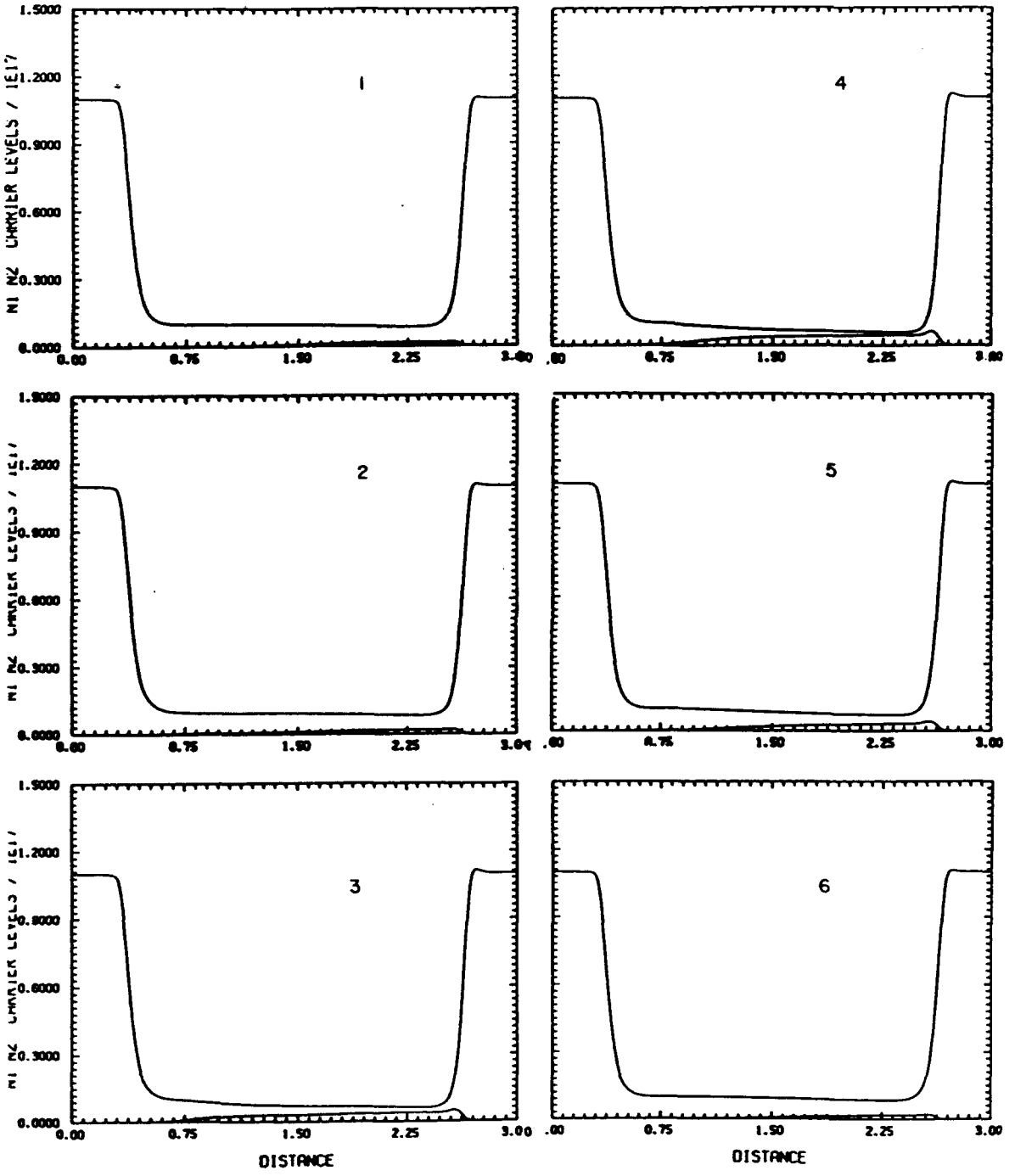

Figure 6.4c Time sequence of density proiles corresponding to the time dependent calcuation of figure 6.4a.

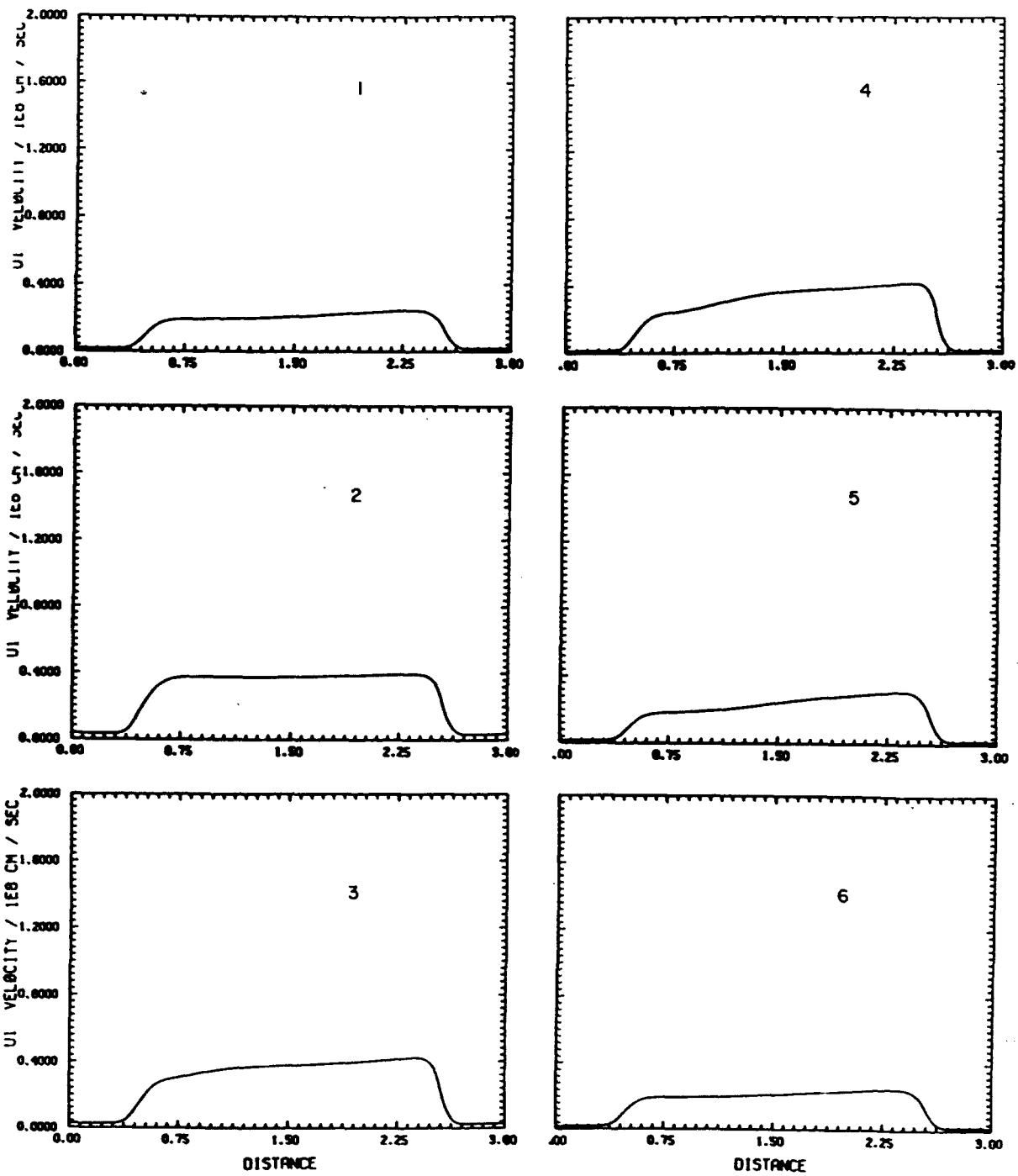

Figure 6.4d Time sequence of gamma valley velocity profiles corresponding to the time dependent calculation of figure 6.4a.

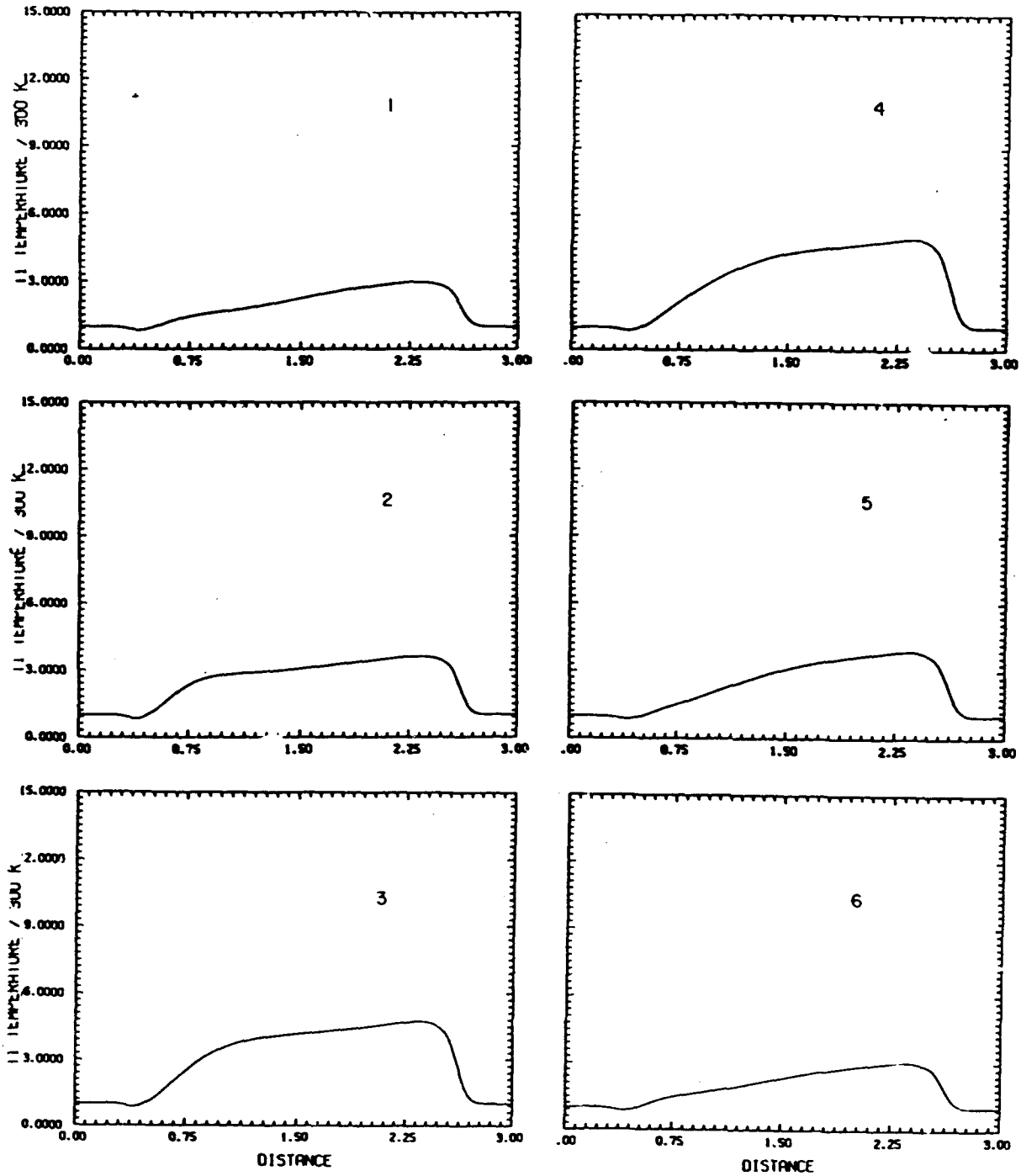

Figure 6.4e Time sequence of gamma valley temperature profiles corresponding to the time dependent calculation of figure 6.4a.

The calculations of figure 6.4 were repeated but with the doping at the N^+ regions increased to $10^{18}/cm^3$. It was anticipated that the displacement current oscillations, which reflect the dielectric relaxation time would end during a shorter time duration. This occurred and is shown in figure 6.5. The charge distributions, potential, velocity and temperature are strikingly similar to the distributions for the lower $10^{17}/cm^3$ calculation and are not repeated.

The situation when the figure 6.3 calculations are repeated but for a period of one picosecond was considered next, with the time dependent results shown in figure 6.5. At the end of 8 picoseconds the structure did not reach steady state equilibrium. Indeed the large current swings are essentially displacement current effects, and while velocity overshoot is occurring at all times during this oscillation, it would be difficult to distinguish this contribution from the displacement current contributions. Indeed it would appear that the measurement of velocity overshoot should concentrate on determining the changes that occur in going from steady state equilibrium to the onset on nonequilibrium.

The broad conclusion that can be drawn from these studies is that nonequilibrium transient effects can be measured; the measurement will not yield overshoot but will provide direct confirmation of the time constants associated with intervalley transfer, which is at the core of nonequilibrium phenomena in III-V materials.

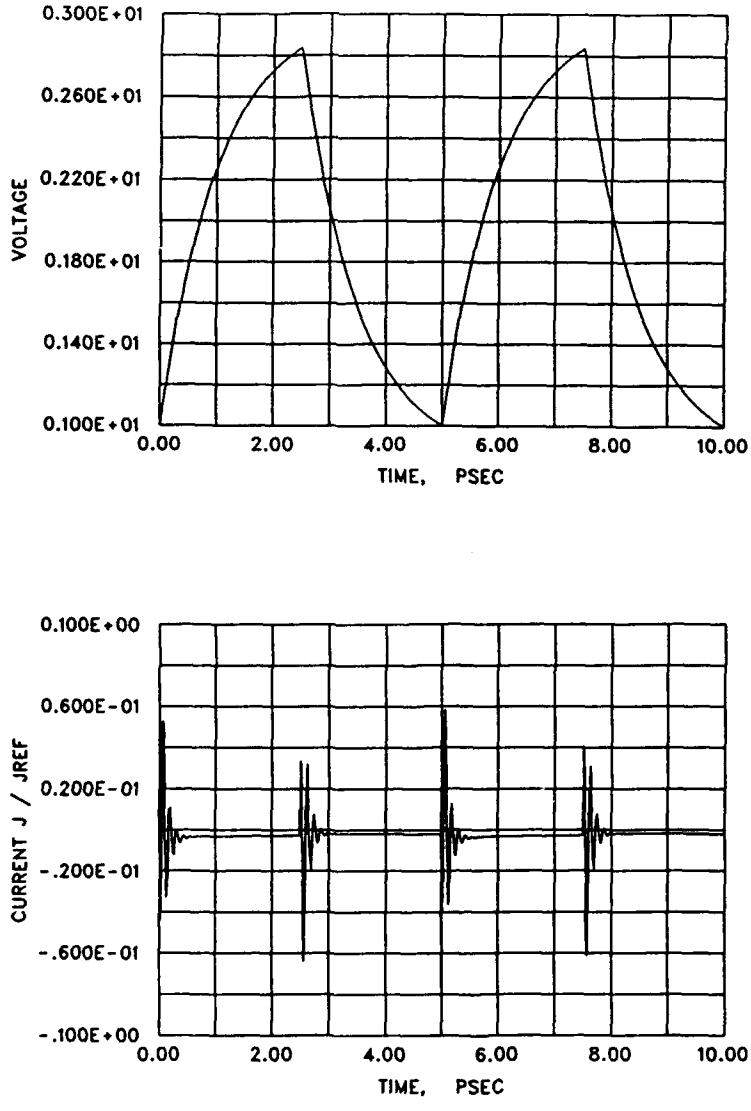

Figure 6.5 Voltage and current profiles for the NIN structure with more heavily doped end regions, with an exponential increase and decrease in voltage. The dc values of current and voltage for this calculation are $V(DC) = 1.0v$, $J(DC) = 3.63x10^4 A/cm^2$.

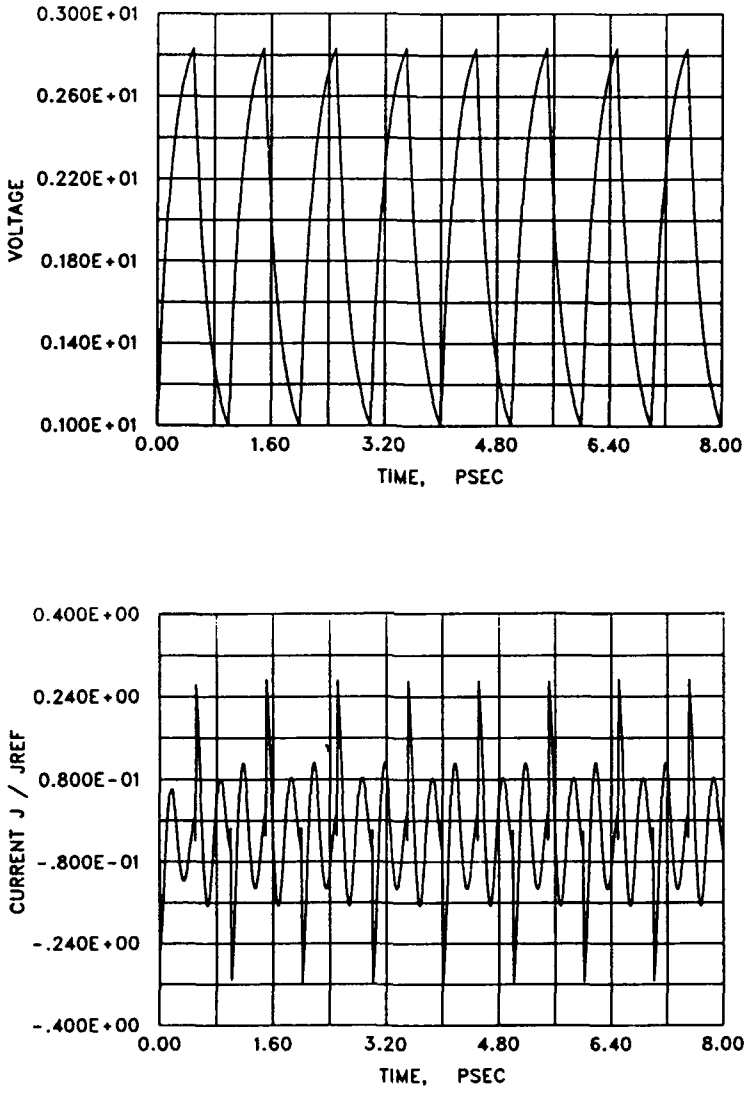

Figure 6.6 Voltage and current profiles for the nominal NIN structure, with an exponential increase and decrease in voltage. The period of this oscllation is one picosecond. The dc values of current and voltage for this calculation are $V(DC) = 1.0v$, $J(DC) = 3.57x10^4 A/cm^2$.

7. Summary

This study focused on the implementation of numerical algorithms for examining the transient behavior of electronic devices and also suggesting experiments to elucidate velocity overshoot.

During the course of the study we also implemented a Monte Carlo algorithm and enhanced the existing moment algorithm to treat transients more accurately, and to include two dimensional scattering events.

The highlights of the study included:

(1) developing new scattering integrals for two dimensional transport;

(2) establishing the presence of terahertz frequency small signal charge density waves forming in the channel of the two dimensional electron gas; and

(3) determining that measurements could be made that would expose the relative time scale differences between energy and momentum relaxation effects--thereby providing evidence for nonequilibrium velocity overshoot.

8. References

Abromowitz, M and I. A. Stegun (1964), *Handbook of Mathematical Functions*, Dover, NY.

Butcher, P. N. (1967), Reports on Prog. Physs. *30*, 97.

Chapman, S. and T. G. Cowling (1964), *The Mathematical Theory of Non-Uniform Gases*, Cambridge Univ. Press, Cambridge.

Grubin, H. L., D. K. Ferry, G. J. Iafrate and J. R. Barker (1982), *VLSI Electronics-Microstructure Science*, Academic Press, NY, *3*, 198.

Grubin, H. L., and J. P. Kreskovsky (1985), *VLSI Electronics-Microstructure Science*, Academic Press, NY, *10*, 237.

Grubin, H. L., and J. P. Kreskovsky (1989), Solid State Electronics *32*, 1071.

Grubin, H. L. (1988) *The Physics of Submicron Semiconductor Devices*, H. L. Grubin, D. K. Ferry and C. Jacaboni, eds, Plenum Press NY, 45.

Grubin, H. L., T. R. Govindan and M. A. Stroscio (1992), to be published.

Jacoboni, C. and L. Reggianni (1983), Rev. Mod. Phys. *55*, 645.

Ketterson, A.A. and Morkoc, H. (1987), IEE Trans. Elec. Dev., ED-33, 1626.

Laval, S, C. Bru, C. Arnodo, and C. Castagne (1980), *Proc 1980 IEDM.*

Ridley, B. (1982) *Quantum Processes in Semiconductors*, Clarendon Press, Oxford.

Ruch, J. G. (1972) IEEE Trans. Elec. Dev. *ED-19*, 652.

Sarma et al (1988), Phys. Rev. *B15, 37*,4560.

Wigner, E. P. (1932), Phys. Rev. *40*, 749.

Yokoyama and K. Hess (1985), Phys. Rev. *B15, 33*,